Hydrogel Microlaser on Chip for Biomedical and Physical Applications

GONG XUERUI

School of Electrical & Electronic Engineering

A thesis submitted to the Nanyang Technological University

in partial fulfillment of the requirement for the degree of

Doctor of Philosophy

2023

Statement of Originality

I hereby certify that the work embodied in this thesis is the result of original research, is free of plagiarized materials, and has not been submitted for a higher degree to any other University or Institution.

01/02/2024

. . . . . .

Date

. . . .

GONG XUERUI

Supervisor Declaration Statement

I have reviewed the content and presentation style of this thesis and declare it is free of plagiarism and of sufficient grammatical clarity to be examined. To the best of my knowledge, the research and writing are those of the candidate except as acknowledged in the Author Attribution Statement. I confirm that the investigations were conducted in accord with the ethics policies and integrity standards of Nanyang Technological University and that the research data are presented honestly and without prejudice.

30/07/2023

. . . . . .

Date

. . . . . .

CHEN YU-CHENG

Authorship Attribution Statement

This thesis contains material from 3 papers published as the first author in the following peer-reviewed journal(s) and 2 papers published and accepted at conferences in which I am listed as an author.

Chapter 3 is published as Gong, Xuerui, Zhen Qiao, Peng Guan, Shilun Feng, Zhiyi Yuan, Changjin Huang, Guo-En Chang, and Yu-Cheng Chen. "Hydrogel Microlasers for Versatile Biomolecular Analysis Based on a Lasing Microarray." Advanced Photonics Research 1, no. 1 (2020): 2000041.

The contributions of the co-authors are as follows:

- Prof. Yu-Cheng Chen provided the initial project direction and experiment.
- I performed all the experiments.
- Prof. Zhen Qiao, Dr. Zhiyi Yuan, Prof. Guo-En Chang and I performed all the numerical simulations.
- I wrote the drafts of the manuscript, and the manuscript was revised by Prof. Yu-Cheng Chen.
- Prof. Yu-Cheng Chen supervised the work and evaluated the performance.
- Mr. Guan Peng modified the inkjet printer in this work.
- Prof. Changjin Huang provided guidance for hydrogel polymerization.

Chapter 4 is published as Gong, Xuerui, Shilun Feng, Zhen Qiao, and Yu-Cheng Chen. "Imaging-based optofluidic biolaser array encapsulated with dynamic living organisms." Analytical Chemistry 93, no. 14 (2021): 5823-5830.

The contributions of the co-authors are as follows:

- Prof. Yu-Cheng Chen initiated the project and experiment.
- I performed all the experiment and prepared the manuscript.
- I and Prof. Zhen Qiao performed the numerical simulation.
- I wrote the drafts of the manuscript.

- Prof. Shilun Feng and I prepared the E. coli culturing.

Chapter 5 is published as Gong, Xuerui, Zhen Qiao, Yikai Liao, Song Zhu, Lei Shi, Munho Kim, and Yu‐Cheng Chen. "Enzyme‐Programmable Microgel Lasers for Information Encoding and Anti‐Counterfeiting." *Advanced Materials* 34, no. 10 (2022): 2107809.

The contributions of the co-authors are as follows:

- Prof. Yu-Cheng Chen initiated the project and experiment.
- I performed all the experiments.
- Dr. Zhen Qiao and I performed the numerical simulation.
- I wrote the drafts of the manuscript.
- Prof. Lei Shi and Dr. Song Zhu provided the microbottle for Q-factor calibration.
- Prof. Yu-Cheng Chen revised the paper.
- Prof. Yu-Cheng Chen supervised the work and evaluated the performance.
- Dr. Yikai Liao, Prof. Munho Kim and I performed the SEM test.

01/02/2024

. . . . . .

Date

. . . . . .

GONG XUERUI

Acknowledgment

I am profoundly grateful for the help and encouragement I've received from numerous individuals throughout my doctoral journey. Their invaluable support has instilled in me the resilience to tackle each challenge that I have encountered along the way.

First and foremost, I wish to extend my profound gratitude to my supervisor, Professor Yu-Cheng Chen. When I embarked on my Ph.D. journey in 2019, I was a fresh undergraduate, largely unaware of the academic landscape and the challenges it presented. Not only is Prof. Yucheng-Chen a genius in research, consistently nurturing innovative ideas to widen our horizons, but he also respects his students immensely. Beyond being just a supervisor, he has been akin to an older brother, supporting me in both my research and personal life. Regardless of the mistakes I've made or the problems I've faced, Prof. Yucheng-Chen has consistently been there to lend a helping hand. I consider myself incredibly fortunate to have met Prof. Yucheng-Chen; without him, I wouldn't be the knowledgeable and skilled researcher I am today.

I also wish to express my heartfelt appreciation to my colleagues, Dr. Qiao Zhen, Dr. Gong Chaoyang, Mr. Zhou Yunke, Mr. Yuan Zhiyi, Ms. Chenlu Wang, Dr. Zhang Yifan, Dr. Daniel N. Roxby, Mr. Randall Ang, Mr. Hamin Rivy, Mr. Guan Peng, Ms. Wang Ziyihui, Mr. Nie Ningyuan, Mr. Fang Guocheng, Mr. Zhou Tian, and Mr. Fu Bowen. Their invaluable advice and constructive suggestions have enabled me to surmount obstacles, devise solutions, and kindle fresh ideas. They have broadened my life experiences and gifted me with cherished memories. I extend my thanks for their unwavering support, and I acknowledge that each one of them possesses qualities and attributes that are truly worth emulating.

I would also like to express my gratitude to Ms. Jiasheng Yin, who provided unwavering support for my decision to pursue a Ph. D during my undergraduate

studies. Her presence greatly enriched the initial two years of my doctoral journey, creating memories I will always cherish.

My heartfelt appreciation and deep love go to Dr. Xuwen Cheng, who stood by my side through challenging times and remained until my recovery. I consider myself incredibly fortunate to have known her since I was 17 and to have maintained our connection until now. Her unwavering support and kindness have not only given me hope in the dark but also instilled in me the courage to face any obstacles that lie ahead.

Lastly, I want to express my profound gratitude to my family. Their pride in my accomplishments has been a constant source of encouragement, and their unconditional support has never wavered. I am grateful for the freedom and courage they've instilled in me throughout this journey. Their faith in my abilities has been the cornerstone of my success, and I cannot express my appreciation for their love and understanding enough.

Content

Abstract

Biological microlasers have positioned themselves as a potent tool for the detection and identification of biomolecules in the last decade. The key advantages of laser-based detection over fluorescence-based methods include signal amplification, tighter linewidth, and superior signal-to-noise ratio, culminating in a remarkable increase in detection sensitivity. Moreover, due to the nonlinearity of the signal at the lasing threshold, laser emission can offer improved axial spatial resolution. The vast diversity in laser parameters such as threshold, intensity, and transverse mode makes lasers suitable candidates for anti-counterfeiting techniques. Despite of recent progress in achieving lasing for molecular biosensing and anti-counterfeiting labeling, the challenges in raw material fabrication and physical property limitations often lead to micro-lasers that lack versatility and functionality in real world applications. Therefore, this dissertation explores the potential of using reconfigurable materials hydrogels to develop a platform that is versatile and well-suited for both chemical sensing and physical anti-counterfeiting.

For better understanding of this dissertation, we begin with a brief review with the introduction of biological lasers and characteristics of hydrogels, then we introduce the background of applications in biochemistry and security techniques (Chapter 1 and Chapter 2). In Chapter 3 and 4, we successfully developed a Whispering Gallery Mode (WGM) hydrogel biological microlaser, capable of detecting variations in molecular distances and differentiating molecular sizes based on lasing threshold. The study also demonstrates the microlaser's ability to encapsulate and analyze living organisms with superior sensitivity compared to traditional fluorescence analysis. Moving to physical applications in Chapter 5 and Chapter 6, we harnessed the inherent properties of hydrogels to create tunable microlasers for anti-counterfeiting purposes. Through enzyme-based reactions, the hydrogel's internal structure

and its corresponding lasing emission were manipulated, enabling a novel approach for information encoding and encryption. Furthermore, the fusion of Förster Resonance Energy Transfer (FRET) lasers and hydrogel's structural randomness yielded a high-capacity optical encoding method, adding an advanced layer of security against counterfeiting. These key findings of this research underscores the immense potential and versatility of hydrogel microlasers, bridging the fields of biophotonics and information security and opening new avenues for future applications and investigations.

List of Figures

List of Abbreviation

Fabry-Perot (FP)

Whispering gallery mode (WGM)

Distributed Bragg reflector (DBR)

Free spectral range (FSR)

Transverse magnetic (TM)

Transverse electric (TE)

Laser emission microscope (LEM)

Green fluorescent protein (GFP)

Förster resonance energy transfer (FRET)

Rhodamine B (RhB)

Fluorescein isothiocyanate (FITC)

N-Hydroxysuccinimide (NHS)

N-(3-dimethylaminopropyl)-N-ethylcarbodiimide hydrochloride (EDC)

Rhodamine 6G (R6G)

L-Glutathione oxidized (GSH)

FITC N-hydroxysuccinimide ester (FITC-NHS)

Rhodamine N-hydroxysuccinimide ester (RhB-NHS)

Escherichia coli *(E. coli*)

SYTO BC green fluorescent nucleic acid stain (Syto-BC)

Luria-Bertani broth (LB broth)

Phosphate Buffered Saline (PBS)

Refractive index (RI)

Acrylamide (AAm)

Polyacrylamide (PAAm)

Alginate methacrylate (M-AAm)

Fluorescein-o-methyacrylate (F-MA)

Bis-acrylamide (Bis-AA)

Gel permeation chromatography (GPC)

Quality factor (Q-factor)

Ince-Gaussian (IG)

Laguerre-*Gaussian (*LG)

Acryloxyethyl thiocarbamoyl rhodamine B (Rhodamine-M)

Green fluorescent protein (GFP)

Cadmium sulfide (CdS)

Chapter 1: Introduction

1.1 Motivation and Objective

The recent advent of biological microlasers has gathered substantial scholarly attention, catalyzing significant advancements within the field. Biological microlasers offer an extensive array of parameters, encompassing lasing spectrum, spatial pattern, laser mode profile, lifetime, thresholds, and gain distribution, among others. Leveraging the unique properties of stimulated emission, biological microlasers demonstrate significant potential for applications in biosensing and bioanalysis. Although these devices can enhance signal intensity exponentially, the dearth of versatile platforms on which to base biological microlasers hampers the expansion of their utilization in multidimensional sensing within biomedical research.

Simultaneously, information anti-counterfeiting technology has emerged as a burgeoning field of study, demonstrating paramount importance in safeguarding high-value commodities such as luxury goods and pharmaceuticals. The inherent characteristics of biological microlaser-generated signals—primarily their extreme sensitivity to external stimuli and material structure—endow them with potential for generating large volumes of data. This makes biological microlasers highly suitable for pioneering novel anti-counterfeiting techniques. However, the current body of research is markedly limited, predominantly focusing on traditional inorganic materials with scant attention given to the employment of biological microlasers and biomaterials in developing efficient and reliable anti-counterfeiting methods.

In summation, the primary aim of this dissertation is to investigate a novel, versatile platform grounded on the generation of biological microlasers from micro-hydrogels. The ultimate objective is to facilitate the application of these biological microlasers in two critical realms: the chemical side, specifically biosensing, and the physical side, namely, anti-counterfeiting technology.

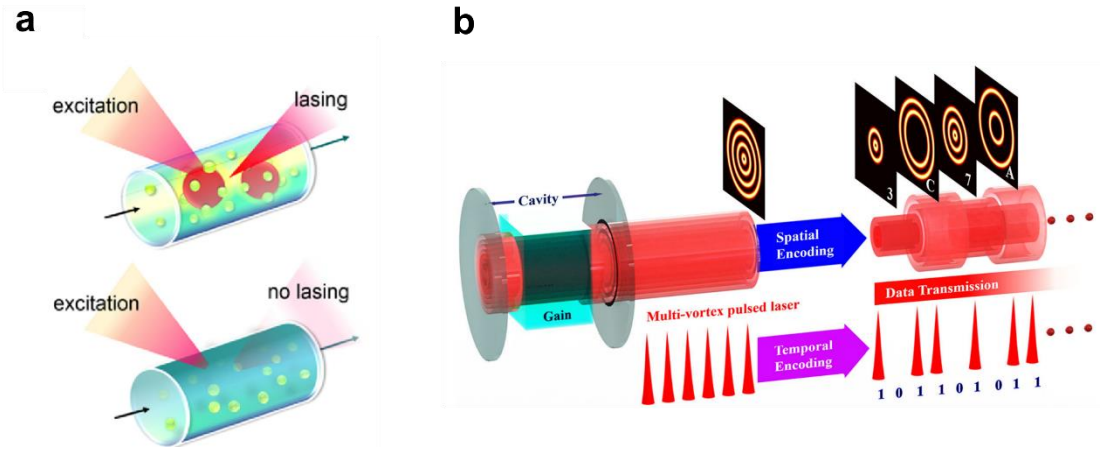

Figure 1.1 Schematics diagram of biosensing and laser-based information security technology. **(a)** Biological microlaser generating from proteins in blood[1]. **(b)** Encoding process based on laser modes[2].

The main objective of this thesis includes:

1. To propose a new hydrogel array fabricated by a commercial inkjet printer and investigate its lasing performance. Using such a hydrogel biological microlaser array to visualize the molecular distance between Förster resonance energy transfer (FRET) pairs and differentiate the molecular size based on lasing threshold.
2. To develop a biological microlaser array that can be integrated with living organism. Investigate the limit of detection of this method and use it to monitor the effect of drugs on living organism based on laser images.
3. To explore the possibility of achieving tunable and controllable lasing signal from hydrogel. Additionally, the connection between laser performance and enzyme reaction occurred on hydrogel chain will also be explored. Once tunability and controlled lasing are achieved, biological microlaser could be employed for both encoding and encryption method.
4. To develop a laser anti-counterfeiting method based on the intrinsic of hydrogel network randomness introduced by free radical polymerization. This would provide enhanced security by generating huge a volume of data due to the intrinsic link between the hydrogel network's inner structure and the emitted laser beam.

1.2 Main Contributions of the Thesis

The major contributions of this thesis include:

- The development of hydrogel microlasers by exploiting the versatility and controllability of hydrogels, where WGM lasing was achieved by printing hydrogel droplets on a mirror. Lasing behaviors and fundamental characteristics of hydrogel lasers were explored under various water-monomer ratios and crosslinking degrees. Hydrogel lasing microarray was developed, providing a novel approach to study molecular interactions within the 3D hydrogel network structure. To demonstrate the potential application and functionality, FRET peptide lasing was exploited for molecular analysis. Single-mode FRET laser emission was achieved by tuning the Forster distance in hydrogel droplets. For this purpose, Different types of biomolecules were encapsulated to achieve biolasing. These findings not only highlight the ability of hydrogel biological microlasers for high-throughput biomolecular analysis but also provide deep insights into the relationship between biostructure and laser physics.
- A novel biological microlaser array encapsulated inside living *E. coli* bacteria to reflect the dynamic changes of living organisms. The concept of image-based lasing analysis was proposed by quantifying the integrated pixel intensity of lasing image from whispering-gallery modes. Dynamic interactions between *E. coli* and antibiotic drugs were compared under fluorescence and laser emission images. The amplification that occurred during laser generation enabled the quantification of tiny biological changes in the gain medium. Laser imaging presented a significant increase of integrated pixel intensity by two orders of magnitude. Our findings clearly demonstrate that image-based lasing analysis is more sensitive to dynamic changes than fluorescence analysis, paving the way for high-throughput on-chip laser analysis of living organisms.
- Development of a biological programmable laser, in which lasing could be manipulated by biomolecular activities at nanoscale. Tunable lasing wavelengths were achieved by exploiting swelling of enzyme-responsive hydrogel droplets in a

Fabry–Pérot microcavity. Both experimental and theoretical data demonstrate that inner 3D network structures and external curvature of hydrogel droplets lead to different lasing thresholds and resonance wavelengths. Inkjet-printed multiwavelength laser encoding and anticounterfeiting were showcased at different scalabilities and in different environments. Hyperspectral laser images were utilized as an advanced feature for higher level of security. The biological encoded laser will provide a new insight into the development of bio-synthetic and bio-programmable laser devices, offering new opportunities for secure communication and smart sensing.

- A novel strategy for anti-counterfeiting, harmonizing the intricate structures of hydrogel networks with the molecular distance sensitivity of FRET lasers. The inherent randomness produced by free radical polymerization in hydrogel structures was exploited to generate intricate and secure anti-counterfeiting codes. The convergence of hydrogel structural complexity and FRET laser sensitivity gave rise to a methodology with significant data capacity. An experimental proof-of-concept test validated the potential of this approach, suggesting new avenues in the field of information security. This research underscores the power of integrating material science and information security, contributing to the development of robust and efficient techniques for data encoding and decoding.

1.3 Organization of the Thesis

The thesis consists of 7 Chapters:

Chapter 1 begins with the motivation and objectives of the thesis. Then, the thesis main contribution is proposed, and the organizational structure of the paper is defined in the final section.

Chapter 2 briefly introduces the background of biological microlaser used for sensing, hydrogel-based applications and anti-counterfeiting technologies. A theoretical background of laser is also included.

Chapter 3 investigates the possibility of achieving laser using hydrogel. A novel platform of hydrogel biological microlaser array is proposed. It's practical application including molecular distance detection and molecular size differentiation, were achieved to demonstrate the versatility of this method.

Chapter 4 demonstrated the realization of the biological microlaser array proposed in Chapter 3. Living microorganism was encapsulated in the micro semi-sphere and served as gain material for laser generation. Detection limitations and dynamic changes of the living microorganism were both investigated.

Chapter 5 reported an innovative microgel laser which can be tuned in response to an enzyme reaction occurred on hydrogel chain. Lasing performance in corresponding to different degree of enzyme reaction was investigated and a fully controllable lasing signal was obtained. Both encoding and encryption were realized based on such a microgel laser.

Chapter 6 demonstrates the potential of leveraging the inherent randomness of the hydrogel three-dimensional network resulted after free radical polymerization and using it for anti-counterfeiting purposes. The chapter successfully demonstrates the use of FRET laser signals to mirror the spatial disparities within the hydrogel network, which validate an anti-counterfeiting method utilizing this specific arrangement.
Chapter 7 concludes the thesis and suggests directions for future work.

Chapter 2: Background and Literature Review

In this chapter, we offer a succinct overview of the current applications of biological microlasers in the realm of sensing, supplemented by an introductory discussion on hydrogels and anti-counterfeiting measures for comprehensive understanding. The mechanics of laser operation, specifically focusing on Fabry-Perot (FP) and whispering gallery mode (WGM) cavities - the primary types utilized in this dissertation, are also examined in detail. The discourse initiates with an exploration of biological microlaser-assisted biosensing applications, followed by an evaluative review of hydrogels and anti-counterfeiting technologies. Concluding the chapter, the operation principles of Fabry-Perot (FP) and whispering gallery mode (WGM) laser cavities are individually analyzed and discussed.

2.1 Microlaser

Since Theodore Maiman's inaugural creation of the laser in 1960, the evolution and expansion of laser technology has been a continuous focal point in the scientific community. Progressive technological advancements over the past several decades have effectively transitioned research focus from macroscale to microscale, and even down to the nanoscale, and this trend has been clearly mirrored in the evolution of laser technology. Novel techniques, such as the establishment of microscale cavities including FP cavities and WGM cavities, have not only retained the unique advantages inherent to traditional laser technology but have propelled it to an advanced level. This has manifested the applicability of microlasers as potent tools in a multitude of fields, such as in biology and medicine. For instance, as shown in Fig.2.1a, this study identifies the mechanism governing transverse mode frequencies in cellular lasers[3], linking cell morphology to lasing frequencies through hyperspectral imaging. It applies this understanding to analyze cell adhesion and classification, opening new avenues for subcellular analysis in biophotonics. Moreover, as displayed in Fig 2.1b, FP cavities of microscale cavity length have shown promise in the realm of cancer diagnostics with patient tissue. The ability of these microscale FP cavities to accurately diagnose

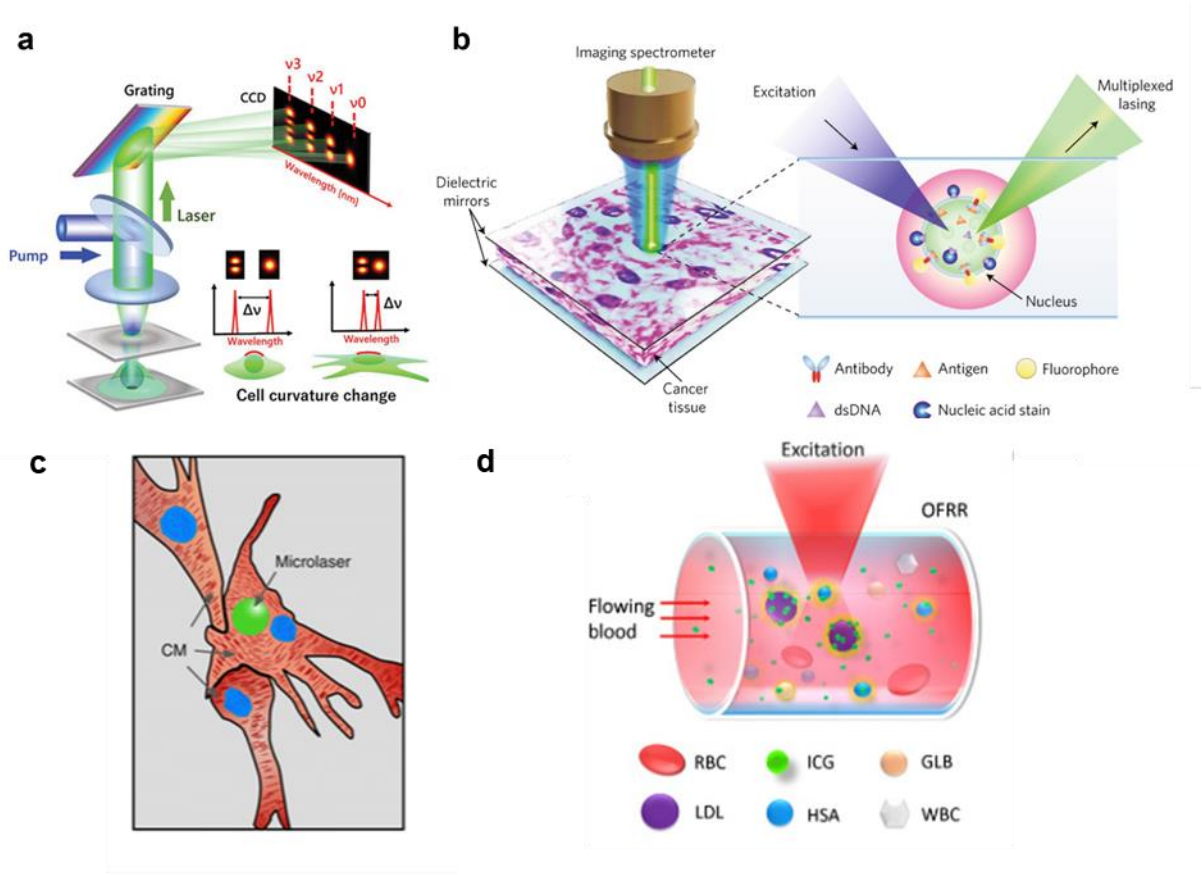

Figure 2.1 Schematic diagram of microlaser applications. **(a)** Cellular feature revealed by FP laser[3]. **(b)** For cancer diagnosis[4]. **(c)** For cell pulse detection[5]. **(d)** WGM lasing for detection of proteins in human blood[1].

cancer denotes a significant leap forward in early cancer detection and personalized treatment planning, reinforcing the transformative role of laser technology in modern medicine. Besides FP cavity laser, WGW laser also plays an important role in this field. For instance, as illustrated in Fig.2.1c, microlaser signals generated from a microsphere surrounded by cardiomyocytes have proven capable of reflecting the cellular pulse[5]. This remarkable capability suggests a potential revolutionary approach in the real-time monitoring and understanding of cardiomyocyte behavior at the microscale. Optical fiber is also famous for generating WGM laser for sensing. As shown in Fig.2.1d, this research[1] introduces the first successful demonstration of Indocyanine Green (ICG) lasing in human serum and whole blood at clinically safe concentrations and intensities, leveraging the unique properties of optofluidic lasers for enhanced detection sensitivity and imaging contrast. By analyzing ICG laser

emission across different serological components, it identifies the essential factors for lasing, setting the stage for advanced clinical and biomedical applications that could improve upon traditional fluorescence-based methods.

2.2 Gain Material in Microlaser

Photoluminescent or fluorescent materials hold considerable potential as gain materials for lasing, a fact that is exemplified in a variety of contexts. Fig.2.2a displays the manifestation of a WGM microlaser, which is generated from aggregated quantum dots, thereby highlighting the prospective use of these nanoscale semiconducting particles as gain material[6]. Furthermore, two-dimensional materials are increasingly being recognized as intriguing gain materials for the fabrication of adjustable or responsive microlasers. As an example[7], Fig.2.2b showcases how these atomically thin layers can be manipulated to generate tunable laser emissions.

Organic compounds, particularly dyes, have also proven to be of immense importance in the realm of lasing materials. The ease with which these materials can be conjugated with various molecules enables them to fulfill a range of sensing or

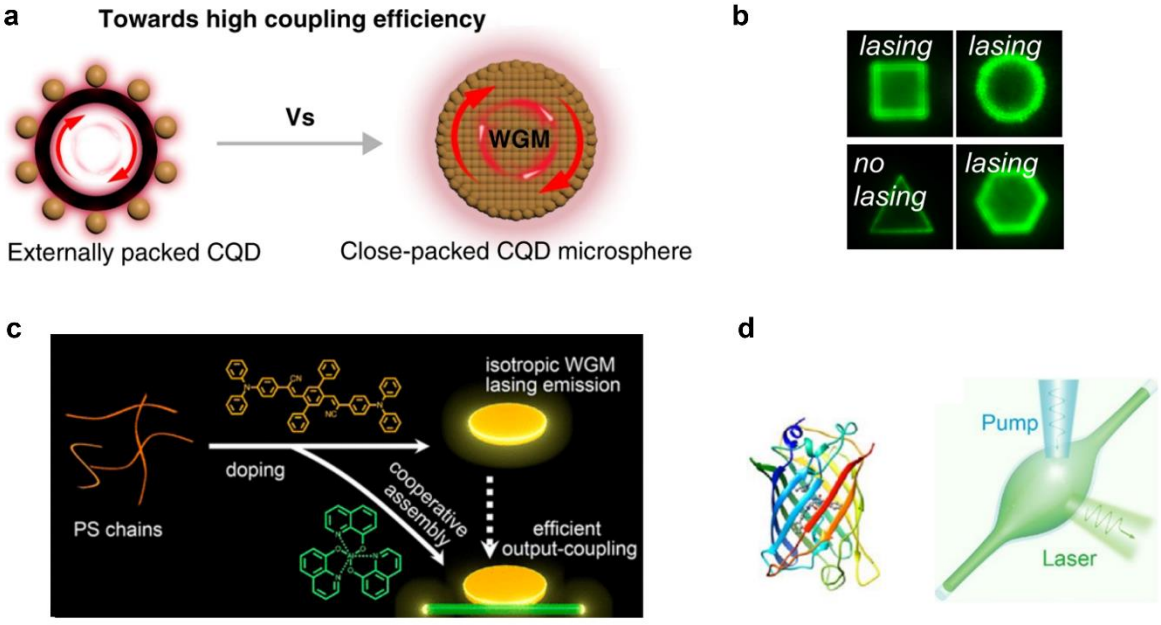

Figure 2.2 Schematic diagrams of different gain materials. **(a)** quantum dots[6]. **(b)** Two dimensional materials[7]. **(c)** Organic dyes[8]. **(d)**Green fluorescent protein[9].

detection tasks, as depicted in Fig.2.2c[8]. Lastly, there has been a significant surge of interest in biological materials as lasing gain materials, owing to their high biocompatibility and diverse range. The green fluorescent protein, as illustrated in Fig.2.2d, is one such biological material that has been extensively employed to generate laser signals[9]. The advent of these biological materials has injected new vigor into the field of microlaser research, opening up fresh avenues of exploration and potential applications.

2.3 Introduction of Biological Microlaser

Biological microlasers have recently garnered substantial interest and emerged as a groundbreaking tool applicable to a variety of fields, including sensing, imaging, and molecular analysis. Similar to other types of microlasers, a biological microlaser also comprises three fundamental components: the gain medium, optical cavity, and pumping light. What sets the biological microlaser apart from traditional lasers, however, is its unique gain medium. In contrast to conventional lasers that typically employ semiconductors or crystals as the gain medium, biological microlasers utilize

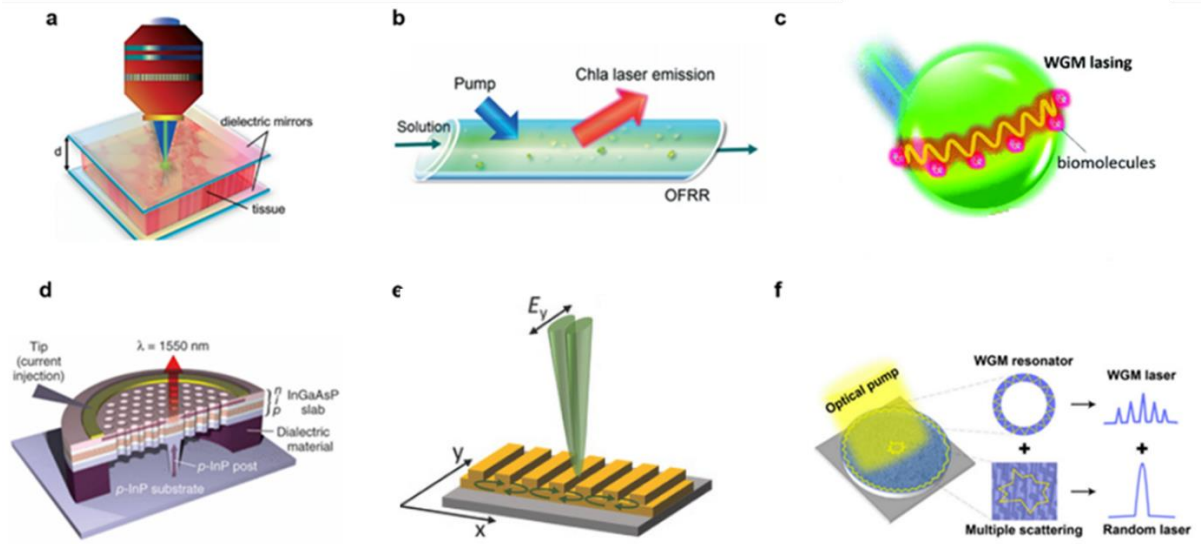

Figure 2.3 Biological microlasers with different optical cavities. **(a)** Fabry-Perot mirror cavity.[10] **(b)** Optofluidic ring resonator.[11] **(c)** Microsphere/droplet based whispering gallery mode laser.[12] **(d)** Photonic crystal based biological microlaser integrated with microfluidics.[13] **(e)** Distributed feedback biological microlaser.[14] **(f)** Random laser without external cavity.[15]

biological materials such as DNA, proteins, and cells[10-15].

In recent decades, rapid advancements in fabrication methodologies have led to the discovery of numerous cavities capable of generating laser signals from biological samples. Examples include the Fabry-Pérot (FP) cavity, ring resonator, microsphere resonator, photonic crystal, distributed feedback laser cavity, and random laser, as depicted in Fig.2.3. The utilization of these resonant structures has significantly broadened the application scope and enhanced the performance characteristics of biological microlasers, cementing their importance in modern optoelectronic devices and biophotonic research.

One of the key attributes of biological microlasers is their remarkable sensitivity, which offers a clear advantage over traditional fluorescence-based detection methods, as illustrated in Fig.2.4. Conventionally, fluorescent detection involves conjugating fluorophores with an analyte, and any alterations in the analyte, such as structural or environmental changes, are reflected in the fluorescent signal. However, this approach, which relies on spontaneous emission, has several limitations. One of the most substantial challenges is that minuscule changes within the analyte may go undetected due to overwhelming background noise inherent in fluorescent measurements. Contrastingly, laser-based detection employs an optical cavity. Here, fluorophores, serving as the gain medium, are situated within this cavity to generate laser emission, which then carries information from within the analyte. In comparison to fluorescence, the presence of an optical cavity allows even minor variations in the gain medium to be substantially amplified due to the robust optical feedback from the cavity. This results in noticeable alterations in the output emission signals, including parameters such as intensity, lasing threshold, emission directionality, and spatial mode distribution. Recent theoretical analysis and empirical findings have highlighted the unique advantages of biological microlasers, such as signal amplification, narrow linewidth, and intense output devoid of background fluorescence or scattering. This leads to a significant enhancement in detection sensitivity and improved signal-to-noise ratios (SNR) compared to fluorescence-based detection methods. Furthermore,

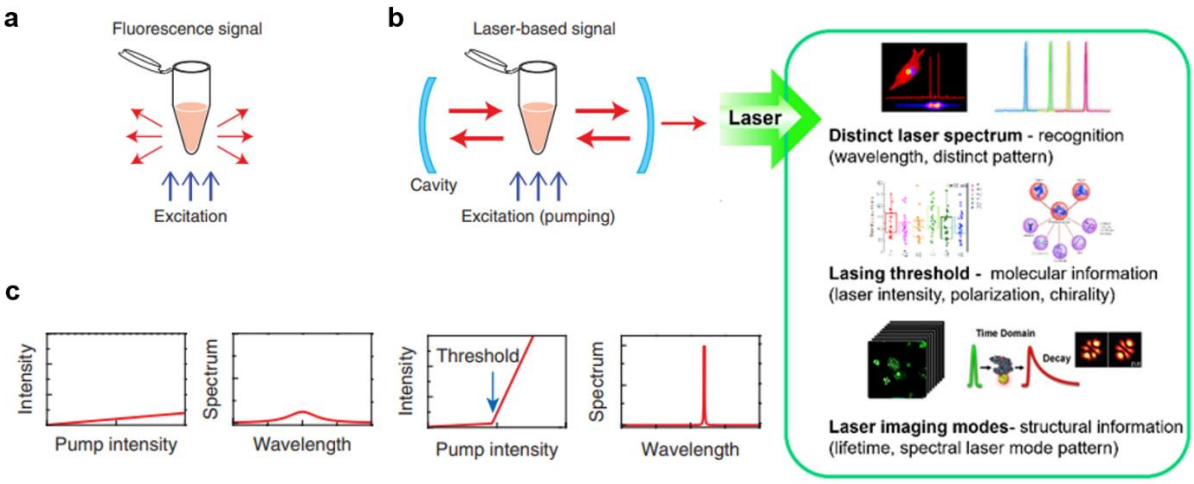

Figure 2.4 Comparison between conventional fluorescence-based and laser-based detection. **(a)** Fluorescence-based method does not have threshold behavior and the spectrum is usually very broad. **(b)** Laser-based method has many characteristics which are different from those of fluorescence emission including provides a lasing threshold and narrow linewidth.[16] **(c)** Differences of spectra performances between laser and fluorescence.

the augmented sensitivity and multi-dimensional analytical capabilities of biological microlasers permit the analysis of minute changes in biomolecules, cells, and tissues. This positions biological microlasers as a powerful tool with enormous potential for diverse biological and medical applications.

2.4 Biological Microlaser in Biosensing

Over the past several years, biological microlasers have become an area of rigorous investigation. The inaugural instance of a biological microlaser was the single-cell laser reported in 2011 (Fig.2.5a)[17]. In this scenario, the green fluorescent proteins (GFP) within the cell were able to achieve lasing, facilitated by the strong optical feedback from a highly reflective mirror. Later research demonstrated intracellular lasing based on whispering gallery mode (WGM) principles. Here, a glass bead was absorbed by a HeLa cell[18], resulting in successful lasing generation within the cell (Fig.2.5b). This study eliminated the constraints of high reflective mirrors and showcased the potential of implantable biological microlaser sensors.

Beyond organic dyes, semiconductor materials have also found applications in biological microlasers. An example of this is the cadmium sulfide (CdS) nanowire

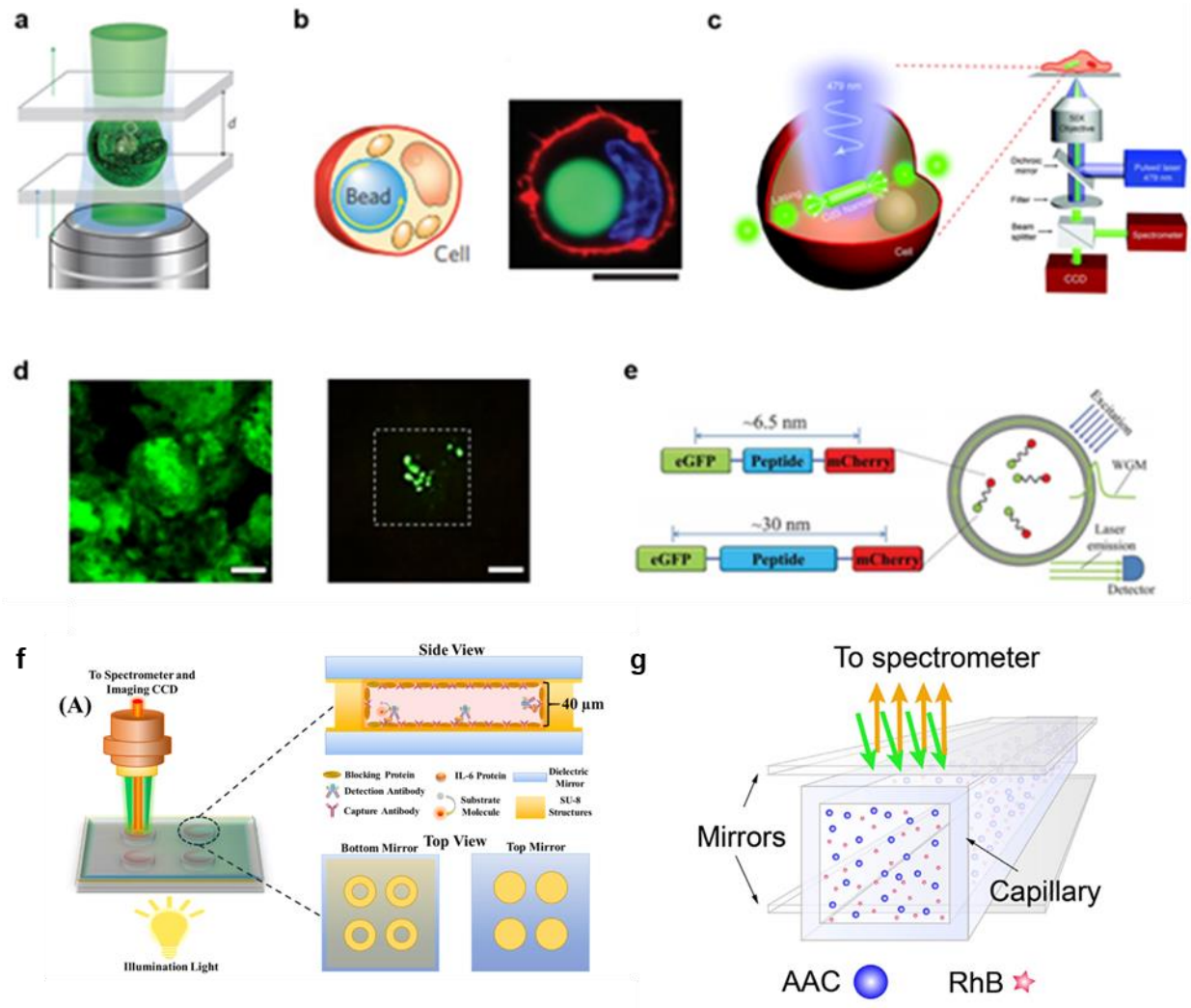

Figure 2.5 Biological microlasers in biosensing. **(a)** Single cell laser.[17] **(b)** Intracellular WGM laser.[18] **(c)** Intracellular nanowire laser.[19] **(d)** Biological microlaser used for cancer screening.[4] **(e)** Fluorescent protein FRET laser.[20] **(f)** Biological laser from antibody reaction[16]. **(g)** Biological laser achieved from capillary[22].

laser[19], which functioned as a standalone intracellular probe (Fig.2.5c). Biological microlasers' potential extends beyond single-cell applications to achieve functionalities at the tissue level. A case in point is the use of biological microlasers to diagnose and locate cancer cells within tissue (Fig.2.5d), demonstrating the significant potential of biological microlasers in the biomedical field[4].

Finally, Forster resonance energy transfer (FRET) biological microlasers have been achieved using protein pairs (Fig.2.5e). In this scenario, the lasing efficiency could be modulated via the underlying protein interactions[20]. Biological laser used

to reflect antibody reaction is also reported (Fig.2.5f). Tan[21] developed an on-chip enzyme-linked immunosorbent assay (ELISA) laser platform enhances biochemical analysis with its high sensitivity and efficiency, achieving a detection limit of 0.1 pg/mL for IL-6 in just 1.5 hours using minimal sample volumes Besides, Yang[22] introduced a highly sensitive approach for biomarker detection (Fig.2.5g) by incorporating immunoreactions within a laser cavity, significantly enhancing detection sensitivity. It achieves a remarkable limit of detection of 1.8×10^{-10} g/L and operates across a wide dynamic range, offering a rapid, cost-effective, and simple method for disease diagnostics without the need for complex processing or large sample volumes.

2.5 Laser Mechanism and Optical Cavity

2.5.1 Einstein Equation

In a two-energy-level system, where E_1 represents the ground state (lower energy level) and E_2 denotes an excited state (higher energy level), we have a certain number of molecules, N_1, at the E_1 level, and N_2 molecules at the E_2 level. The energy of the photon emitted during the transition of molecules from the higher to the lower energy state is given by $h\upsilon = E_2 - E_1$, where h is Planck's constant and v is the frequency of the photon. Spontaneous emission refers to the phenomenon wherein molecules at the higher energy level E_2 spontaneously transition to the lower energy level E_1, resulting in the release of photons. This process is governed by a characteristic decay rate of the excited state. In other words, the number of excited molecules that spontaneously decay per unit time is represented by this decay rate. The intrinsic property of the system, the decay rate of the excited state, can thus be expressed as follows:

$$\frac{dN_2(t)}{dt} = -A_{21}N_2(t) \qquad (2.1),$$

where A_{21} is the spontaneous transition coefficient while spontaneous emission lifetime equals to $\tau = 1/A_{21}$.

At the same time, photons can be absorbed by the lower energy level:

$$\frac{dN_1(t)}{dt} = -B_{12}N_1(t)\rho(\nu_0) \quad (2.2),$$

where B_{12} is the absorption coefficient and $\rho(\upsilon)$ is the excitation photon density. Moreover, a photon with an energy equivalent to the energy difference between E_2 and E_1, denoted as E_2 - E_1, can instigate a stimulated emission. This process triggers the transition of molecules from the excited state E_2 to the ground state E_1, leading to the emission of an additional photon of energy E_2 - E_1. Remarkably, this newly emitted photon mirrors the stimulating photon in terms of wavelength, phase, polarization state, and propagation direction, thereby establishing a coherent state.

$$\frac{dN_2(t)}{dt} = -B_{21}N_2(t)\rho(\nu_0) \quad (2.3),$$

where B_{21} is the stimulated transition coefficient.

At equilibrium, the change rate of molecules at energy levels E_1, E_2 must be zero:

$$\left(\frac{dN_2(t)}{dt}\right)_{st} + \left(\frac{dN_2(t)}{dt}\right)_{sp} = \left(\frac{dN_1(t)}{dt}\right)_{abs} \quad (2.4)$$

$$A_{21}N_2(t) + B_{21}N_2(t)\rho(\nu_0) = B_{21}N_2(t)\rho(\nu_0) \quad (2.5)$$

$$\frac{N_2}{N_1} = \frac{B_{12}\rho(\nu_0)}{A_{21} + B_{21}\rho(\nu_0)} \quad (2.6)$$

Considering the that the distribution of the system's particles to various energy level obeys Boltzmann Distribution, the relationship between N_1 and N_2 can be expressed as:

$$\frac{N_2}{N_1} = \frac{g_2}{g_1}\exp\left(-\frac{E_2 - E_1}{kT}\right) \quad (2.7)$$

where g_1 and g_2 are the degenerate degree of E_1 and E_2, respectively. From the blackbody radiation:

$$\rho(\nu) = \frac{8\pi n^3 h\nu^3}{c^3} \frac{1}{e^{h\nu/k_b T} - 1} \tag{2.8}$$

Therefore, the Einstein's relation becomes:

$$\frac{A_{21}}{B_{21}} = \frac{8\pi n^3 h\nu^3}{c^3} \tag{2.9}$$

2.5.2 Rate Equation and Population Inversion

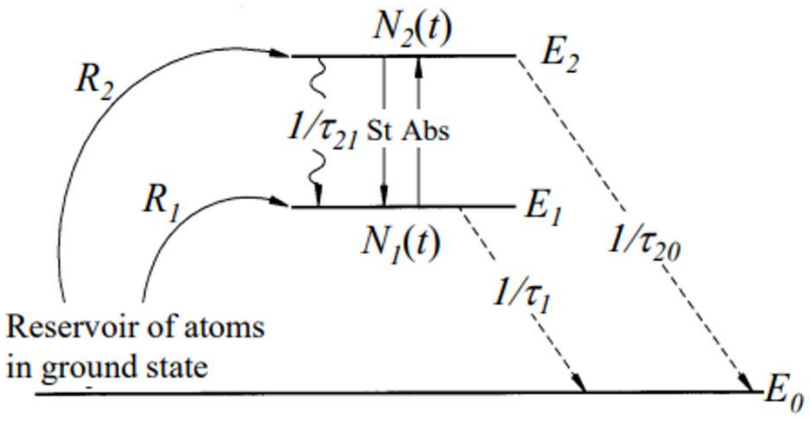

Figure 2.6 Schematic diagram of three energy level

When considering a three-level system in steady-state, as illustrated in Fig 2.6, we can proceed with its description through the coupled rate equations. This steady-state condition implies that the population of each energy level in the system remains constant over time. Therefore, the rate at which atoms or molecules transition into a given energy level equals the rate at which they transition out of that same level. Consequently, this leads to a set of coupled differential equations that can be solved to describe the behavior of the system.

$$\frac{dN_2}{dt} = R_2 - \frac{N_2}{\tau_2} - \frac{\sigma_e I}{h\nu}(N_2 - N_1) = 0 \tag{2.10}$$, and

$$\frac{dN_1}{dt} = R_1 + \frac{N_2}{\tau_{21}} - \frac{N_1}{\tau_1} + \frac{\sigma_e I}{h\nu}(N_2 - N_1) = 0 \quad (2.11),$$

where R_1 and R_2 are the pump rate for energy level E_1 and E_2, respectively. The decay rate of state E_1 is $1/\tau_1$, the total decay rate of state E_2 is $1/\tau_2 = 1/\tau_{21} + 1/\tau_{20}$.

By solving the Equations (2.10) and (2.11), we obtained:

$$\Delta N_1 = \left[R_1 \left(\frac{1}{\tau_2} + \frac{\sigma_e I}{h\nu} \right) + R_2 \left(\frac{1}{\tau_{21}} + \frac{\sigma_e I}{h\nu} \right) \right] \quad (2.12), \text{ and}$$

$$\Delta N_2 = \left[R_2 \left(\frac{1}{\tau_1} + \frac{\sigma_e I}{h\nu} \right) + R_1 \left(\frac{\sigma_e I}{h\nu} \right) \right] \quad (2.13)$$

$$\Delta = \frac{1}{\tau_1 \tau_2} \left[1 + \left(\tau_1 + \tau_2 - \frac{\tau_1 \tau_2}{\tau_{21}} \right) \left(\frac{\sigma_e I}{h\nu} \right) \right] \quad (2.14).$$

The difference between two energy levels can be written as:

$$N_2 - N_1 = \frac{R_2 \tau_2 \left(1 - \frac{\tau_1}{\tau_{21}} \right) - R_1 \tau_1}{1 + \left(\tau_1 + \tau_2 - \frac{\tau_1 \tau_2}{\tau_{21}} \right) \left(\frac{\sigma_e I}{h\nu} \right)} \quad (2.15).$$

If we strive to achieve population inversion, which is a condition where $\Delta N > 0$, this state can be accomplished provided that the relaxation time τ_{21} is greater than τ_1. Assuming that the light intensity is small enough so that the denominator in Equation (2.15) would approximate to 1. Consequently, under such a scenario, the expression for the gain coefficient, which represents the increase in light intensity per unit distance in the medium, can be rewritten as follows:

$$\gamma_0(\nu) = \sigma_e(\nu) \left[R_2 \tau_2 \left(1 - \frac{\tau_1}{\tau_{21}} \right) - R_1 \tau_1 \right] \quad (2.16)$$

$$\frac{1}{I} \frac{dI}{dz} = \frac{\gamma_0(\nu)}{1 + I\nu / I_s} \quad (2.17)$$

If the ratio of τ_2 to τ_{21} approximates 1 ($\tau_2/\tau_{21} \sim 1$), the expression for the saturation intensity can be reformulated as follows:

$$I_s = \frac{h\nu}{\sigma_e(\nu)\,\tau_2}\,\frac{1}{1+\frac{\tau_1}{\tau_2}\left(1-\frac{\tau_1}{\tau_{21}}\right)} \sim \frac{h\nu}{\sigma_e(\nu)\,\tau_2} \tag{2.18}$$

It's crucial to note that when the light intensity equals the saturation intensity, the gain coefficient decreases to half its initial value.

2.5.3 Absorption and Emission Cross Section

Cross section serves as another significant parameter in laser principle, particularly in the understanding of the interaction between photons and the atoms or molecules of the gain medium in a laser. The cross-section essentially quantifies the probability of a specific interaction occurring between a photon and an atom or molecule, which is defined as the ratio between total absorbed (emitted) energy in unit time and the total excitation energy in unit time per unit area (cm^2):

$$\sigma = \frac{h\nu W_{abs}}{I} = \frac{h\nu B_{21}\rho(\nu_0)}{c\rho(\nu_0)} = \frac{h\nu B_{21}}{c} \tag{2.19}.$$

The absorption cross section, which represents the likelihood of an atom in the lower energy state absorbing a photon and transitioning to the higher energy state, was deduced by experiment results:

$$\sigma_a(\lambda) = 3.82\times 10^{-21}\varepsilon(\lambda) \tag{2.20},$$

where σ_a is the absorption cross section and ε is the extinction coefficient of particular gain material.

The emission cross section, representing probability of an atom in the excited state undergoing a transition to the lower energy state, either spontaneously or as stimulated emission, can be defined as:

$$\sigma_e(\lambda) = \frac{\lambda^4 E(\lambda)}{8\pi c n^2 \tau_f} \tag{2.21},$$

where σ_e is the emission cross section, τ_f is the spontaneous emission lifetime of material, and n is the refractive index of surrounding medium. In Equation (2.21), *E(λ)* is related to the quantum yield of the gain material, where $q = \int E(\lambda)\cdot d\lambda$

2.5.4 Fabry-Perot Resonators

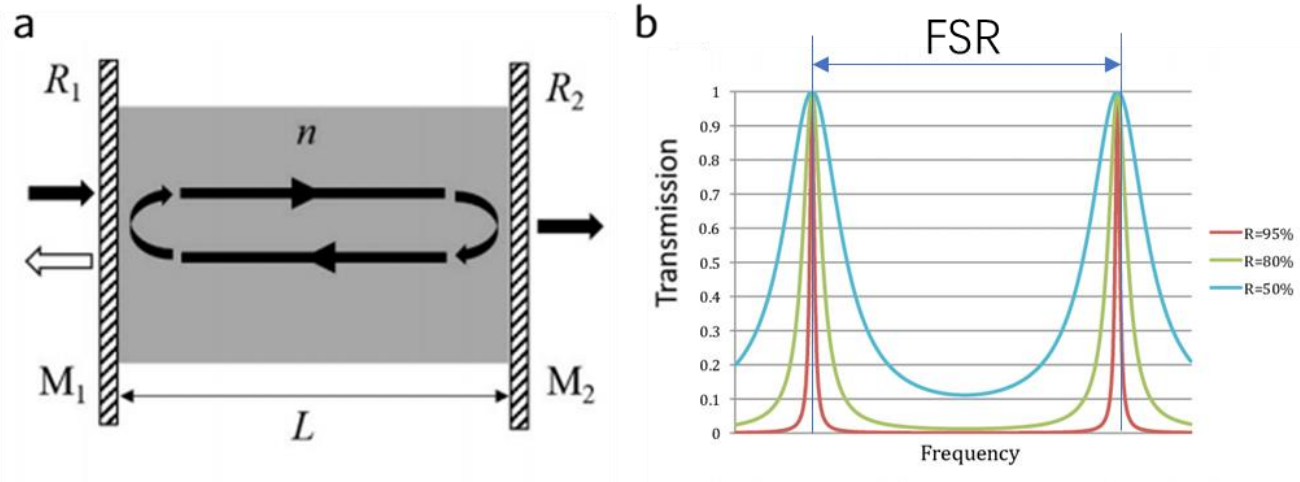

Figure 2.7 (a) Schematic of a Fabry-Perot cavity consisting of two parallel mirrors M_1 and M_2 with reflectance of R_1 and R_2, respectively, refractive index n and cavity length L. **(b)** Transmission of an FP cavity.[24]

The FP cavity, since the inception of laser technology, has remained one of the most extensively studied types of optical cavities.[23] Various forms of FP cavities have been fabricated using different materials and methods, such as metals, distributed Bragg reflectors (DBRs), and even interfaces between high and low refractive index materials, like in the case of nanowires. The operating principle of the FP cavity is depicted in Fig.2.7a, illustrating that light introduced into the cavity experiences multiple reflections between the two mirrors.

A fraction of this light is transmitted with each pass and can interfere constructively or destructively with the incident light. For the purpose of our analysis, we denote the cavity length as *L*. We assume both mirror have same reflectivity as r and different transmissivity as *t* and *t'* , respectively. Additionally, we define A_{in} as the amplitude of the incident electric field, and the phase difference as δ. Given these parameters, the transmitted wave's amplitude, denoted as A_t, can be represented as follows[21]:

$$A_t = tt'A_{in} + tt'r'^2 e^{i\delta} A_{in} + tt'r'^4 e^{i2\delta} A_{in} + \dots \quad (2.22),$$

which can also be written as:

$$A_t = \frac{T}{1 - Re^{i\delta}} A_{in} \quad (2.23),$$

where T represents the product of transmissivity and R is the cavity's overall reflectivity. Hence, the transmissivity, a key parameter in characterizing an optical system like the FP cavity, can be derived from the ratio of the transmitted or reflected light intensity to the incident light intensity:

$$\frac{I_t}{I_{in}} = \frac{A_t A_t^*}{A_{in} A_{in}^*} = \frac{(1-R)^2}{(1-R)^2 + 4R\sin^2\left(\frac{\delta}{2}\right)} \quad (2.24)$$

One can see that the transmissivity is dependent on phase difference δ.

$$\delta = \frac{2\pi}{\lambda} \Delta l = \frac{4n\pi L}{\lambda} \cos\theta \quad (2.25)$$

In the previous equation (2.25), Δl represents the optical path difference between two adjacent partial waves, θ denotes the incident angle, and n is the refractive index of the medium within the cavity. Proceeding from here, by substituting equation (2.25) into (2.24), the conditions for maximum transmission can be obtained. These conditions correspond to the resonance conditions within the FP cavity. The derived resonance conditions can be formulated as follows:

$$\delta = \frac{4\pi n L \cos(\theta)}{\lambda} = m2\pi \quad (2.26), \text{ and}$$

$$\frac{I_t}{I_{in}} = \frac{(1-R)^2}{(1-R)^2} = 1 \quad (2.27).$$

One of the crucial parameters characterizing an FP cavity is the Free Spectral Range (FSR), which is defined as the frequency interval between two adjacent resonant modes, namely, modes m and m-1, as illustrated in Fig 2.7b. The FSR reflects the cavity's ability to distinguish between closely spaced frequencies. In the context of an FP cavity, we can derive the formula for FSR from Equation (2.5) as follows:

$$\lambda_m = \frac{2nL}{m} \quad (2.28).$$

Besides, the cavity lifetime (τ_c) and quality factor (Q) are also two significant factor that can indicate the energy storage ability of a cavity:

$$Q = \omega \tau_c \quad (2.29),$$

$$\tau_c = \frac{2nL}{c \ln\left(R^2 (1 - \alpha L)^2 \right)} \quad (2.30).$$

In addition, the finesse (F) of the resonator is a dimensionless parameter that characterizes the sharpness of the resonance peaks of the Fabry-Pérot étalon. It is directly related to the spectral resolution of the étalon, with higher finesse values indicating sharper and more narrowly spaced peaks. The finesse is defined as the ratio of the Free Spectral Range (FSR) to the spectral width (δv_m) of the resonance:

$$F = \frac{FSR}{\delta v_m} \quad (2.31),$$

in which spectral width could be expressed as:

$$\delta v_m = \frac{c}{2nLF} \quad (2.32).$$

The finesse can also be related to the reflectivity (R) of the mirrors. Assuming the étalon is air-spaced and losses other than mirror reflectivity are negligible, the finesse can be approximated by:

$$F \approx \frac{\pi \sqrt{R}}{1 - R} \quad (2.33).$$

2.5.5 Whispering Gallery Mode Cavities

Whispering Gallery Modes (WGMs) are a type of wave resonance where light waves propagate around a circular or spherical structure, trapped by continuous total

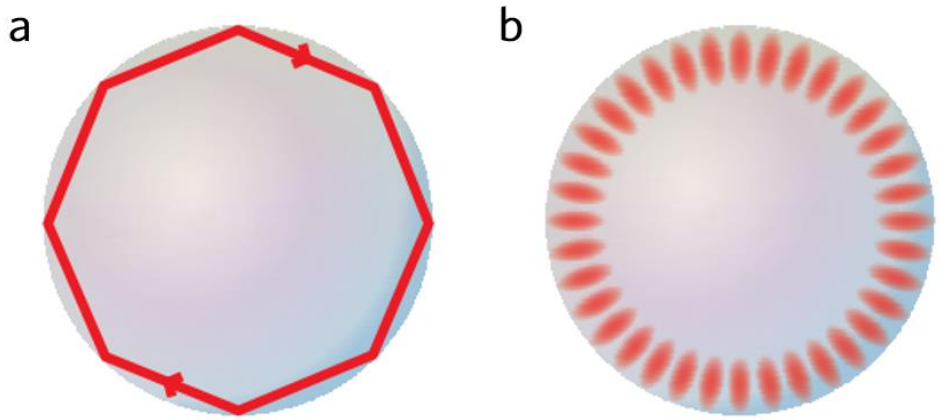

Figure 2.8 (a) Geometrical optics representation of whispering gallery modes. **(b)** Wave optics representation of whispering gallery modes.[26]

internal reflection. They are commonly observed in micro-resonators, such as microspheres, microdisks, or microtoroids.[25] In such WGM structures, the internal material possesses a higher refractive index compared to the external surroundings. As a result, light is trapped within the structure due to total internal reflection occurring at the boundary of the circular architecture. When this trapped light completes a full round-trip and returns to its original position in phase, a condition known as resonance is achieved. This resonant condition gives rise to a standing wave pattern, an attribute that characterizes the WGM. Here we considered a 3-dimensional microsphere as the cavity to support WGM.

Microsphere-based WGM cavities, as depicted in Fig.2.8, can concurrently sustain both Transverse Magnetic (TM) modes and Transverse Electric (TE) modes.

For simplicity, the wavelengths at which resonance occurs comply with the following equation:

$$m\lambda = 2\pi R n_{eff} \tag{2.34}$$

To determine the electric field distribution and the precise resonant wavelengths in Whispering Gallery Mode (WGM) cavities, the electric fields can be represented as follows:

$$E(r.t) = E_0 e^{i(k \cdot r - \omega t)} \tag{2.35}$$

Using Equation (2.32) with Maxwell's equations, which govern the behavior of electric and magnetic fields, one can derive the wave equation that describes light propagation in dielectric materials. This can be formulated as follows:

$$\nabla^2 E(r,t) = -k^2 E(r,t) \tag{2.36}$$

Here, *k* represents the wave vector, which is equivalent to the product of the refractive index *n* and the angular frequency *ω*, divided by the speed of light *c*. In spherical coordinates, we propose that *ψ* is the solution to the scalar Helmholtz equation, which can be expressed as follows:

$$\nabla^2 = \frac{1}{r^2}\frac{\partial}{\partial r}\left(r^2\frac{\partial \psi}{\partial r}\right) + \frac{1}{r^2 \sin^2\phi}\frac{\partial^2 \psi}{\partial \theta} + \frac{1}{r^2 \sin\phi}\frac{\partial}{\partial \phi}\left(\sin\phi\frac{\partial \psi}{\partial \phi}\right) \tag{2.37}$$

By separating the variables, one can obtain the solution[26]:

$$\psi(r,\theta,\phi) = \mathrm{R(r)}\Theta(\theta)\,\Phi(\phi) \tag{2.38}$$

$$\Phi = \frac{1}{\sqrt{2\pi}} e^{\pm im\phi} \tag{2.39}$$

$$\Theta = P_l^m(\cos\theta) \tag{2.40}$$

$$\Theta(\theta)\,\Phi(\phi) = Y_l^m(\theta,\phi) \tag{2.41}$$

$$\frac{d}{dr}\left(r^2\frac{dR(r)}{dr}\right) + \left(k^2 r^2 - l(l+1)\right)R(r) = 0 \tag{2.42}$$

where *l* and *m* are the azimuthal and angular mode numbers of WGM, and P_l^m and Y_l^m are the Legendre polynomial and spherical harmonics:

$$\begin{aligned} P_l^m(x) &= (1-x^2)^{m/2}\frac{d^m}{dx^m}P_l(x) \\ P_l(x) &= \frac{1}{2^l l!}\frac{d^l}{dx^l}(x^2-1)^l \end{aligned} \tag{2.43}$$

$$Y_l^m(\theta,\phi) = \frac{1}{\sqrt{2\pi}} e^{\pm im\phi} P_l^m(\cos\theta) \tag{2.44}$$

The solution of Equation (2.39) can be described as spherical Bessel functions:

$$J_l(kr) = \sqrt{\frac{\pi}{2kr}} J_{j+1/2}(kr)$$
$$Y_l(kr) = \sqrt{\frac{\pi}{2kr}} Y_{j+1/2}(kr) \tag{2.45}$$

The spherical Hankel functions can be expressed as:

$$H_l^{(1)} = J_l(kr) + iY_l(kr)$$
$$H_l^{(2)} = J_l(kr) - iY_l(kr) \tag{2.46}$$

J_l and H_l are the spherical Bessel function and spherical Hankel function. Hence the exact resonant mode wavelengths can be described as[27]:

$$\frac{1}{\lambda}(R, n_l, n_{eff}, r, m) = \frac{1}{2\pi R n_l}[m + \frac{l}{2} + \alpha(r)\sqrt[3]{\frac{m+\frac{1}{2}}{2}} - \frac{L}{\left(n_{eff}^{\ 2} - 1\right)^{1/2}}$$
$$+ \frac{3}{10}\alpha^2(r)\sqrt[-3]{\frac{m+\frac{1}{2}}{4}} - 2^{-1/3}(n_{eff}^{\ 2} - \frac{2}{3}L^2)\frac{\alpha(r)(m+\frac{1}{2})^{-2/3}}{\left(n_{eff}^{\ 2} - 1\right)^{3/2}}] \tag{2.47}$$

This equation illustrates that the resonant wavelength λ is contingent upon various factors including the radius R of the cavity, the internal and external refractive indices n_1 and n_2, the radial mode number r, and the angular mode number m. The effective refractive index, denoted as n_{eff}, is defined as the ratio of the refractive index of the cavity (n_1) to that of the surrounding environment (n_2), when $n_{eff} = n_1/n_2$. The parameter L is given by $1/n_{eff}$ and n_{eff} for Transverse Magnetic (TM) and Transverse Electric (TE) modes, respectively. $\alpha(r)$ represents the solution of the Airy function.

The Quality factor (Q factor) of WGM cavities, a measure of the energy loss rate relative to the stored energy, can be computed as follows:

$$Q = \frac{Re(\omega)}{2 \times |Im(\omega)|} \tag{2.48}$$

The formula of Q factor can be simply expressed as:

$$Q = \frac{L\left(n_{eff} - \frac{1}{n_{eff}}\right)}{2\left(\sqrt{\frac{2\mu_0}{l+1/2}} - \frac{1}{4\mu_0}\right)} e^{\frac{4\mu_0}{3}\sqrt{\frac{2\mu_0}{l+1/2}}} \tag{2.49}$$

where the parameter L equals $1/n_{\text{eff}}$ and n_{eff} for TM modes and TE modes. The $\mu_0 = l + \frac{1}{2} - \frac{2\pi R}{\lambda}$ at the resonant wavelengths.

2.6 FRET Efficiency and Förster Distance

Fluorescence Resonance Energy Transfer (FRET) is a distinctive non-radiative process where the emission or absorption of a photon is not involved during the energy exchange. It's commonly understood as a dipole-dipole interaction taking place between two molecular entities: the energy donor and the acceptor.

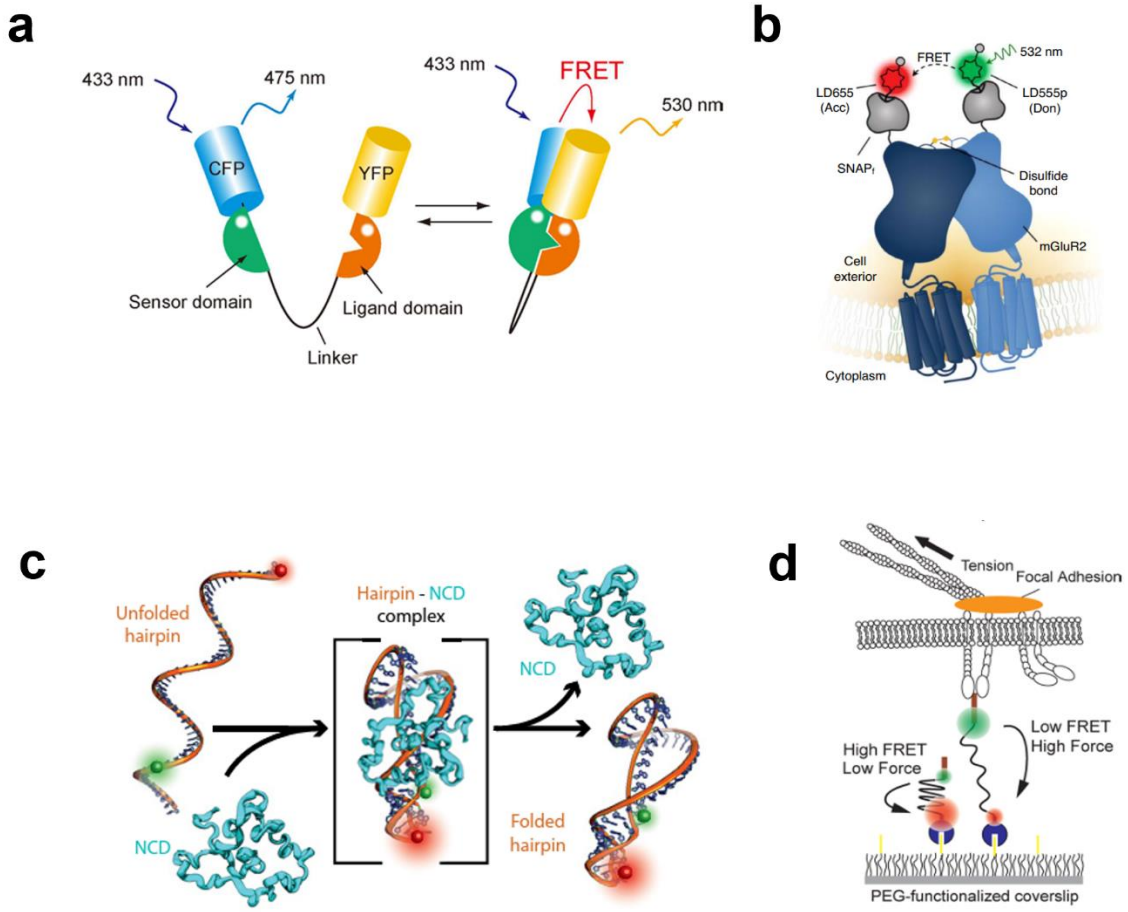

Figure 2.9 Schematics diagrams of FRET applications. **(a)** For biomolecular interaction detection[28]. **(b)** For cell signal transduction[29]. **(c)** For visualization of protein folding dynamics[30]. **(d)** For cell force mapping[31].

FRET is characterized by its strong dependence on distance, wherein an energized donor molecule non-radiatively couples with an adjacent acceptor molecule to transmit energy. The efficacy of this energy transfer exhibits an inverse relationship with the sixth power of the distance separating the donor and acceptor. This unique characteristic positions FRET as a potent spectroscopic tool capable of measuring distances at the nanoscale. FRET not only serves as a valuable spectroscopic tool but also plays a vital role in numerous biophysical and biological phenomena, including protein folding dynamics, cellular signal transduction, and intercellular communication. Its wide-ranging applications extend to the realms of biosensing, molecular imaging, and exploration of biomolecular interactions[28-31] (Fig.2.9). The strategic selection of the donor-acceptor pair and the precise control of their spatial alignment can leverage FRET to yield invaluable insights into the structural intricacies and dynamism of biological systems.

Next, we will introduce FRET theoretically, the energy transfer rate from the donor to the acceptor is given by:

$$k_F(r) = \frac{1}{\tau_d}\left(\frac{R_0}{r}\right)^6 \tag{2.50},$$

in which R_0 refers to the Förster distance where the FRET efficiency is 50%.

The equation of R_0 is given by:

$$R_0 = \sqrt[6]{\frac{9\ln(10)\,k^2\phi_d}{128\pi^5 N_A m^4}\int_0^\infty F_d(\lambda)\,\varepsilon_a(\lambda)\,\lambda^4 d\lambda} \tag{2.51},$$

In this context, k^2 is the orientation factor between the donor and acceptor dipoles, typically assumed to be 2/3 under the assumption of random orientation. Φ_d signifies the quantum yield of fluorescence of the donor molecules. N_A represents Avogadro's number, while m stands for the refractive index of the medium in which the energy transfer occurs. Furthermore, $F_d(\lambda)$ denotes the normalized fluorescence emission intensity of the donor, and $\varepsilon_a(\lambda)$ signifies the molar absorption coefficient (or extinction coefficient) of the acceptor, with the units of $M^{-1}cm^{-1}$. The overlap integral, which

represents the degree to which the donor emission spectrum overlaps with the acceptor absorption spectrum, can be calculated as follows:

$$\int_0^\infty F_d(\lambda)\,\varepsilon_d(\lambda)\,\lambda^4 d\lambda \qquad (2.52),$$

where the integral is taken over all wavelengths (λ). The overlap integral is critical for FRET efficiency, as it determines how effectively the donor can transfer energy to the acceptor. A larger overlap integral indicates a higher probability of energy transfer.

The efficiency of FRET, denoted as E, is a key parameter that quantifies the fraction of energy transferred from the donor to the acceptor. It is defined as:

$$E = \frac{1}{1+\left(\frac{R}{R_0}\right)^6} \qquad (2.53),$$

where R is the distance between the donor and acceptor, R_0 is the Förster distance, where the efficiency is 50%.

The lifetime of the donor fluorescence in the presence (τ_{DA}) and absence (τ_D) of the acceptor provides another way to quantify FRET efficiency:

$$E = 1 - \frac{\tau_{DA}}{\tau_D} \qquad (2.54),$$

where τ_{DA} is the donor lifetime in the presence of the acceptor, τ_D is the donor lifetime in the absence of the acceptor.

Indeed, FRET efficiency can also be calculated by measuring fluorescence intensities. This method relies on comparing the change in donor fluorescence intensity in the presence and absence of the acceptor. The FRET efficiency can be represented by the following equation:

$$E = 1 - \frac{I_{DA}}{I_D} \qquad (2.55),$$

where I_{DA} is the donor fluorescence intensity in the presence of the acceptor, I_D is the donor fluorescence intensity in the absence of the acceptor.

2.7 Hydrogel

2.7.1 Hydrogel Formation

Hydrogels, three-dimensional networks comprised of hydrophilic polymers, are fascinating materials that have found widespread applications in various fields such as drug delivery, tissue engineering, and anti-counterfeiting technology, to name a few. Their versatility stems from their unique properties, which include high water content, tunable mechanical strength, and the ability to respond to environmental stimuli such as pH, temperature, and light.

The formation of hydrogels typically involves the polymerization of hydrophilic monomers in the presence of a crosslinking agent. Two primary techniques used for hydrogel synthesis are the step growth polymerization and free radical polymerization. The choice of polymerization method (Fig.2.10) can significantly influence the structure and properties of the resulting hydrogel. In step-growth polymerization, reactive groups on the monomer molecules react with each other to form the polymer network. This method typically results in hydrogels with uniform network structures but may require longer polymerization times and careful control of reaction conditions. On the other hand, free radical polymerization involves the generation of free radicals, typically through the decomposition of a radical initiator under heat or light. The free radicals then initiate the polymerization of the monomers, leading to the formation of the polymer network. This method tends to produce hydrogels with more heterogeneous network structures but can be completed much faster compared to step growth polymerization.

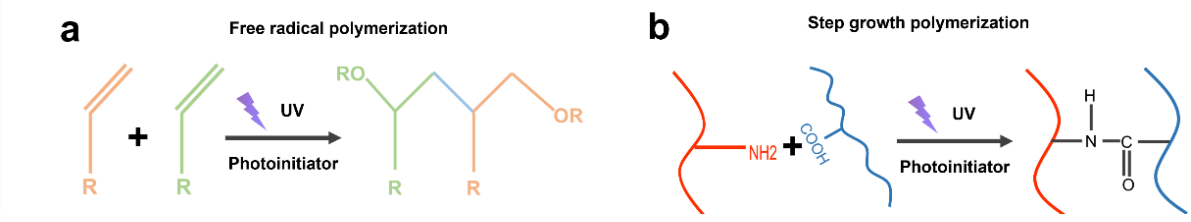

Figure 2.10 schematic showing the polymerization process. **(a)** Free radical polymerization. **(b)** Step growth polymerization

Importantly, the characteristics of the hydrogel, including its porosity, mechanical strength, and response to stimuli, can be finely tuned by manipulating the polymerization conditions, such as the concentration of the monomers and the concentration and type of crosslinking agent, and the polymerization time and temperature. Consequently, a wide variety of hydrogels with distinct properties can be synthesized to suit different applications. With ongoing research and development, the potential applications of hydrogels continue to expand, making them a subject of keen interest in material science and bioengineering.

2.7.2 Hydrogel Applications

Hydrogels have been a prominent focus of research in recent years due to their excellent biocompatibility and diverse potential applications in biosensing and biomedical fields[32]. Hydrogels' unique composition, characterized by functional groups on side chains (like amine or carboxyl groups), makes them amenable to various chemical modification that facilitate multifunctionality. One key principle inside

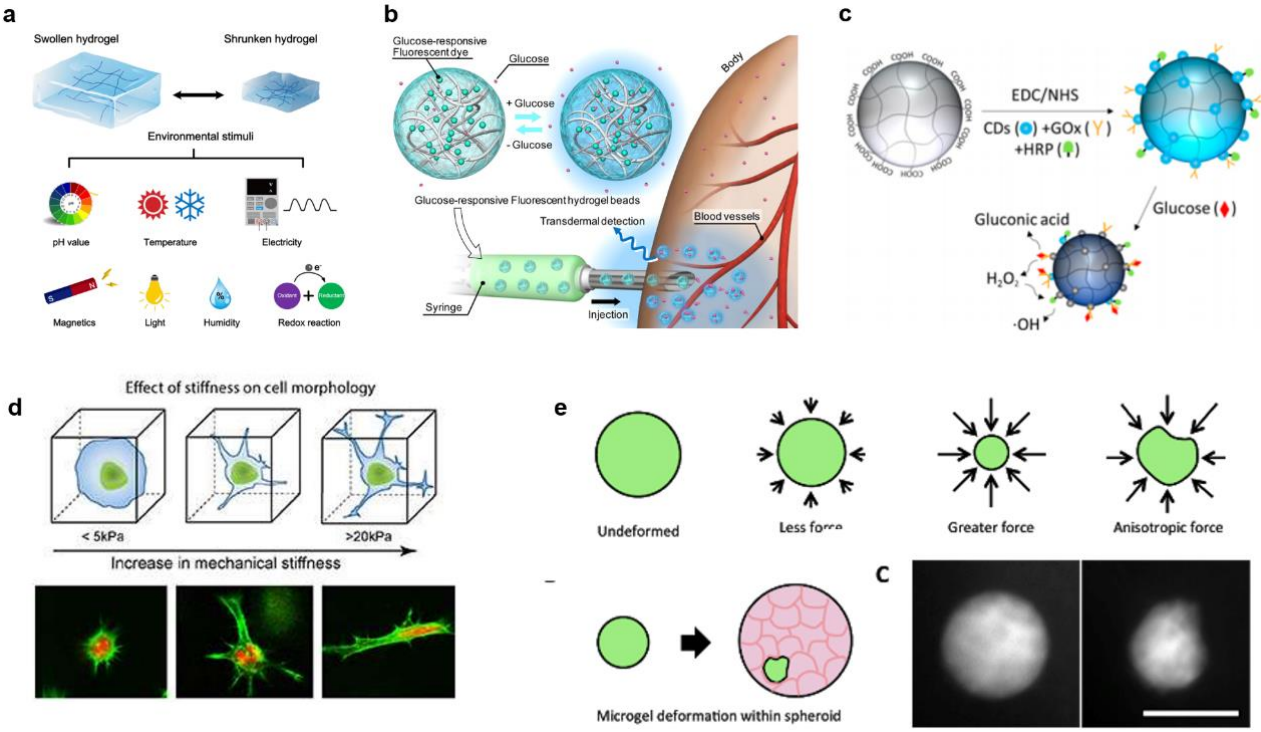

Figure 2.11 Various functions of hydrogel. **(a)** Different kinds of stimuli responsive hydrogel.[33] **(b)**Injectable hydrogel glucose sensor.[34] **(c)** pH responsive hydrogel glucose sensor.[35] **(d)** Hydrogel be used as ECM material.[36] **(e)** Concepts of using hydrogel as force sensors inside tumor spheroid.[37]

hydrogel-based sensors is the responsiveness of these side-chain groups to environmental stimuli[35], as depicted in Fig.2.11a.

A salient example of this principle in action is the development of hydrogel-based glucose sensors. Fig.2.11b illustrates the design of an injectable hydrogel glucose sensor, wherein a functional group on the hydrogel microsphere's chain reacts with glucose molecules to emit blue fluorescence[36]. An alternative approach, as represented in Fig.2.11c, involves monitoring the changes in the external environment triggered by the interaction between glucose and glucose oxidase[37]. This interaction alters the pH, leading to a contraction of the hydrogel sphere and subsequent quenching of the surface carbon dots.

These applications underscore the adaptability of hydrogels in biosensing applications. Beyond biosensing, hydrogels also serve as an effective Extracellular Matrix (ECM) substitute in biological research[38], as illustrated in Fig.2.11d. Due to their high biocompatibility, hydrogels provide a suitable platform for cellular growth and proliferation. Furthermore, their adjustable 3D structures, the stiffness of which can be thoroughly controlled, offer an array of microenvironments for cellular growth. This feature opens up possibilities for studying cellular activity in a 3D scaffold rather than a traditional 2D platform. In addition, like other polymers, hydrogels possess elastic properties that make them significant in biophysics research. Their flexible chains lead to elasticity, enabling the calculation of applied force by monitoring the deformation of the hydrogel[39], as seen in Fig.2.11e. As such, hydrogels continue to offer new avenues of exploration in diverse fields.

2.8 Information Security and Anti-counterfeiting

Over the past decade, information security has seen an extraordinary expansion, spanning a vast array of applications integral to our daily lives, including health, economy, and intellectual property protection[38-41]. Concurrently, the advent of an increasingly digital and interconnected society has magnified the challenges posed by fraudulent activities, including the global menace of counterfeiting. This illicit practice

has substantial economic repercussions, amounting to billions of dollars, and presents significant risks across multiple sectors, from high-end commodities to medicinal products, thereby hindering economic growth and endangering public health and safety. Accordingly, the establishment of robust security systems with potent anti-counterfeiting capabilities has become paramount in safeguarding personal information, privacy, and broader socio-economic stability. Traditional anti-counterfeiting methods, primarily designed based on mathematical one-way functions[42, 43], carry a heightened risk of information leakage. Hence, in response to these emerging threats and in anticipation of future challenges, the demand for dependable, sophisticated, and effective anti-counterfeiting strategies has grown more pressing than ever.

2.8.1 Conventional Anti-counterfeiting Method

Anti-counterfeiting methods have been realized based on various materials not only just inorganic materials such as crystals but also reach to biomaterials such as protein. One example is using 2D materials to generate anti-counterfeiting patterns. Lin[44] reported a study (Fig.2.12a) presents an innovative, reliable, and environmentally stable anticounterfeiting technology, combining two-dimensional materials MXene and graphene oxide, deep learning software[43], and QR codes to provide enhanced information security.

Raman shift is also a very popular information carrier in developing anti-counterfeiting techniques. As shown in Fig.2.12b, this research[45] introduces biocompatible, flexible optical physical unclonable functions (PUFs) labels created by embedding microdiamonds in silk fibroin films. These labels, which can adhere to complex surfaces, provide enhanced counterfeit protection. The microdiamonds' random distribution and high stability ensure a robust PUF performance.

Besides inorganic materials, organics materials can also contribute to the realm of anti-counterfeiting. Healm[46] reported using chaotic phosphorescent patterns developed from an organic crystal and atomic seed heterostructure, security labels are created (Fig.2.12c). These patterns, while similar macroscopically, display

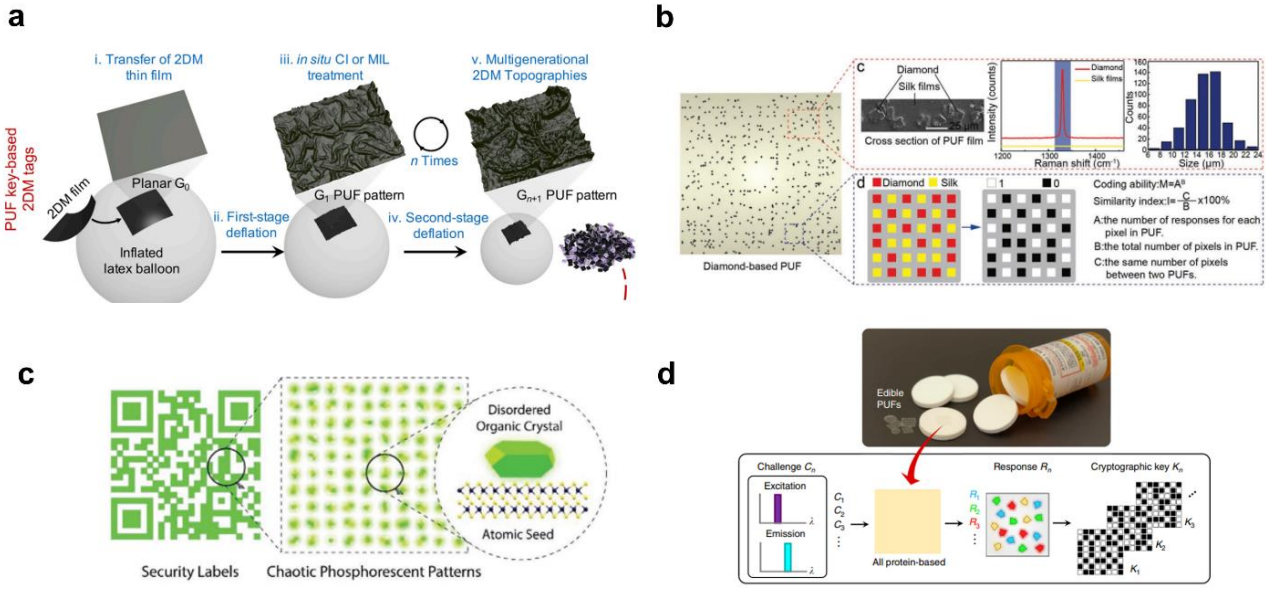

Figure 2.12 Schematics diagrams of anti-counterfeiting methods. **(a)** 2-dimensional material[43]. **(b)** Method using Raman shift as analyte[44]. **(c)** Organic crystal[45]. **(d)** Edible anti-counterfeiting labels based on protein[46].

significant disorder at the microscopic level, resulting in an encoding capacity exceeding 10^{17} on a small MoS2 fragment. Last but not least, anti-counterfeiting labels can even be fabricated by specific protein[47] which is edible and safe for human (Fig.2.12d). This study substantially enhances the feasibility of deploying anti-counterfeiting technologies in real-world applications, underscoring the immense potential of organic, bio-related materials within this domain.

2.8.2 Anti-Counterfeiting Methods Based on Stimulated Emission

In contrast to traditional technologies that rely on broad photoluminescence or Raman shift, laser emission (or stimulated emission) presents an innovative approach for optical encoding. It introduces new coding elements and produces intricate emission spectra corresponding to modifications in gain materials and cavity geometry. The variety of laser parameters, including thresholds, spectrum, laser modes, along with their sensitivity to multiple stimuli, position lasers as optimal candidates for generating substantial data volumes useful for creating anti-counterfeiting labels. Zhao[48]

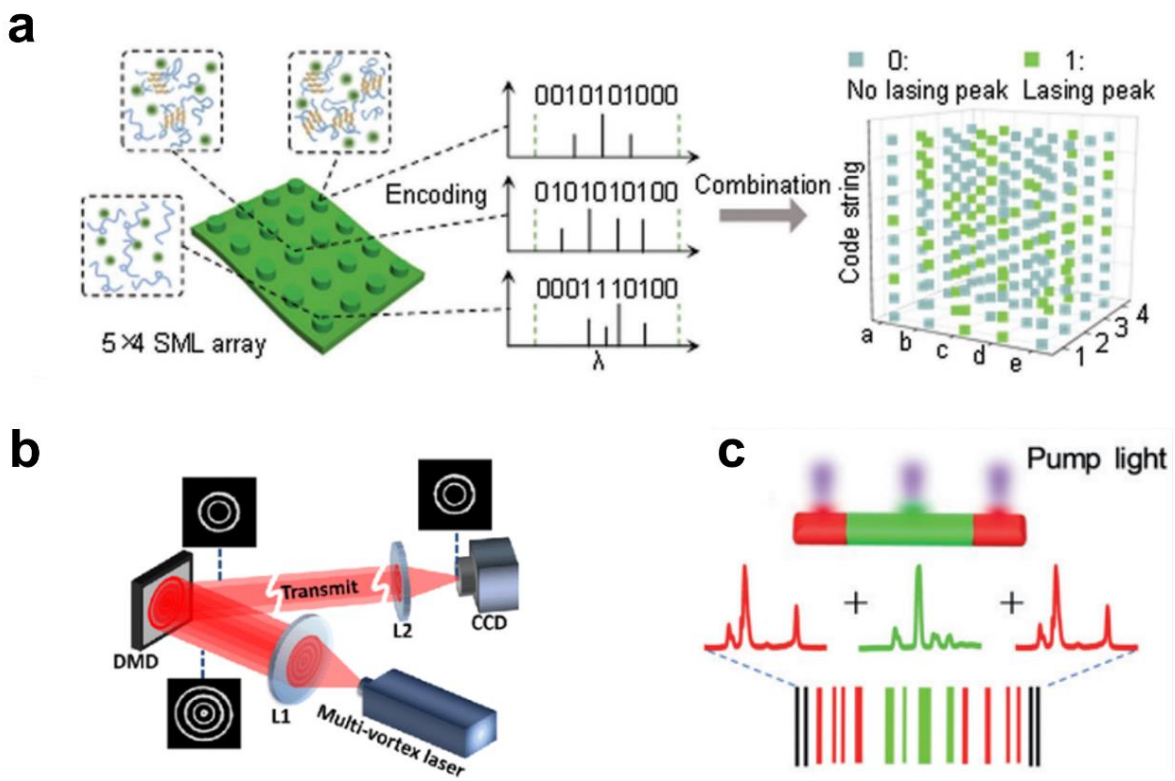

Figure 2.13 Schematic diagrams of anti-counterfeiting methods based on stimulated emission. **(a)** Based on laser intensity[47]. **(b)** Based on laser modes[48]. **(c)** Based on FWHM extracted from laser spectrum[49].

presented a unique anti-counterfeiting approach using silk protein-based microlaser arrays with physical unclonable functions, creating secure labels with predictable readout sites and unique signal distribution (Fig.2.13a). The coding elements 1 and 0 refer to occurrence or missing of lasing peak in corresponding wavelength. Besides spectrum, laser modes[2] can also serve as a potential candidate for anti-counterfeiting for its high sensitivity to external stimuli and cavity geometry (Fig.2.13b). As laser presents various parameters, Full wavelength half maxima (FWHM)[49] is also be utilized to transfer the laser spectrum into a readable 2-dimensional barcode (Fig.2.13c).

Chapter 3: Hydrogel Microlasers for Versatile Biomolecular Analysis based on Lasing Microarray

In this chapter, we will detail the development of a “hydrogel biological microlaser” by exploiting the high versatility of hydrogels and exploring its fundamental characteristics in lasing. The concept of hydrogel lasing microarray was also devised through inkjet printing, suggesting the potential as a novel sensing platform for biomolecular interactions.

Biological microlasers have advanced rapidly in recent years, demonstrating their immense potential to employ lasing emission as a sensing signal for monitoring molecular interactions[1, 4, 16, 50, 51]. Such lasers are known for their distinct advantages in terms of signal amplification, narrow linewidth, and strong intensity, which lead to unprecedented detection sensitivity of tiny changes in biological systems[5, 17, 22, 52, 53]. Most biological microlasers were realized through the introduction of fluorescent biomolecules (gain) into millimeter-sized resonators, resulting in difficulties for realizing further applications. As such, whispering gallery mode (WGM) microlasers have come into the play due to their high Q-factor, low-mode volume, and miniaturized size. A plethora of biomaterials has been employed to form biocompatible microlasers in recent years, including proteins, poly(lactic acid), starch, lipids, cellulose, and polymers[54-63]. To move a step forward, it is essential to realize microlasers with the versatility to design, control, and functionalize different biostructures and molecules within the cavity. Hydrogel, one of the most popular biomaterials, has received tremendous attention for its high versatility among biocompatible materials over decades[35, 64]. Endowed by its unique three-dimensional network structures and porous interface, hydrogel enjoys priority in a wide range of applications in drug delivery, therapeutics, tissue engineering, and biosensing devices[65-67]. Hydrogels can be used to encapsulate biomolecules or cells because they provide the natural aqueous environment required for biomolecules to function in biological systems. In particular, the degree of crosslinking can be tailored according

to specific functionalities, such as diffusion barrier, porous size, and interactions with the environment and other molecules. Considering their good mechanical strength and modifiable chemical interactions, the stiffness of hydrogels can also be designed for engineering in cellular mechanics[68, 69]. Hydrogel microarrays have also been implemented as a high-throughput platform for cellular and molecular screening[70, 71].

Inspired by the high versatility and controllability of hydrogels, this study aims to develop hydrogel microlasers and to explore its fundamental characteristics in biolasing. Fig.3.1a illustrates the concept of hydrogel biological microlaser, in which precursor solutions mixed with fluorescent dyes are printed on a highly reflective dielectric mirror to form a cap-like cavity. Whispering gallery mode laser emission was achieved through the optical confinement between the hydrogel droplet and the bottom mirror. Taking advantage of the unique physical properties of hydrogel, lasing behaviors could be fully manipulated by different degrees of polymerization and monomer ratios. The obtained laser signal was found to be closely related to the structural transformation in hydrogel cavities. Furthermore, hydrogel lasing microarray was developed through inkjet printing, contributing a novel platform to study molecular interactions within 3D hydrogel network structures. Fig.3.1b presents the photo and fluorescence image of a hydrogel microarray after UV curing. Various droplet sizes, volumes, and fluorophores could be fabricated by programming the inkjet printer, where the smallest laser diameter could be achieved was 20 μm.

To demonstrate potential applications and functionality of such a hydrogel laser array, FRET (Förster resonance energy transfer)-based detection was introduced in hydrogel by exploiting fluorescent-peptide conjugates. Molecular distances between FRET pairs could be adjusted by different polymerization degrees, resulting in different FRET lasing intensity. Single-mode laser emission was achieved with a significantly increased FRET lasing intensity, suggesting a sensitive platform for monitoring biomolecular interactions. Finally, to manifest the versatility of hydrogel microlasers, peptides with diverse molecular weights were encapsulated to form biolasing. Lasing

spectra and thresholds generated form fluorescent-peptides revealed the role of molecular size towards lasing performance. These results not only provide deep insights into the relationship between biostructure and lasing properties but mark a critical step towards employing hydrogel laser in high-throughput molecular analysis.

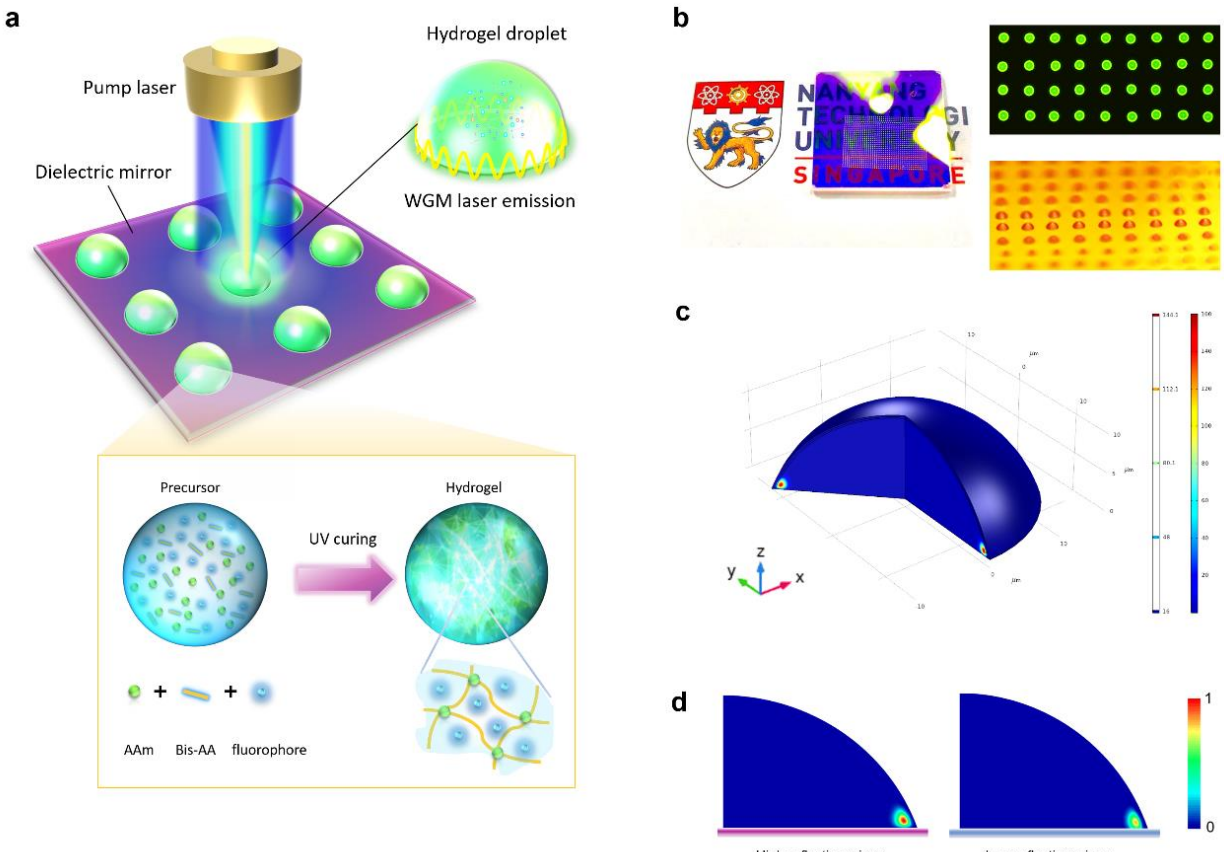

Figure 3.1 (a) Schematic diagram showing the concept of hydrogel biolasers and hydrogel lasing microarray, which is supported by whispering gallery mode. The bottom inset depicts a transformation of hydrogel inner structure after UV curing. Fluorophores confined inside the polymer network forms the gain medium of hydrogel laser. **(b)** The photograph of hydrogel microarray printed on a dielectric mirror. Right panel: fluorescent image of hydrogel array excited by LED pump (top). All the droplets in this image present diameter of 20 μm, which is the minimum size that can be achieved. An enlarged microscopic image of hydrogel array (bottom). **(c)** Simulated 3D electric field distribution of a WGM droplet resonator placed on the mirror (diameter of 20 μm). **(d)** Comparison of the WGM modes when a microdroplet is placed on a high-reflective mirror (Q-factor= $6x10^4$) and a low-reflective mirror (Q-factor= $2.0x10^2$).

3.1 Theoretical Background

3.1.1 Rate Equation

The influence of a mirror on the single-mode laser operation was examined through theoretical simulation using the COMSOL Multiphysics software. The Quality factor (Q-factor) for the hydrogel cavity, both with and without a Distributed Bragg Reflector (DBR), which is a highly reflective structure, were computed and the results are presented in Fig.3.1d. To attain lasing, it's crucial to overcome all radiative losses induced by both the cavity and the gain materials. A threshold Q-factor can be deduced using the rate equations. The population dynamics of Rhodamine B, which serves as a laser gain medium, can be delineated by the subsequent equations:

$$\frac{dn(t)}{dt} = I_p \sigma_{op} \left[N_0 - n(t)\right] - \frac{\sigma_{el} c}{\eta} n(t) q(t) + \frac{\sigma_{ol} c}{\eta} \left[N_0 - n(t)\right] q(t) - \frac{n(t)}{\tau_f} \tag{3.1}$$

$$\frac{dq(t)}{dt} = \frac{Fc}{\eta V} \sigma_{el} n(t) + \frac{\sigma_{el} c}{\eta} n(t) q(t) - \frac{\sigma_{al} c}{\eta} \left[N_0 - n(t)\right] q(t) - \frac{q(t)}{\tau_q} \tag{3.2}$$

By solving the equations, the threshold Q-factor of 70000 can be obtained, where we assume photon density of the emission light is 1.17×10^{23} cm^{-3}.

3.1.2 Threshold Calculation

To calculate the thresholds under different photoinitiator concentration, we utilize rate equation to describe the population dynamics of FRET dye pairs (Fluorescein isothiocyanate (FITC) and Rhodamine-B(RhB)) which can be read as:

$$\begin{aligned} \frac{dq_d(t)}{dt} &= \frac{Fc}{\eta V} \sigma_{edd} n_d(t) + \frac{c q_d(t)}{\eta} \left\{ \sigma_{edd} n_d(t) - \sigma_{odd} \left[N_d - n_d(t)\right] \right\} \\ &- \frac{c q_d(t)}{\eta} \sigma_{aad} \left[N_a - n_a(t)\right] - \frac{q_d(t)}{\tau_{cd}} \end{aligned} \tag{3.3}$$

$$\begin{aligned} \frac{dn_a(t)}{dt} &= I_p \sigma_{pa} \left[N_a - n_a(t)\right] + k_F n_d(t) + \frac{c q_d(t)}{\eta} \sigma_{aad} \left[N_a - n_a(t)\right] \\ &- \frac{c q_a(t)}{\eta} \left\{ \sigma_{eaa} n_a(t) - \sigma_{aaa} \left[N_a - n_a(t)\right] \right\} - \frac{n_a(t)}{\tau_a} \end{aligned} \tag{3.4}$$

$$\frac{dq_a(t)}{dt} = \frac{Fc}{\eta V}\sigma_{eaa} n_a(t) + \frac{cq_a(t)}{\eta}\left\{\sigma_{eaa} n_a(t) - \sigma_{aaa}\left[N_a - n_a(t)\right]\right\} - \frac{q_a(t)}{\tau_{ca}} \tag{3.5}$$

$$\frac{dn_d(t)}{d_t} = I_p \sigma_{pd}\left[N_d - n_d(t)\right] - k_F n_d(t) - \frac{cq_d(t)}{\eta}\left\{\sigma_{odd} n_d(t) - \sigma_{odd}\left[N_d - n_d(t)\right]\right\} - \frac{n_d(t)}{\tau_d} \tag{3.6}$$

The calculation results for theoretical lasing threshold under different FRET efficiencies is shown in Fig.3.4a.

3.2 Experimental Methods

3.2.1 Materials

The dyes we used in this work are as follows: Fluorescein sodium salt (Sigma-Aldrich #F6377), Rhodamine B (Tokyo Chemical #A5102), 5(6)-Carboxyfluorescein N-hydroxysuccinimide ester (Sigma-Aldrich #21878), NHS-Rhodamine (Thermal Fisher Scientific #46406). For the hydrogel, Acrylamide (Sigma Aldrich #A9099) was selected as the monomer. N,N′-Methylenebis(acrylamide) (Sigma #146072) as crosslinker to form 3D structure, and 2-Hydroxy-4′-(2-hydroxyethoxy)-2-methylpropiophenone (Sigma # 410896) as photoinitiator to trigger polymerization. To prepare dye-peptide conjugates, Gly-His (Sigma Aldrich #G1627), L-Glutathione oxidized (Sigma Aldrich #G4376), V5 peptide (Sigma Aldrich #V7754), insulin (Sigma Aldrich #I6634), and protein standard (BSA, 200mg/ml) (Supelco #P5369) were used as bioagents to combine with NHS ester.

3.2.2 Array Fabrication

For water-based array, 0.8 mg FITC was added into 1mL mixture of water and glycerol (volume ratio 1:1) and then mixed on the vortex. Final dye concentration is 2 mM. Then the solution was added into the printer and printed on a dielectric mirror. For hydrogel based array, 0.475 g Acrylamide (AAm) and 0.025 g N,N′-Methylenebis(acrylamide) (Bis-AA) were dissolved in 500 μL DI water to prepare precursor solution. Futhermore, 35 mg photoinitiator was added into the solution to

trigger polymerization after UV curing (Panasonic #ANUJ3500). Then 0.8 mg FITC/ 1 mg RhB was added into the precursor. The final dye concentration is 2 mM. The prepared precursor was added into the printer and printed on a dielectric mirror (customized by Evaporation Coatings Inc, USA). At last, the printed array was illuminated by a UV curing system (375 nm) for 5 seconds.

3.2.3 FRET Pairs Preparation

For FITC-RhB pairs, 0.8 mg FITC and 1 mg RhB were added into the precursor solution and then mixed on the vortex. Final concentrations of FITC and RhB were both 2 mM.

For FITC-Gly-His conjugates, 1mg FITC-NHS was first dissolved in 25 μL DMF. 0.6 mg Gly-His was dissolved in 200 μL Triethylammonium bicarbonate buffer (Sigma Aldrich #T7408). Then two solutions were mixed and reacted under room temperature for 2 h. For RhB-GSH conjugates, 1.1 mg RhB-NHS was dissolved in 25 μL DMF. 1.3 mg of GSH was dissolved in 200 μL PBS buffer. Then two solutions were mixed and reacted under room temperature for 2 h. After the reaction, the prepared conjugates were mixed, and 100 μL ethanol was added into the solution. The final concentration of dyes was 2 mM, and the peptides were prepared excessively to ensure all fluorophores have been conjugated with peptides. Then 0.475 g AAm and 0.025 g Bis-AA were added and dissolved through vortex mixing. Finally, different amount of photoinitiator were added into the prepared solution, ranging from 0 mg to 45 mg.

3.2.4 Preparation of Dye-peptide Conjugates

First, 1.6 mg RhB-NHS was dissolved in 50 μL DMF. Then 1.3 mg GSH, 1.5 mg V5-peptide, 5 mg insulin were dissolved in 350 μL PBS buffer, separately. Later, RhB-NHS solution was added into each group and reacted with bioagents under room temperature for 2 h. The RhB-NHS solution was also added into 350 μL PBS buffer as a comparison group. After reaction, 0.475 g AAm, 0.025 g Bis-AA and 35 mg photoinitiator were added into the prepared solution and dissolved on the vortex. Finally, 100 μL ethanol was added to the solution. The Final concentration of RhB in

every group was 2 mM and all the concentration of peptides were prepared excessively to ensure RhB-NHS to be totally conjugated.

3.2.5 Optical System Setup

A microscopic system (Nikon Ni2) with a 10X 0.3 NA objective was used to pump the hydrogel array and collect light. Optical pumping was achieved by a pulsed ns-laser (EKSPLA PS8001DR) integrated with an optical parametric oscillator with (repetition rate: 50 Hz; pulse duration: 5 ns; pulse energy: 5mJ). According to the respective absorption wavelength of fluorophores, the pump laser was tuned to 488 nm for FITC and FRET or 532 nm for RhB. The beam diameter at the objective focal plane was approximately 40 μm. The collected light was transmitted to a charge-coupled device camera or an imaging spectrometer (Andor Kymera 328i and Newton 970 EMCCD). For quantitative measurements of fluorescence image, an integrated LED was used as the excitation source and imaged by a CCD (Andor Zyla SCMOS) mounted on the microscope. A filter whose transmissivity from 460-480 nm was used to obtain desired excitation for FITC and a filter whose transmissvity from 510-530 nm was used for obtain desired excitation for RhB. The reflectivity file of the DBR mirror we used was shown in Fig.3.2.

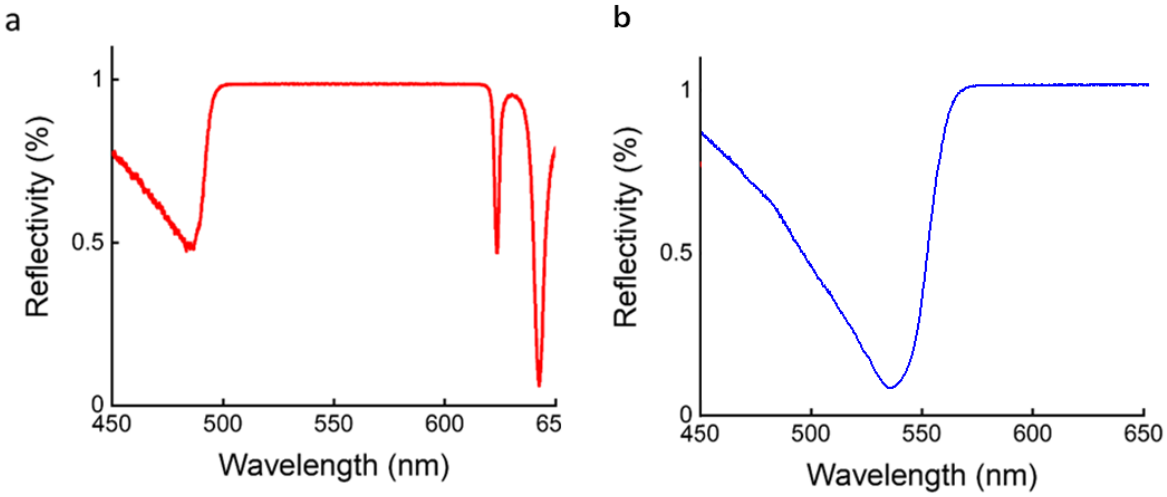

Figure 3.2 Reflectivity file of the DBR mirror used in experiment for **(a)** FITC and **(b)** RhB, which has high reflectivity (R >99%) in corresponding to each gain's emission to achieve support for lasing generation.

3.3 Results and Discussion

3.3.1 Investigation of Lasing Behaviors In Hydrogel Array

In order to explore the possibility of obtaining lasing with a water-based microcavity, the lasing modes of a hydrogel droplet resonator were first simulated based on a 20 μm sized hydrogel droplet. Fig.3.1c presents the typical WGM, which resonates around the bottom of a droplet. To understand the mechanism of the mirror underneath, we compared the Q-factors and electric field strengths of WGMs under high and low reflectivity mirrors in Fig.3.1d. Under a high reflectivity mirror (R = 99.9%), WGM possesses a reasonably high Q-factor of 10^4 and strong electric field strength as indicated in Fig.3.1d, compared to a WGM modes on a low reflective substrate. When the bottom mirror has the same resonant wavelength as the gain in a droplet, the overall threshold becomes lower due to high Q-factor; therefore, it can support and generate more laser modes and higher intensity are expected. On the contrary, the Q-factor becomes two orders of magnitude lower when the bottom substrate possesses a low reflectivity substrate (R = 11.1%), resulting in lower electric field strength and lower number of laser modes. Herein, the tremendous difference in Q-factor illustrates the critical role of the bottom mirror for achieving lasing conditions in a hydrogel droplet resonator.

As a first step, hemisphere microdroplets were printed on a highly-reflective dielectric mirror by using water/glycerol (volume ratio 1:1) to form the cavity and Fluorescein-isothiocyanate (FITC) as the gain material. In comparison to previous works who used high-precision dispensers to fabricate microlasers[72, 73], it is noteworthy that here we only modified an office inkjet printer to achieve microlaser arrays. WGM laser emissions were obtained and verified by free spectral range corresponding to the droplet diameter. Taking advantage of the versatility of inkjet printer, lasing wavelength could be adjusted by changing different fluorophores. For instance, lasing from Rhodamine-B (RhB) was observed around 610 nm with a threshold of 3.6 μJ/mm^2. Different droplet microlaser diameter or contact angle could also be adjusted by programming the printer.

Moving forward, we attempt to implement the same approach to achieve hydrogel lasers. By replacing glycerol with acrylamide monomer and crosslinkers, hydrogel precursors mixed with FITC or RhB were printed on the same mirror. Laser emissions from hydrogels were observed, as shown in Figs.3.3a and 3.3b, respectively. The free spectral range corresponds well with the hydrogel droplet diameter, following the basic principle of WGM. It is noteworthy that no 3D network structure was formed inside the cavity before polymerization. However, complex 3D networks are formed after the polymerization reaction. To investigate how such 3D network structure will make an impact on lasing behavior, we compared the lasing performance by adjusting the monomer/water ratio from 10% to 50 % under a fixed pump intensity in Fig.3.3c. To our surprise, the lasing intensity increased significantly with the increment of monomer ratios (Figs.3.3d and 3.3e). This interesting result shows that the lasing behavior of hydrogels is highly dependent on the inner structure of hydrogels, which can be attributed to the difference in terms of refractive indexes. The higher the monomer ratio, the higher the refractive index will lead to higher Q-factor and thus lasing intensity.

On the other hand, we investigated how polymerization (degree of crosslinking) may affect lasing behavior, based on a fixed content (monomer/water ratio). The differences can also be clearly seen in laser modes, before and after polymerization in Fig.3.3f. Apparently, ring modes were formed inside the hydrogel after polymerization (bottom photo). Higher-order modes were observed as well, which is likely the result of 3D network structure formed inside the hydrogel. Furthermore, we measured the lasing threshold of precursor and polymerized hydrogel. The lasing spectra of hydrogel under various pump energy densities are plotted in Fig.3.3g. Fig.3.3h shows the spectrally integrated laser output as a function of pump energy density (610 nm- 630 nm) extracted from Fig.3.3g. A lower lasing threshold was found for polymerized hydrogel due to the result of a slightly increased refractive index. However, the increased value of RI (0.02) was not very obvious; thus didn’t become a dominated factor, which is consistent with the previous report[74].

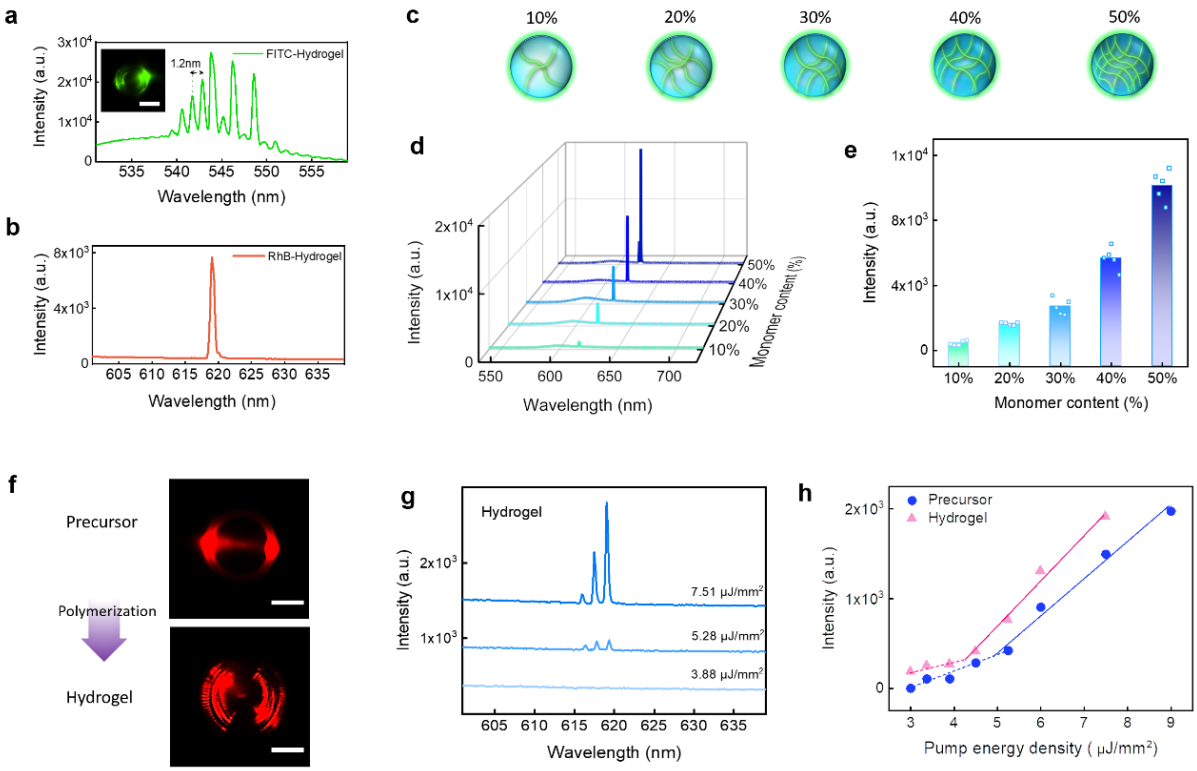

Figure 3.3 (a-b) Lasing spectra obtained from hydrogel microlaser by mixing precursor with (a) 2 mM FITC and (b) 2 mM RhB, respectively. The inset shows the laser mode image from one hydrogel droplet under 480 nm excitation. The excitation wavelength for FITC was 480 nm and RhB was 530 nm. **(c)** The schematic diagram shows the difference of inner hydrogel structure with different monomer/water ratio (%) in the precursor. **(d)** Lasing spectra obtained from hydrogel droplet with different monomer content ratio and same diameter of 60 μm. The encapsulated RhB concentration was 2 mM. Pump energy density = 57 μJ/mm^2 for all collected spectra. **(e)** The lasing intensity distribution extracted from (d). **(f)** Comparison of laser mode obtained from precursor and hydrogel (before and after polymerization). **(g)** Lasing spectra of hydrogel containing 2 mM RhB under different pump energy density, the curves have been shifted for clarity. **(h)** Comparison of lasing threshold between precursor and polymerized hydrogel. All scale bars, 30 μm. UV curing time was fixed at 5 seconds.

3.3.2 Hydrogel Lasing Controlled by Molecular Interactions

On the basis of hydrogel laser, we aim to investigate how such microlasers could be applied in biomolecular analysis. Herein we introduced FRET pairs in hydrogels to demonstrate how FRET lasing efficiency can be modulated by tuning the Forster distance in hydrogel microdroplets (Fig.3.4a). By changing the amount of photoinitiator,

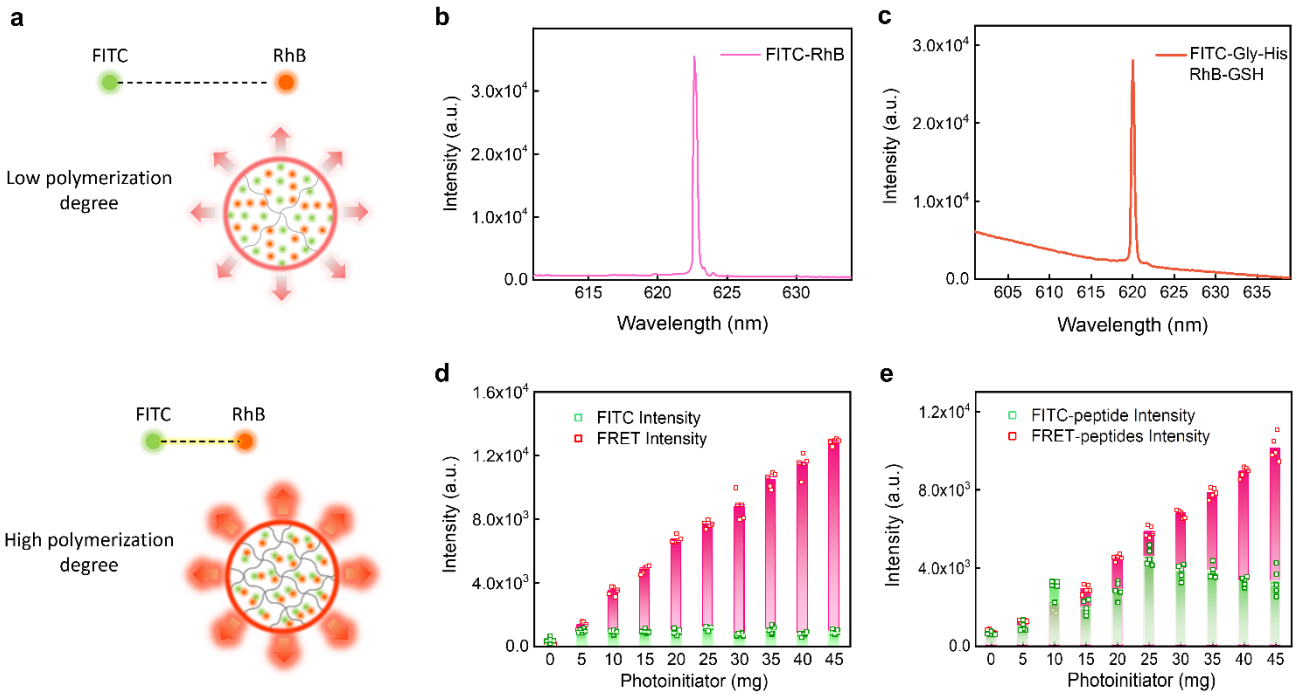

Figure 3.4 (a) Schematic diagram illustrating FRET interaction in hydrogel microdroplet with low polymerization degree and high polymerization degree. FRET formed by 2 mM RhB and 2 mM FITC. The Foster distances become smaller at a higher polymerization degree. **(b-c)** Lasing spectra obtained from hydrogel containing (b) 2 mM FITC-RhB FRET pairs and (c) 2 mM FITC-Gly-His/RhB-GSH pairs. **(d)** Comparison between the integrated intensity of laser output obtained from hydrogel containing pure FITC and FRET pairs, under various photoinitiator concentrations. (**e**) Comparison between the integrated intensity of laser output obtained from FITC-Gly-His and FRET-peptide pairs, under various photoinitiator concentrations. UV curing time was fixed at 5 seconds. All droplet diameter was 60 μm. Pump energy density = 75 μJ/mm^2. Excitation wavelength = 480 nm.

the polymerization degree will influence the FRET lasing performance. Fig.3.4b first presented the lasing spectrum of FRET laser resulted from pure FITC-RhB. In order to monitor the interaction between molecules, two peptides, including Gly-His and L-Glutathione oxidized (GSH), were selected to conjugate with FITC N-hydroxysuccinimide ester (FITC-NHS) and Rhodamine N-hydroxysuccinimide ester (RhB-NHS) respectively. Fig.3.4c shows the lasing spectrum obtained from hydrogel containing FITC-Gly-His and RhB-GSH dye-peptide conjugates, where FRET-peptide lasing was achieved. To our surprise, the FRET emission signals received were nearly single-mode rather than multi-mode lasing. We further explored the cause of this interesting phenomenon using theoretical calculation and provided explanation:

Different Q-factors of hydrogel cavity resulted from different reflectivity of the bottom mirror substrate.

This point can be explained by the effective Q-factor of hydrogel cavity at respective wavelengths, depending on the reflectivity of the bottom mirror. Fig.3.5 shows the calculated Q-factor of hydrogel cavity with a low reflective mirror and high reflective mirror (R = 99.9%) from 615 nm to 630 nm. Due to the mirror's low reflectivity (R =40%) around RhB emission wavelength, the radiative Q-factor was constricted and decreased compared to that with a high reflective mirror. Nonetheless, according to calculation results, only the Q-factor of WGM mode at 620 nm was still higher than the threshold Q-factor, thus enabling it to compensate for the losses, forming a sharp single-mode on the spectrum

With a fixed control of molecule concentrations and UV-curing time, the increased amount of photoinitiator will lead to a higher degree of polymerization. FRET pairs would be squeezed by smaller interval of hydrogel chains than those with lower polymerization degree, resulting in higher energy transfer efficiency (Fig.3.4a).

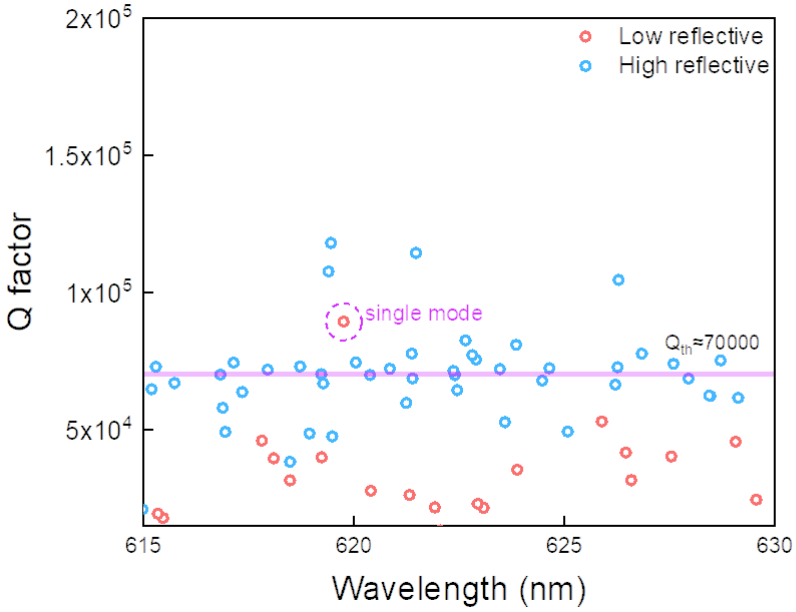

Figure 3.5 Calculated Q-factor of hydrogel cavity with low reflective mirror (red spots) and high reflective mirror (blue spots) from 615 nm to 630 nm.

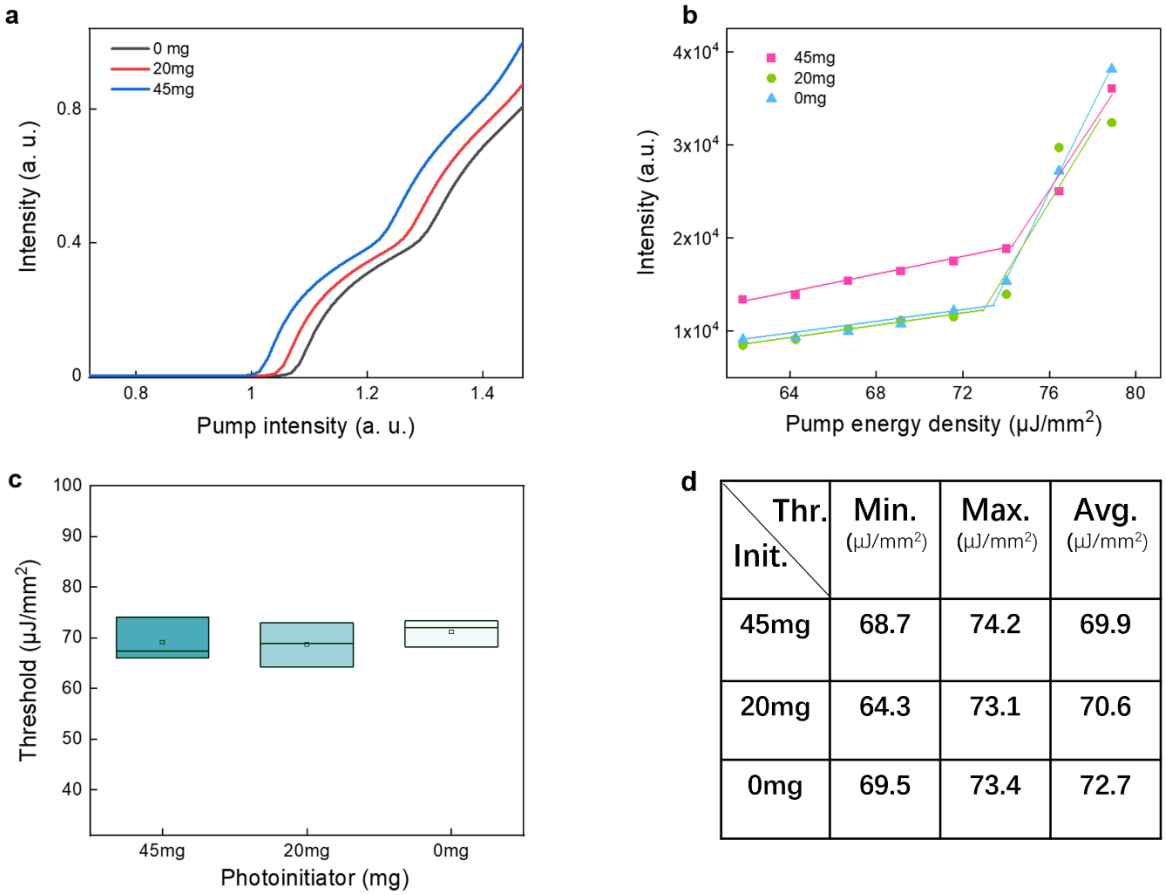

d

Thr. / Init.	Min. (μJ/mm²)	Max. (μJ/mm²)	Avg. (μJ/mm²)
45mg	68.7	74.2	69.9
20mg	64.3	73.1	70.6
0mg	69.5	73.4	72.7

Figure 3.6 (a) Comparison of calculated FRET lasing threshold between hydrogel cavity containing 0, 20 and 45 mg photoinitiator. **(b)** Experiment results of FRET lasing threshold from hydrogel cavity containing 0, 20, 45 mg photoinitiator. **(c)** Statistical plot of FRET lasing thresholds obtained from hydrogel cavity contained above mentioned photoinitiator concentration. **(d)** The minimum, maximum and average value of threshold recorded in (c).

Consequently, the distance between the donor molecules and acceptor molecules could be adjusted by a polymerization degree (crosslinking degree).

We first chose three photoinitiator concentrations (0, 20, and 45 mg) as a comparison to study how polymerization degree may influence the FRET lasing performance. Fig.3.6b shows the lasing threshold curves for FRET lasing with different photoinitiator concentration. Only a slight difference could be distinguished, indicating the change of Forster distance couldn't be entirely reflected by lasing thresholds. Theoretical calculations were also performed by considering respective FRET efficiency and Föster distances (Fig.3.6a), which were in good agreement with experiment results. However, the calculation results suggested a significant trend in

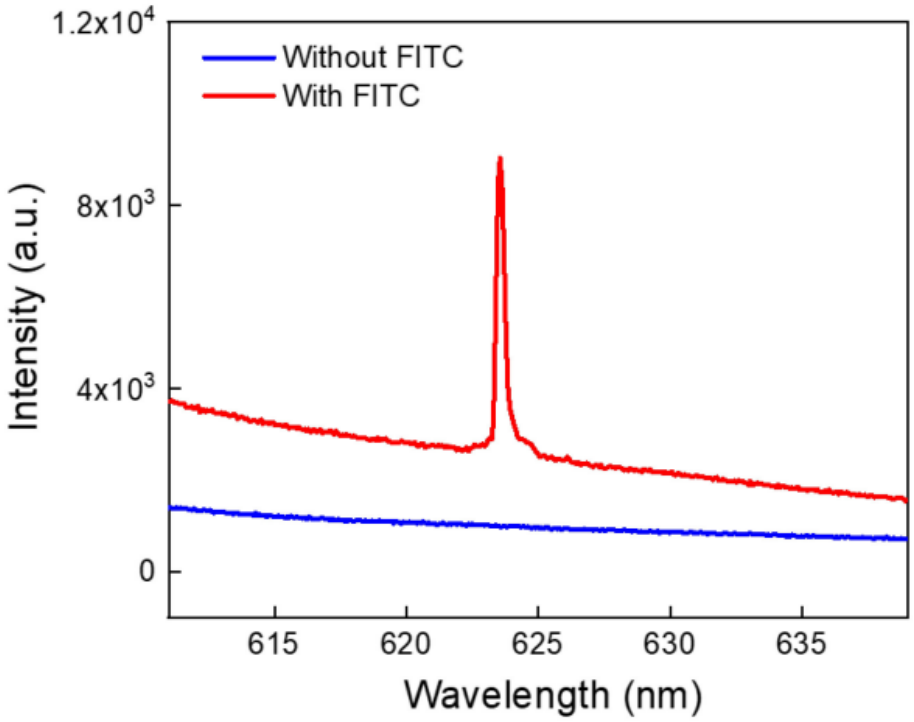

Figure 3.7 Red curve: FRET lasing spectrum in hydrogel droplet (FITC-RhB). Blue curve: direct excitation of RhB in hydrogel droplet without FITC (donor). Both were excited under pump energy density of 100 μJ/mm^2.

terms of lasing intensity near the threshold, which may be an alternative parameter to quantify FRET interactions. To ensure the differences between thresholds is indeed small, a statistic for experimental obtained thresholds value of three different FRET efficiencies is plotted in Fig.3.6c and Fig.3.6d.

Herein we employed lasing intensity in Figs.3.4d and 3.4e to present the controllability of molecular interactions and lasing action by adjusting the photoinitiator concentration in hydrogels. The pump energy density was selected based on the threshold of 0 mg lasing threshold. We first tested hydrogel lasers with FITC-RhB fluorophores in Fig.3.4d. Under a fixed UV-curing time, the integrated FRET laser intensity increased linearly, reflecting a higher FRET efficiency (pink bars). Similar results were obtained by using FRET peptide pairs (FITC-*Gly-His* & RhB-*GSH*) in Fig.3.4e (pink bars). As a control group, the lasing intensity of hydrogel lasers without FRET pairs (only FITC or FITC-*Gly-His*) are manifested in Figs.3.4d and 3.4e, respectively (green bars). Fig.3.4d shows that lasing intensity only increased between

0 mg to 5 mg, while the intensity remains beyond 5 mg. In Fig.3.4e, the lasing intensity increased between 0 mg to 25 mg and started to drop gradually. In contrast, the FRET-peptide laser intensity (pink bars) increased significantly when the photoinitiator reached above 25 mg. To confirm the increase of FRET laser intensity is attributed to increased FRET efficiency, the corresponding lasing spectra are provided in Fig. 3.7.

3.3.3 Hydrogel Lasing with Different Biomolecules

Finally, our test target was to demonstrate the wide applicability of hydrogel lasing microarray. For this purpose, different types of biomolecules were selected based on molecular weights. Fig.3.8a shows the schematic diagram of the three biomolecules conjugated to RhB-NHS, including insulin (5734 g/mol), V5-peptide (1524 g/mol), and GSH (612 g/mol). As a control group, RhB-NHS was plotted and analyzed. All four fluorophore conjugates were mixed with hydrogel monomers and printed to from lasing microarrays. Figs.3.8b to 3.8e show our obtained results, namely the respective lasing spectra obtained from hydrogel array with RhB-insulin, RhB-V5, RhB-GSH, and pure RhB-NHS, respectively. Besides lasing spectrum, Fig.3.8f shows the spectrally integrated laser output in the wavelength range 610-630 nm as a function of the pump energy density (610 nm- 630 nm). Our results in Fig.3.6f found that when RhB-NHS binds to biomolecules, the lasing threshold tends to become smaller. Given that there seems to be a trend between lasing threshold and encapsulated molecular size, many factors should be considered. Here we provided two possible explanations. First, the introduction of larger molecules increased the Rayleigh scattering in the whole system. Studies have reported that scattering can serve as a decisive factor for enhanced lasing in WGM cavity[75].

With more substantial scattering, the light path inside the cavity will be longer, which in turn increases the photon lifetime inside the cavity. The mentioned three molecules could have a similar effect inside hydrogel cavity, resulting in a lower lasing threshold. To be more specific, we calculated the corresponding fraction of scattered light. With Rayleigh scattering cross-section and corresponding molecular number, the fraction of light scattered by respective molecule was 2×10^{-2} for insulin, 10^{-2} for V5,

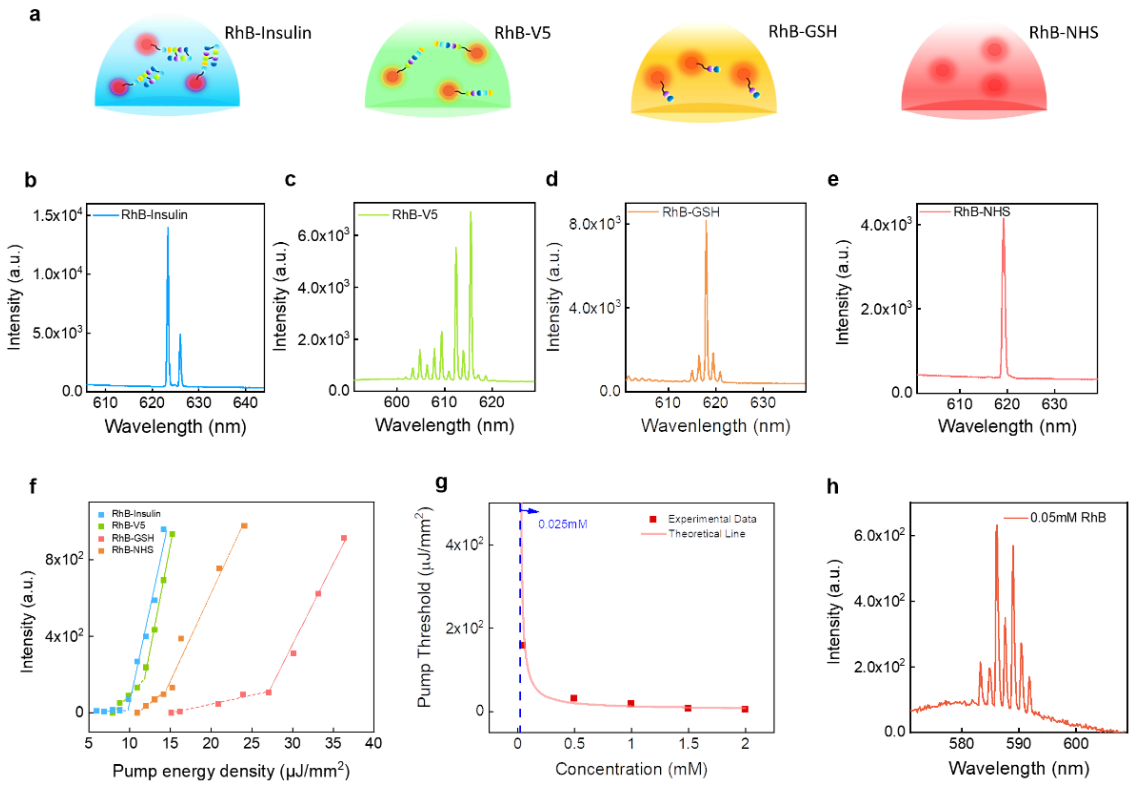

Figure 3.8 **(a)** Schematic diagram of biological molecules encapsulated by hydrogel droplets where RhB was used for fluorophore conjugation. **(b-e)** Lasing spectra obtained from hydrogel containing (b) RhB-insulin (5734 g/mol); (c) RhB-V5(1524 g/mol); (d) RhB-GSH (612 g/mol); (e) RhB-NHS above their respective lasing thresholds. The excitation wavelength for all the droplets were fixed at 530 nm. **(f)** Spectrally Integrated laser output obtained from hydrogel containing different RhB-peptide conjugates as a function of pump energy density. **(g)** Lasing threshold for hydrogel (droplet size of 60 μm) encapsulated with different RhB concentration. The lowest presented concentration here is 0.05 mM. The solid dots represent experimental data, and the pink curve represents the theoretical fitting. **(h)** Lasing spectrum obtained from hydrogel containing 0.05 mM RhB fluorophore.

and 1.8×10^{-3} for GSH; therefore larger molecules may generate stronger lasing emissions.

Second, larger molecules have more tendency to adhere to the interface[76], particularly the interface between the mirror and droplet. Consequently, more gain will contribute to the WGM lasing, thus generating a lower lasing threshold.

Finally, we explored the detection limit of hydrogel microlasers in Fig.3.8g. The concentration of RhB was adjusted in the hydrogel array to study the threshold

required for lasing.The square in represent lasing threshold measured from experiment. The lowest concentration in our experiment to obtain a stable lasing signal in hydrogel was approximately 50 μM (Fig.3.8h), which is an acceptable range for biomolecular analysis[1]. We also used rate equations to better illustrate the relations between the lasing threshold and RhB concentration, the numerical solutions are shown by the pink curve in Fig.3.8g. The blue dashed line, which is an asymptote to the curve, indicates the theoretical limit, which is possible to achieve in the current system. Herein the expected detection limit for lasing is close to 25 μM, implying that for biomolecule or agent on this order is possible to be detected through lasing.

3.3.4 Conclusion

In this study, we developed a fully functional, controllable, and biocompatible microlaser by using hydrogels. The realization of hydrogel laser marks a critical step for employing hydrogel laser in a wide range of biomedical applications. As such, various biomolecules and fluorophores could be encapsulated within the hydrogel to form lasing at desirable wavelengths. Fundamental lasing properties of hydrogel lasers were explored under different water-monomer ratios and degrees of polymerization. Our results revealed that the internal 3D hydrogel networks and biological structures would have a significant impact on its lasing output, including thresholds and spectra. Additionally, hydrogel lasing microarray was demonstrated by inkjet printing. To the best of our knowledge, this is the first microlaser array that can be easily fabricated on-chip by an office printer. Finally, single-mode FRET lasing was manipulated through biomolecular interactions, paving a new way for high throughput biomedical analysis.

Chapter 4: Imaging-based Optofluidic Biological Microlaser Array Encapsulated with Dynamic Living Organisms

In chapter 3, we detail the demonstration of biological microlaser arrays for molecular sensing. Here we wanted to move forward and investigated the possibility of using such method for the study of living organism applications. In this chapter, an inkjet-printed biological microlaser microarray encapsulated with living organism was developed for bioanalysis. For the first time, bioanalysis based on laser emission images was used to quantify underlying biochemical and biological processes in *vitro/in vivo* in a live organism. The detection limit was as low as single *E. coli* level. Combined with the intrinsically high sensitivity of micro-lasers, *E. coli* was exploited for dynamic lasing analysis under antibiotic drug interactions. The findings demonstrate that laser-image based analysis outperforms conventional fluorescence-image based analysis by two orders of magnitude. The same approach could be applied to a wide range of living species, including living cells, bacteria, viruses, and proteins interactions.

Optofluidics, which takes advantage of optics and microfluidics, has emerged as a building block in numerous fields over the past decade.[77-81] The ability to deliver light and fluids with microscopic precision has opened new applications in sensing and imaging[1, 11, 82-85]. For instance, flow cytometry, interferometry, and Raman spectroscopy based on optofluidics have already demonstrated their applicability in molecular and cellular analysis.[86-88] Recent progress in optofluidics has developed unique adaptability and regeneration of functional photonic systems[89, 90], such as energy devices, reconfigurable microphotonic devices, and optofluidics laser.[91-94] In particular, optofluidic biological microlasers have demonstrated several advantages over fluorescence in terms of signal amplification, narrow linewidth, and strong intensity, leading to orders of magnitude increase in detection sensitivity. Recently, a plethora of studies have shown the promise of biological microlaser from proteins, DNA, cells to living organisms[1, 11, 17, 18, 60, 95-99]. Endowed by the unique

properties of laser, optofluidic biological microlasers possess high sensitivity to subtle changes inside a cavity, including gain (dye) distribution and cavity structure. Various types of optical cavities and platforms have therefore been developed for bioanalysis[1, 12, 18]. However, most biological microlasers demonstrated to date require precise and accurate recording of the lasing spectrum, which limits its application in high-throughput biomedical applications and on-chip analysis. To move a step forward, it is essential to realize biological microlaser with the capability of rapid and large area data recording.

In contrast to lasing spectra, laser emission images offers a new dimension of information which is challenging to acquire from lasing spectrum. By taking advantage of the scanning technique, laser emission images or laser modes could be captured with a camera to form large-scale images. The accuracy of laser emission images has also been proven to be the same as spectrum-based laser-sensing measurements, indicating the applicability of laser imaging-based analysis[100]. With the integration of microarray[101-103], laser images could be obtained from different samples simultaneously[72, 104-107], Despite the recent progress in laser emission imaging, quantitative analysis of laser emission images remains unresolved[4].

In this study, we aim to develop an image-based lasing microarray that can be used for high-throughput and dynamic analysis of living organisms. Fig.4.1a illustrates the concept of such microarray, where whispering gallery mode (WGM) lasing was achieved through optical confinement along the equator of the microdroplet. By utilizing an office inkjet printer, *E. coli* (Escherichia coli) was encapsulated inside a microdroplet cavity formed by cell medium and glycerol. SYTO BC green fluorescent nucleic acid stain (Syto-BC) was used to label the nucleic acid components in *E. coli*. (laser gain). The minimal quantity of *E. coli* required for lasing was investigated to elucidate the limitation of such a laser microarray (~ single *E. coli* level). To achieve lasing analysis, WGM-based laser emission images of *E. coli* microarray were recorded when pumped above the lasing threshold. By converting the original RGB color model (RGB) image to greyscale, the former 2D image could be converted to a

statistical result of total pixel intensity for quantitative analysis.

To demonstrate the promising potential of image-based lasing analysis (Fig.4.1b), antibiotic drugs were added in the microdroplets to interact with *E. coli*. As a proof-of-concept, ampicillin was applied in the microarray to change the living condition and growth activity of *E. coli* by destroying their cell membranes. Both conventional fluorescence images and laser emission images were compared under different periods of reaction time based on pixel intensity. Our results which are detailed in subsequent sections of this chapter will show that lasing image-based analysis outperforms fluorescence image-based analysis by two orders of magnitude. The findings in this study indicate that lasing images could serve as a novel platform to quantify dynamic changes in living organisms with outstanding sensitivity. Besides the above-mentioned application, the similar concept can be integrated with other types of fluidics and nanoparticles to expand their functions[108-112]. We envision this tool can be exploited in a wide range of living species, including viruses, bacteria, and living cells, paving the way for high throughput on-chip analysis of bio-laser emissions.

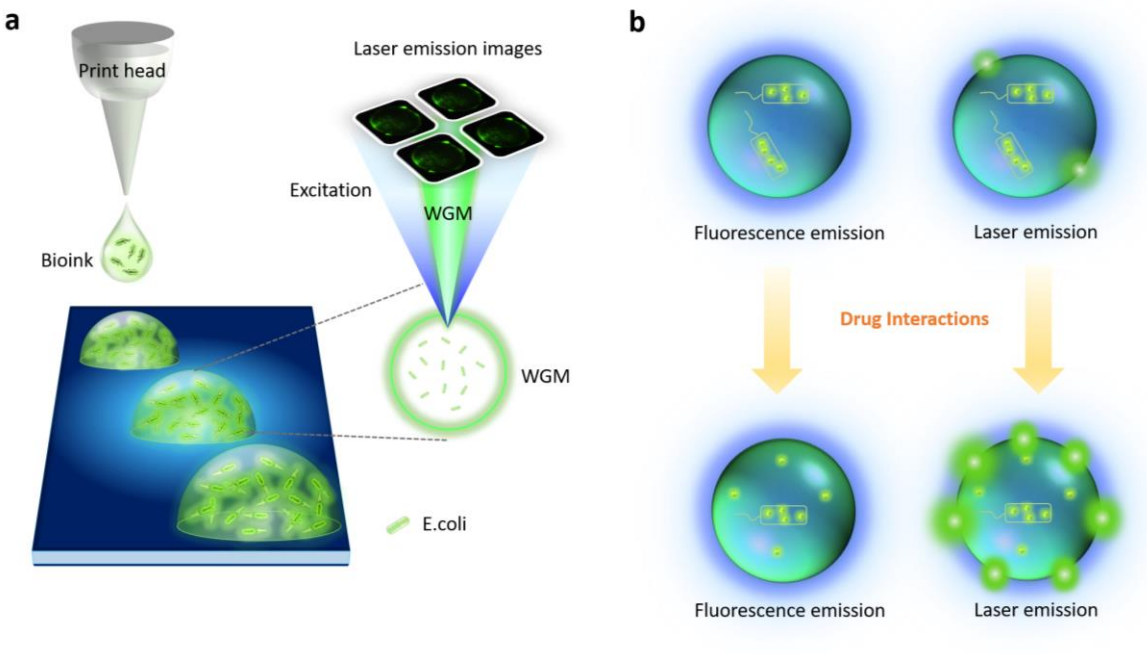

Figure 4.1 (a) Schematic showing the concept of image-based *E. coli* biological microlaser microarray. **(b)** Comparison between fluorescence emission and laser emission from a droplet containing *E. coli* before (top row) and after (bottom row) adding ampicillin.

4.1 Experimental Method

4.1.1 Bacteria Preparation and Culture

Escherichia coli O114 (ATCC 25922) was inoculated into a 10 mL LB (Luria-Bertani) broth and cultured overnight in a 37°C incubator, and equivalent to bottles with 1 ml volumes. 1 ml of the stored *E. coli* was mixed with 10 mL of LB broth and cultured at 37°C for 3 h with a shaking speed of 180 rpm. After culture, the bacteria were serially 10-fold diluted with sterile PBS (Phosphate Buffered Saline) to prepare bacteria suspensions with different concentrations of bio-ink for fluorescence or laser experiments. For verification of bacteria concentration and viability, bacterial samples were serially diluted with sterile PBS, and surface plated on the LB agar plates. After incubating at 37°C for 22–24 h, the visible colonies of bacteria were counted to calculate the concentration.

4.1.2 Preparation of Bioink and Ampicillin treatment

For the preparation of bioink, *E. coli* were pelleted by centrifugation and resuspended in PBS for 15 min at 3800 rpm twice. The cells were then labeled with SYTO BC green fluorescent nucleic acid stain (Thermo Fisher #B7277) by mixing the solution with 4 µl of 5 mM dye for 1 hour at room temperature. After checking the fluorescence of stained cells under the fluorescence microscopy, the stained cells will be ready for printing. PBS was obtained from Vivantis (Malaysia). Glycerol was purchased from Promega Corporation. Ampicillin was purchased from Sigma-Aldrich (St. Louis, MO, USA). The stained *E. coli* cultured in LB Broth was mixed with glycerol (volume ratio 1:1). Ampicillin was then added into the solution to a final concentration of 200 µg/mL. The prepared solution was reacted for 5, 10, 15, 20 minutes under room temperature and printed on a dielectric mirror (Fig.4.2), respectively.

4.1.3 Electric Field Simulation

The electric field of WGM resonators and their Q-factors were calculated with the finite element method using COMSOL Multiphysics software. The eigenfrequency

study was applied in the electromagnetic waves, frequency-domain interface within the wave optics modules. For all the simulation, a 2D axisymmetric model was employed. The geometries of the droplet resonators were set to be parts of perfect rounds, and the refractive index (RI) was 1.4. For the Q-factor calculations, a reflectivity of 99.90% was considered for a high reflective bottom mirror and 11.11% for a low reflective substrate. The Q-factor value was chosen from 150 solutions around 530 nm wavelength obtained by COMSOL Multiphysics software.

4.1.4 Configuration of Printer

A commercially avaliable Epson Lp120 printer was selected to fabricate *E. coli* array. The original ink pad was removed and changed into four 1000 μL pipet tips. After processing head cleaning by using water and ethonal for three times, bioink containing *E. coli* could be added. The printer was controlled by modifying the control algorithm downloaded from Epson's website.The printhead has three sizes, by changing the size, different volume of droplet can be dispersed. And by setting different printing times, larger droplet can be achieved through merging with droplets printed before. By adjusting the parameters, the volume and diamter of droplet could be fully manipulated.

4.1.5 Optical System Setup

A microscopic system (Nikon Ni2) with a 10X 0.3 NA objective was used to pump the droplet array and collect light (Fig.4.2). Optical pumping was achieved by a pulsed ns-laser (EKSPLA PS8001DR) integrated with an optical parametric oscillator with (repetition rate: 50 Hz; pulse duration: 5 ns; pulse energy: 5 mJ). According to the respective absorption wavelength of fluorophores, the pump laser was tuned to 490 nm to match the excitation of Syto-BC. The beam diameter at the objective focal plane was approximately 40 μm. The collected light was transmitted to a charge-coupled device camera or an imaging spectrometer (Andor Kymera 328i and Newton 970 EMCCD). For measurements of fluorescence image, an integrated LED was used as the excitation source and imaged by a CCD (Andor Zyla SCMOS) mounted on the microscope.

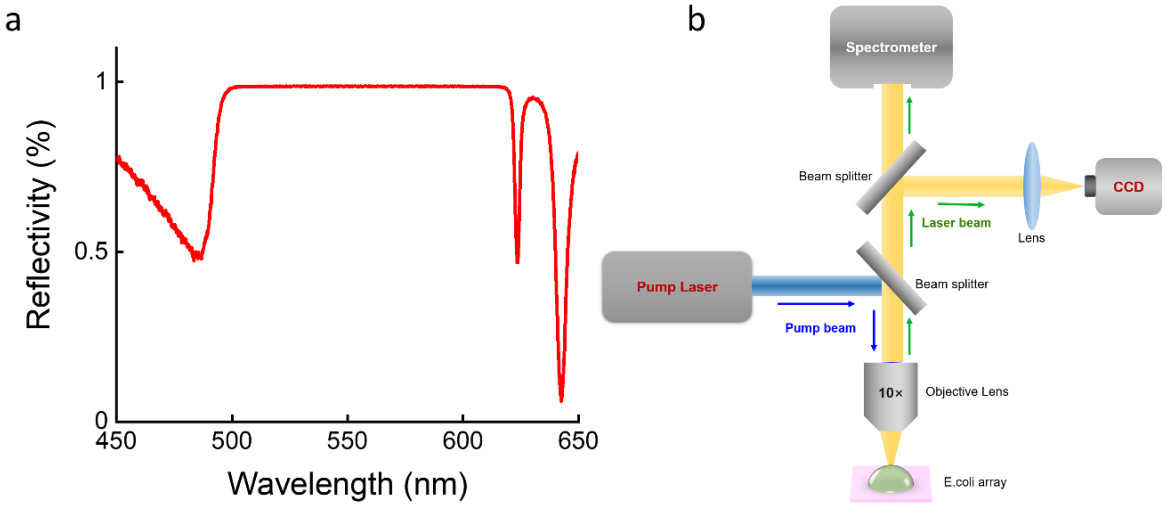

Figure 4.2 (a) Reflective profile of the dielectric mirror used in experiment. **(b)** Schematic diagram of the optical system.

4.1.6 Laser Image Processing

The original RGB images were first converted from RGB to greyscale. Next, the outline of a droplet was fitted by a crircle with the radius of r using MATLAB. Since the WGM lasing mainly focus on the edge of droplet. A ring area with the outer radius of r+5 pixels and an inner radius of r-5 pixels were then selected for further analysis, in which 10 pixels were enough to include all the pixels that contributed to lasing.

4.2 Results and Discussion

4.2.1 Investigation of Lasing Behaviors of *E. coli* Array

We first explored the possibility of fabricating *E. coli* lasing array with an office inkjet printer. By using a mixture of *E. coli*, glycerol, and cell medium as the bio-ink, *E. coli* was printed and encapsulated in the microdroplets on a dielectric mirror which can provide better optical confinement[113]. The successful encapsulation of *E. coli* inside each droplet was confirmed using a fluorescence microscope, as shown in Fig.4.3a. Laser emission was generated upon excitation (490 nm) based on WGM modes. The free spectral range (FSR) was asured to be 1.6 nm in Fig.4.3b, corresponding to a diameter of 40.0 μm (the theoretical calculation of FSR follows: $\Delta\lambda = \frac{n\pi D}{\lambda^2}$). In order

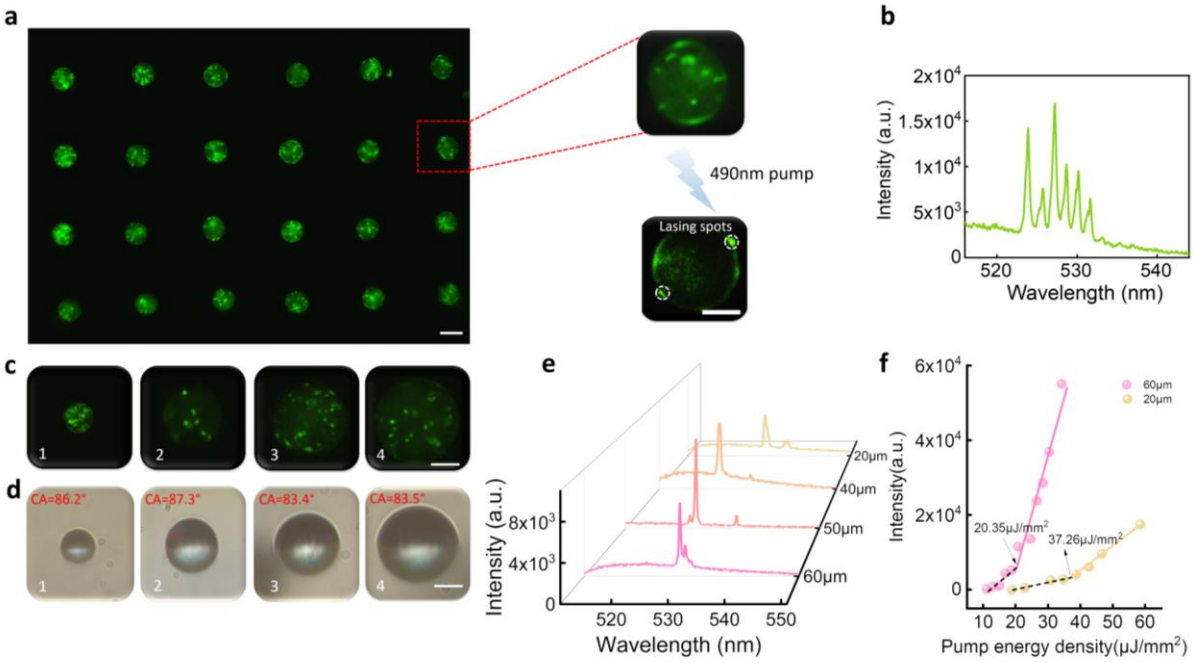

Figure 4.3 (a) Fluorescence image of printed *E. coli* microarray. Scale bar, 40 μm. Right panel: An enlarged fluorescent image of a droplet containing *E. coli* (top). Laser emission image of droplet after pumping by 490 nm pulsed laser excitation (bottom). Scale bar, 20 μm. **(b)** Lasing spectrum recorded from a 40 μm droplet above its lasing threshold.Pump wavelength: 490 nm. **(c-d)** Fluorescent images of printed droplets ranging from 20 μm to 60 μm. Side view images of corresponding droplets. Scale bar, 20μm. **(e)** Lasing spectra measured from droplets with different diameters. Excitation wavelength: 490 nm. Pump energy density: 43 μJ/mm^2. **(f)** Lasing threshold comparison between a 60 μm droplet and a 20 μm droplet.

to ensure the existence of WGM modes, simulations based on contact angle and reflectivity were conducted through COMSOL. The results showed that the Q-factor of WGM mode is around 70000 with the existence of high-reflectivity bottom mirror, which is significantly higher than the Fabry-Perot mode formed between droplet surface and bottom mirror (Q~169).

Taking advantage of the versatility of printer, droplets with different sizes could be fabricated by adjusting the parameters in printer. As shown in Fig.4.3c, droplets ranging from 20 μm to 60 μm were fabricated. To elucidate the consistency of such method, the side views of individual droplets with different diameters were recorded and statistics on droplet size and contact angle were also conducted (Fig.4.4). Fig.4.3d

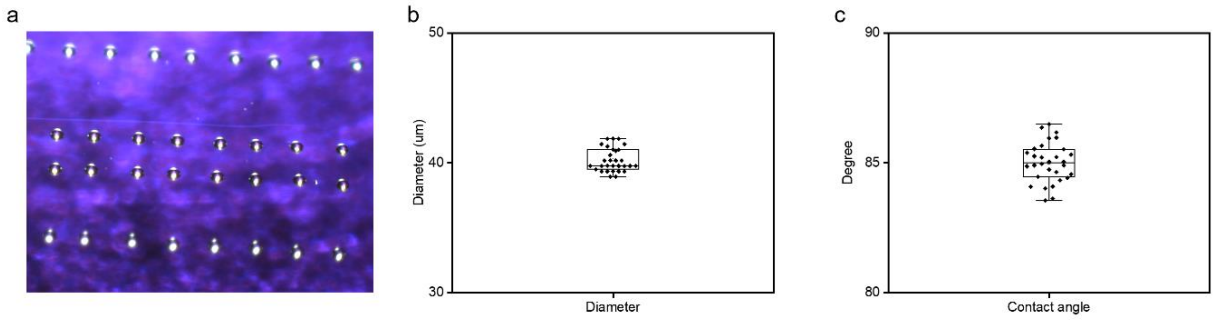

Figure 4.4 (a) Side view image of the printed array. **(b-c)** Statistics on the droplets sizes and contact angle.

presents the differences between the contact angle for the droplets of various sizes. A decrease of 3 degrees was observed for larger droplets, which is a result of competition between gravity and surface tension. Moving forward, lasing performance of different size droplets was investigated. Fig.4.3e shows lasing spectra recorded from individual droplets. With a larger size, the lasing intensity was observed to be stronger due to the increase of cavity Q-factor and the total quantity of *E. coli* encapsulated within the droplet. Such changes could be observed through lasing threshold, as compared in Fig.4.3f.

4.2.2 Influence of *E. coli* Quantity

Next, we investigated the minimal quantity of *E. coli* required for lasing under a fixed droplet diameter of 40 μm (volume~ 1.67×10^{-8} cm^{-3}). By adjusting the *E. coli* concentration in bioink, different concentrations could be progammed and printed. Fig.4.5a presented the fluorescence images of printed droplets encapsulated with different amounts of *E. coli*. In order to evaluate the reproducibility of such printing method, a statistic calculation of *E. coli* were performed in 30 droplets. For a *E. coli* concentration of 1×10^{9} CFU/mL, the theoretical number of *E. coli* in each droplet should be 16. Our result in shows that the number of *E. coli* within each droplet is consistent, which also agrees well with the theoretical number calculated before.

As presented in Fig.4.5b, strong lasing emission was observed for droplets encapsulated with 16 and 8 *E. coli*. The corresponding lasing spectra were measured

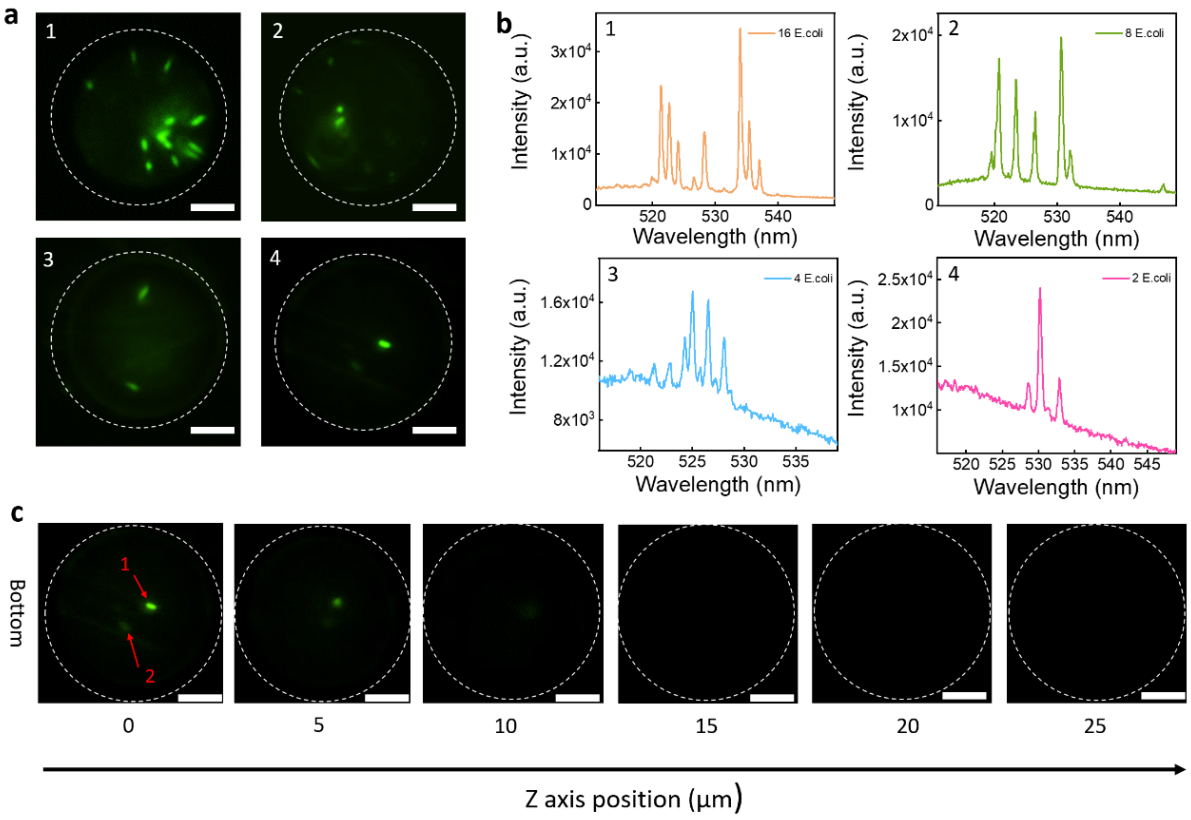

Figure 4.5 **(a)** Fluorescence images of droplets with different *E. coli* concentrations (cell count per fixed droplet volume). No.1-4 represent droplets containing 16, 8, 4, 1~2 *E. coli*, respectively. **(b)** Lasing spectra measured from droplets No.1-4. **(c)** Fluorescence images recorded from droplet with only 1~2 *E. coli* on different Z-focus planes. Considering the height of the droplet height was 20 μm, the Z-scanning covered 25 μm which should be enough to include the whole droplet. Only 1~2 *E. coli* were observed. All scale bars, 10 μm.

at a pump energy density of 78 μJ/mm^2. At a relatively lower *E. coli* concentration, a higher lasing threshold was required to obtain lasing. To our surprise, lasing was achieved from droplets containing only 1~2 *E. coli*, as shown in Fig.4.5b. To confirm the actual quantity of *E. coli*, fluorescence images were taken at different Z-planes (Fig.4.5c). Note that the lasing intensity and signal-to-background ratio is determined by the amount of *E. coli* that participated in WGMs near the surface of microdroplets.

4.2.3 Quantitative Analysis of Laser Emission Images

To investigate its potential in high-throughput lasing analysis, laser images were successfully recorded by scanning over a 4×4 microlaser array with encapsulated *E.*

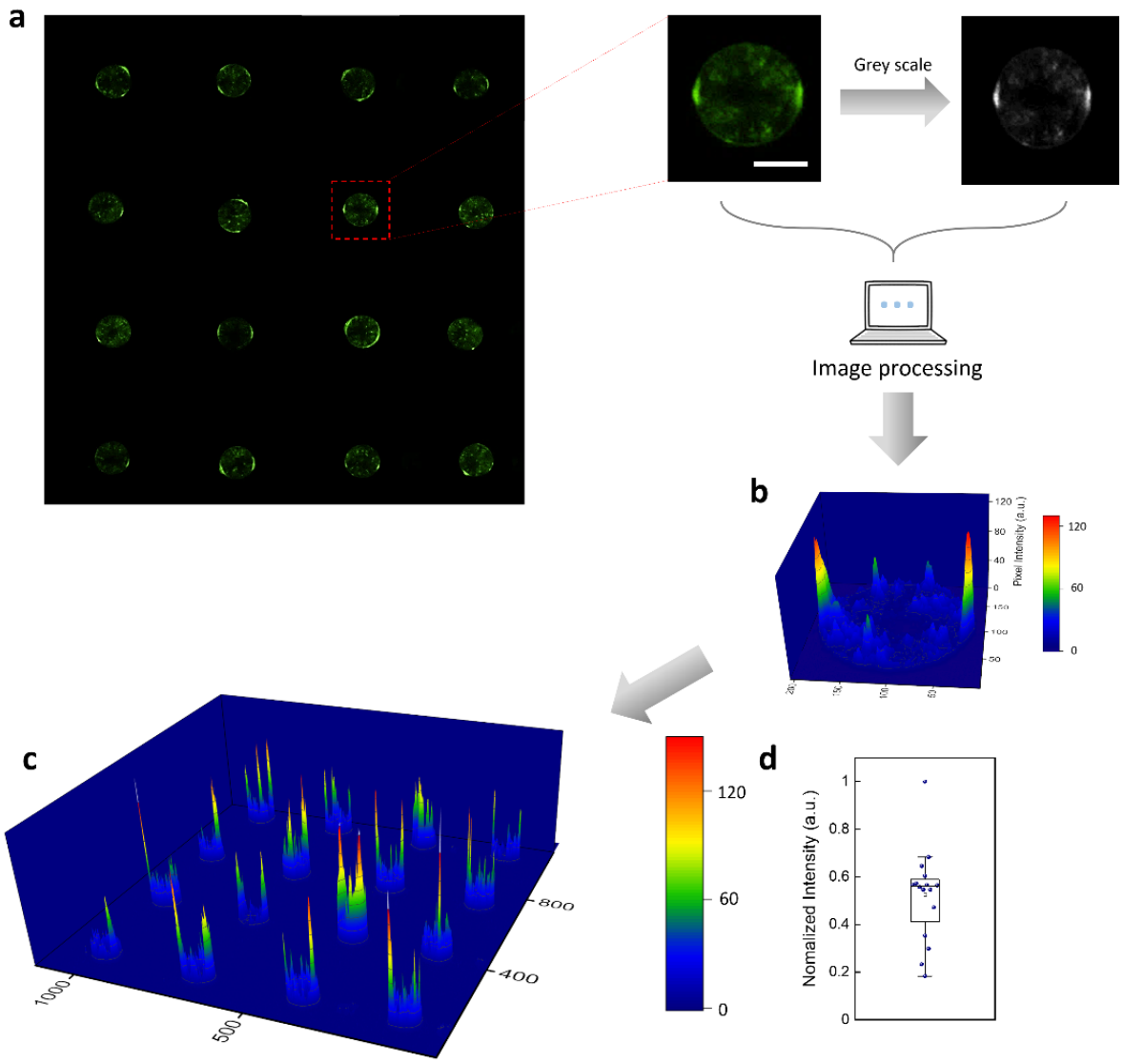

Figure 4.6 (a) Laser emission image recorded from a 4×4 *E. coli* array (left large image). A bandpass filter (510-550 nm) was applied during experiment to eliminate the influence of pump light. Right images: converting a single lasing droplet from RGB to greyscale. **(b)** The pixel intensity profile extracted from the greyscale image in (a). **(c)** Pixel intensity distribution profile extracted from the *E. coli* biological microlaser array. **(d)** Statistic of pixel intensity integration of each droplet in **(a)** after subtracting the fluorescence background (pure lasing signals). Scale bar, 20 μm.

coli (Fig.4.6a). Bright lasing spots were observed at the edges of each droplet, which is the result of scattered WGM lasing emission.

For better visualization, the original lasing image was converted from RGB to greyscale. Subsequently, the 2D image was plotted into a 3D distribution of pixel

intensity profile for quantitative analysis. For instance in Fig.4.6b, the pixels along the edge of the droplet have extremely high intensity, representing strong WGM lasing signals from *E. coli*. On the contrary, the vast majority of lower intensity pixels resulted from the remaining fluorescence emissions. By applying the proposed methodology, the image of microlaser array (Fig.4.6a) was converted into a 3D pixel intensity profile, as shown in Fig.4.6c. In order to attest the reliability of such method, we statistically analyzed the total pixel intensity for individual droplets in the array. The result in Fig.4.6d demonstrates that the distribution of total pixel intensity is relatively consistent in most lasing droplets, which is an important characteristic for quantitative analysis.

4.2.4 Analysis of Interactions with Antibotic Drugs

Finally, we demonstrated how such a microarray could be exploited to realize living organisms and their responses when excited with an external stimulus. To date, many antibiotic drugs have been used to study the dynamic changes and interactions with *E. coli*. Ampicillin is a FDA approved drug which has effective inhibitory effects for most of the medically essential organisms in infectious disease[114-116]. As shown in Fig.4.7a, by adding ampicillin into the droplet, the cell membrane of *E. coli* would be destroyed and, in turn, release its DNA into an external medium. Therefore, the morphology of *E. coli* will change from long-tube shape to irregular or rounded shape after loosing its bio-functions. The interaction between ampicillin and *E. coli* can be observed where the quantity of *E. coli* decreased obviously after 15 minutes reaction. As ampicillin interacts with *E. coli*, more fluorescent DNA (gain molecule) will be released into the droplet through time and contribute to WGMs, resulting in stronger laser emission. Fig.4.7b presents the laser images recorded from 0 to 20minutes after adding ampicillin in the droplets. We can see the scattered WGM lasing signal increased dramatically; however, the lasing intensity reaches a maximum value after 23 minutes (Fig.4.8). As a comparison, fluorescence images were also recorded in Fig.4.7c. However, the intensity saturated after 5 minutes and thus could not reflect the subtle dynamic changes of *E. coli* in droplets anymore.

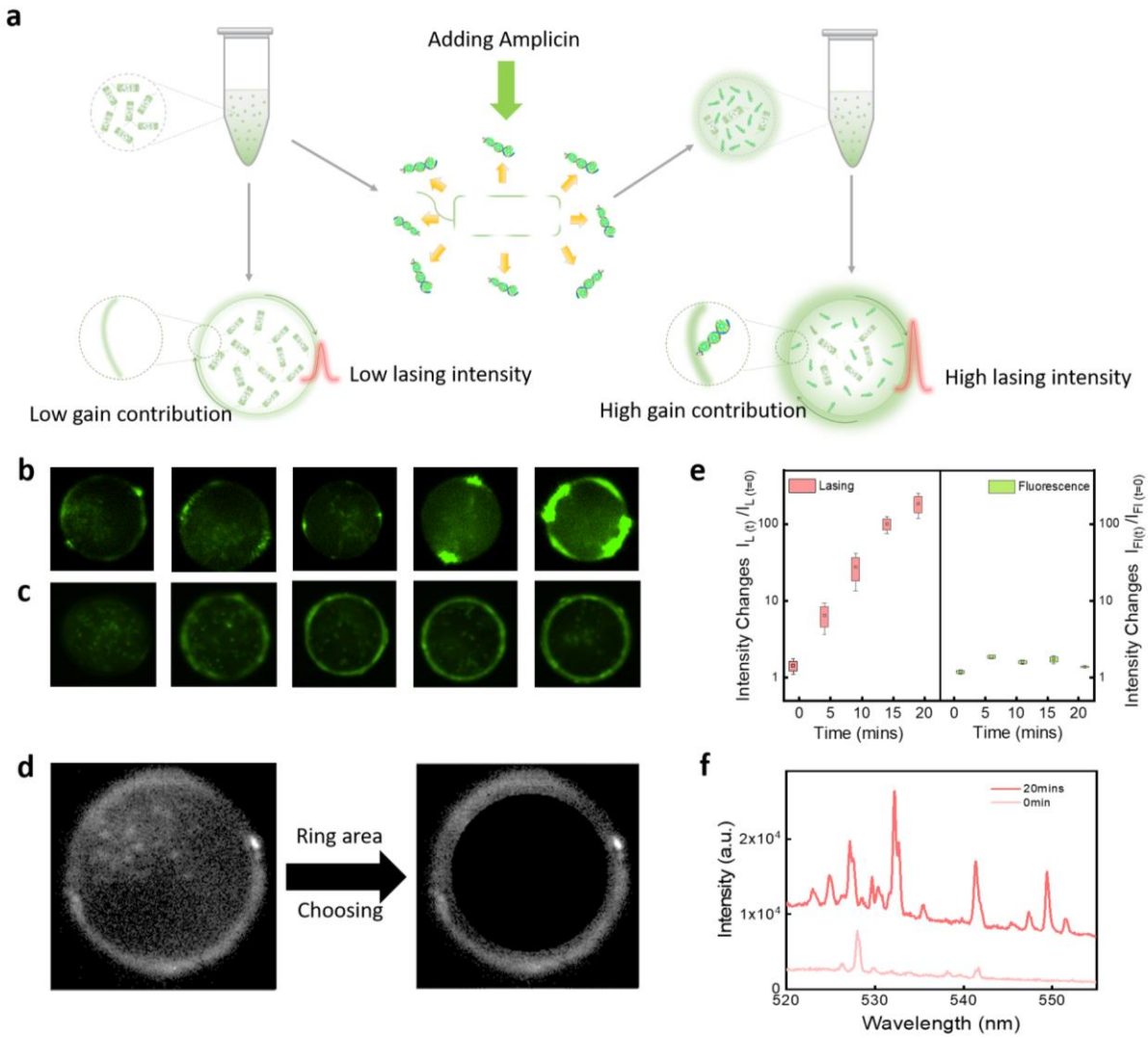

Figure 4.7 (a) Schematic diagram showing the function of ampicillin and changes of gain distribution inside a droplet cavity. **(b)** Laser images recorded from droplets after adding ampicillin for 0, 5, 10, 15, 20 minutes. **(c)** Fluorescence images recorded from droplets after the same process as in **(b)**. **(d)** Concept of image processing: only the pixels inside the ring area were extracted for lasing analysis. **(e)** Dynamic changes of intensity acquired from laser emission images and fluorescence images after adding ampicillin for 0, 5, 10, 15, 20 minutes. The normalized intensity changes were calculated by comparing the integrated pixel intensity at respective times to the intensity at t=0. **(f)** Lasing spectra measured from droplets before (0 min) and after adding ampilicin for 20 minutes. All droplet sizes: 40 μm. All the images and spectra were recorded under the same pump energy density. For each time interval, 8 droplets were measured for the statistics in (e).

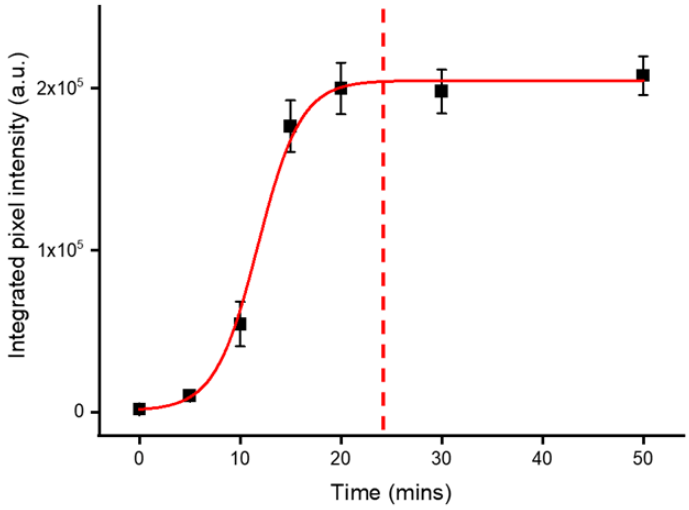

Figure 4.8 Integrated pixel intensity of lasing images after adding E. coli for 0, 5, 10, 15 ,20, 30, 50 minutes. The intensity saturated around 23 minutes.

In order to ensure our observation, a quantitative analysis was carried out for both lasing-based and fluorescence-based images. For quantification of fluorescence images, the pixel intensity of the whole droplet was integrated. For the quantification of lasing images, an algorithm was developed to quantify the total pixel intensity of the lasing signals emitted from droplets' surfaces. The actual image pixel area that was considered for lasing analysis is shown in Fig.4.7d, where the majority of laser signals are located.

Here we compared the integrated pixel intensity extracted from laser images and fluorescent images in Figs.4.7b and c respectively after interacting with ampicillin. Subsequently, we calculated the dynamic changes of lasing image intensity $I_{Laser(t)}/I_{Laser\ (t=0)}$ (integration of pixel intensity for pixel contributed to lasing) and plotted in the left panel of Fig.4.7e. Apparently, laser imaging presented a significant increase of integrated pixel intensity by two orders of magnitude. On the other hand, we also calculated the dynamic changes of fluorescence image intensity $I_{Fl(t)}/I_{Fl\ (t=0)}$, as shown in the right panel of Fig.4.7e. The results show that the fluorescence intensity remains at a similar level after 20 minutes. The differences were also confirmed by lasing spectra after adding ampicillin for 0 min and 20 minutes in Fig.4.7f, demonstrating the distinct ability to monitor dynamic changes. An enhancement score of 10^2 was

achieved here. However, there is one thing to be noted in this method. The excitation light plays a pivotal role in the behavior of lasing images. It has been observed that as the excitation increases, the pixel intensity on the lasing image similarly elevates. This scenario, however, is suboptimal for applications that utilize lasing images. The reason for this is that these applications depend on the integration of pixel intensity to augment their final value. When pixel intensity reaches saturation, diminishing differences are observed despite any increase in actual laser intensity. Therefore, selecting an appropriate pump intensity to initiate the experiment becomes crucial.

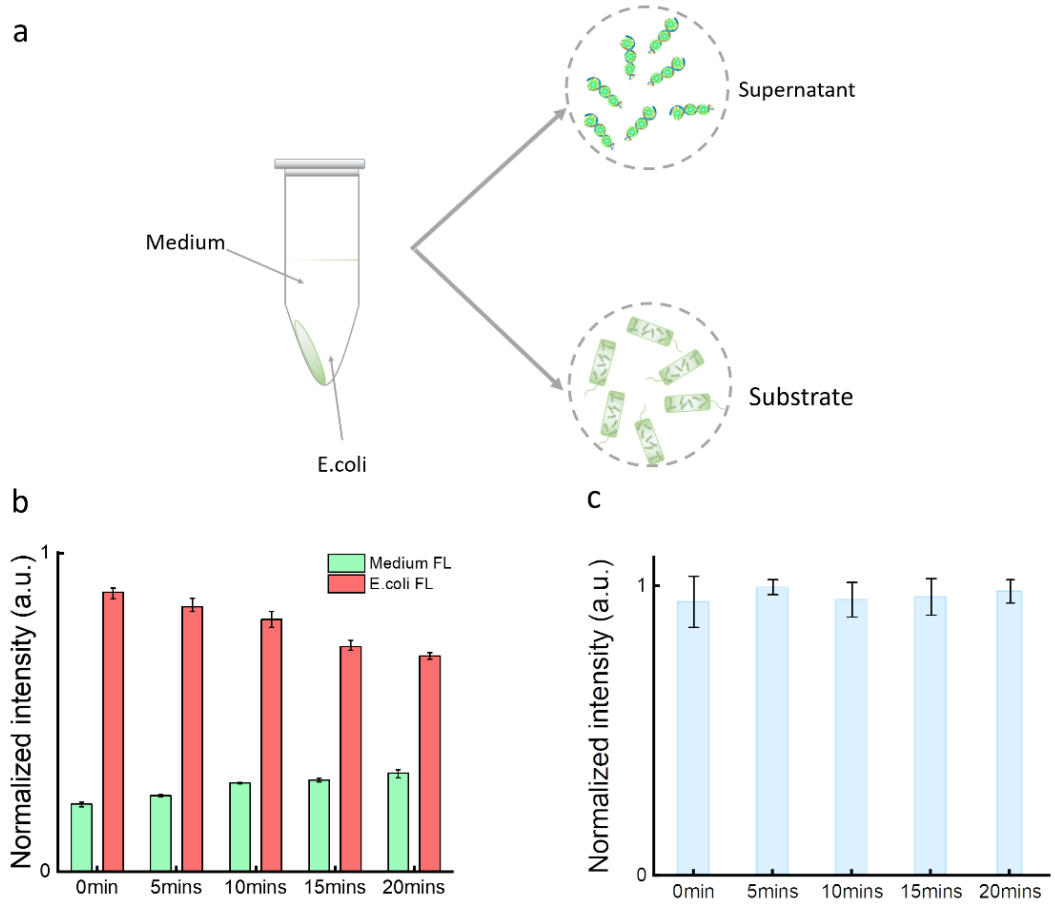

Figure 4.9 (a) Schematic diagram showing the substances in supernatant (fluorescent DNA) and substrate (E. coli) after centrifuge. **(b)** Fluorescence intensity measured from supernatant and substrate (after centrifuge) under different treatment periods. **(c)** Control group: Fluorescence intensity from original bio-ink after adding ampicillin under different treatment periods (without centrifuge). All the intensities were based on the readout from fluorescence spectrometer.

In order to confirm that this phenomenon was attributed to the release of fluorescent DNA in *E. coli*, the fluorescence intensities from both supernatant and substrate were quantified respectively after centrifugation (Fig.4.9a). As shown in Fig.4.9b, the fluorescence intensity of supernatant increased after ampicillin treatment, while the fluorescence intensity of the substrate decreased gradually from 0 min to 20 min. Additionally, the total fluorescence intensity of the original bio-ink was measured before centrifugation. From Fig.4.9c, it can be seen that no obvious difference in fluorescence intensity changes was observed after ampicillin treatment, implying that the total amount of fluorophores remained the same in the droplets. In contrast, the release of fluorophores into the droplet medium changes the laser gain distribution, thus changing the lasing output significantly.

4.3 Conclusions

To date, a plethora of sensing technologies have been developed for the recognition of pathogenic bacteria based on advanced nanostructured materials, including surface plasmon resonance, carbon-based nanomaterials, quantum dots, surface-enhanced Raman scattering, and electrochemical detection[117-123]. Such optical or electrical-based methods acquire biological information through the chemical reaction between the surface moieties on nanostructure and the bacteria. Additionally, these methods usually can visualize a detailed image of a single bacteria when integrated with an imaging tool, therefore can be used to track the motion or structural changes of individual bacteria. However, these nanostructured-based methods require specific design of chemical reactions and complex device fabrication. Compared with such methods, the proposed biological microlaser array simplifies the preparation process with a common office printer while maintaining a high sensitivity. Although laser images can provide the integrated information inside each droplet, it lacks the ability to monitor the physiological activities of individual bacteria. Another disadvantage of lasing and fluorescence-based methods is the requirement for labeling, which may suffer from low stability. To increase the stability of the gain

material and endow laser with responsiveness to pathogenic reactions, the possibility of combining both functional nanomaterial and lasing could be exploited in the future. In summary, we have developed an inkjet-printed optofluidic biological microlaser array which can encapsulate living organism for bioanalysis. Most importantly, a novel approach for bioanalysis based on laser emission images was proposed to quantify the underlying biochemical and biological processes *in vitro* or *in vivo* in a live organism. As a proof-of-concept, *E. coli* was exploited for dynamic lasing analysis under antibiotic drug interactions. Our results show that the amplification that occurs during laser generation enabled us to quantify tiny changes in biological processes in the gain medium. Finally, an image-based lasing analysis for *E. coli* was demonstrated to be much more sensitive to dynamic changes than fluorescence analysis. The same approach could be applied to a wide range of living species, including living cells, bacteria, viruses, and proteins interactions.

Here we would like to point out a few perspectives. First of all, the concept of inkjet-printed biological microlaser array possesses the unique advantages of high-throughput fabrication and programmable controllability. Unlike microfluidic chips which require complicated micro-fabrication, the printing method can quickly generate massive dimension of lasing droplets on-chip within 1-2 seconds. The size, volume, and design of microdroplet array can be easily controlled through software. It should also be noted that only an office inkjet printer is required to fabricate the microarray in this work, which is very cost-effective and time-efficient. Second, the key innovation of this work is to employ laser emission images to quantify dynamic changes in living organisms. In comparison to conventional lasing spectra analysis, image-based analysis provides a rapid platform to analyze the laser emission signals. With the integration of high-repetition rate laser and galvo-scanner, the speed for data acquisition could be significantly improved in the future. Third, we would like to point out that the proposed platform can be applied to any lasing wavelengths, depending on the fluorophore selected to label the living species. Taking advantage of the narrow linewidth of lasing signal, multiplexed detection may also be possible in the future.

Chapter 5: Enzyme-Programmable Microgel Lasers for Information Encoding and Anticounterfeiting

In Chapters 3 and 4, we demonstrated the capacity of the fabricated laser array to detect both chemical molecules and living organisms, thereby highlighting its potential in chemical analysis. Beginning with this chapter, we aim to delve deeper into the multifaceted applications of such a hydrogel microlaser array, particularly focusing on its utility in physical domains, such as in anti-counterfeiting measures.

With the advent of information explosion in the last decade, information encryption has gathered tremendous attention in data protection, anticounterfeiting, as well as secured communication.[124-126] Among various strategies, optical information encoding possesses a high accuracy and versatility by exploiting a distinctive absorption band, or other emission intensity, wavelength, polarization, resonance modes, structural colors, and chirality upon specific stimulation or excitation.[127-133] Encoding methods based on optical nanostructures possess the strong ability to manipulate light at the nanoscale with high controllability,[134, 135] however, the fabrication is usually cost-intensive and challenging for mass production. Most reflected or transmitted light usually have a very broad band, which makes it difficult to conduct huge color capacity. On the other hand, anticounterfeiting technologies based on photoluminescence are the most widely used candidate in the field owing to their vivid visualization, facile authentication, and are generally easier to fabricate into large dimensions with solution-processed techniques. Luminescent materials including organic fluorophores, nanocrystals, quantum dots, and transition-metal complexes have been incorporated with various photonic structures and platforms for optical encoding[136-142]. However, photoluminescence signals usually have a relatively broad emission band, resulting in a relatively low security level. In comparison with broadband photoluminescence, laser emission (stimulated emission) provides a promising route for optical encoding with new coding elements, generating feature-rich emission spectra corresponding to changes of gain materials and cavity

geometry. To date, various types of lasing configurations have been explored and demonstrated for optical encoding from micron to nanoscale, including whispering-gallery modes and random laser.[49, 143-150] The narrow linewidth of laser emission spectra can be converted into barcodes with a higher level of multiplexing and complexity for distinguishable readout. Meanwhile, laser emission may offer an opportunity to surpass conventional physical dimensions, including wavelength and polarization.[2, 151-154] For instance, multi-vortex laser beams can create an unlimited number of orbital angular momentum quantum states in principle, which can be used as powerful tools for optical encoding.

While many laser encoding methods have been developed, state-of-the-art lasers require synthetic materials or precise fabrication. In contrast, naturally responsive biomolecules have attracted tremendous attention in creating controllable biointerfaces that can recognize and regulate signals into macroscopic physical or chemical behaviors under stimuli.[97, 155] Active molecules such as DNA, silk, and proteins have specific reactions to certain stimuli, are ideal agents to achieve alternation on samples in terms of inner structure, surface charge, and even absorption.[12, 52, 146, 156, 157] Owing to the intrinsic structural diversity and chemical reactivity, such biomolecules not only enable a higher level of functionality to tailor optical responses at nanoscale but also retain excellent data storage capacity. The high complexity and randomness of biomolecular interactions provide an unclonable feature for anticounterfeiting, which cannot be replicated by other materials. The ability to manipulate and control laser information with biomolecules is therefore significant yet challenging.

Recently, hydrogels have emerged as a promising candidate for interfacing photonics and bioengineering by combining their light-guiding properties with chemically reactive network[35, 68, 74, 113]. Endowed by the hydrophilic group of polymer chains, hydrogel possesses strong water storage capacity and is well-known for its high tunability.[66, 67, 71] Taking advantage of the functional groups on the side chain, hydrogels have demonstrated a higher functionality by responding to various

external stimuli, such as pH, temperature, humidity, and specific biochemical reactions.[34, 158-160] By controlling the network structure or densities, hydrogels can exhibit different optical properties in terms of emission, reflection, and transmission, making hydrogel an attractive material for optical encoding. [161-163] In this study, we proposed a biological encoded laser, where information encoding and anticounterfeiting were both accomplished through enzyme reactions in hydrogels.

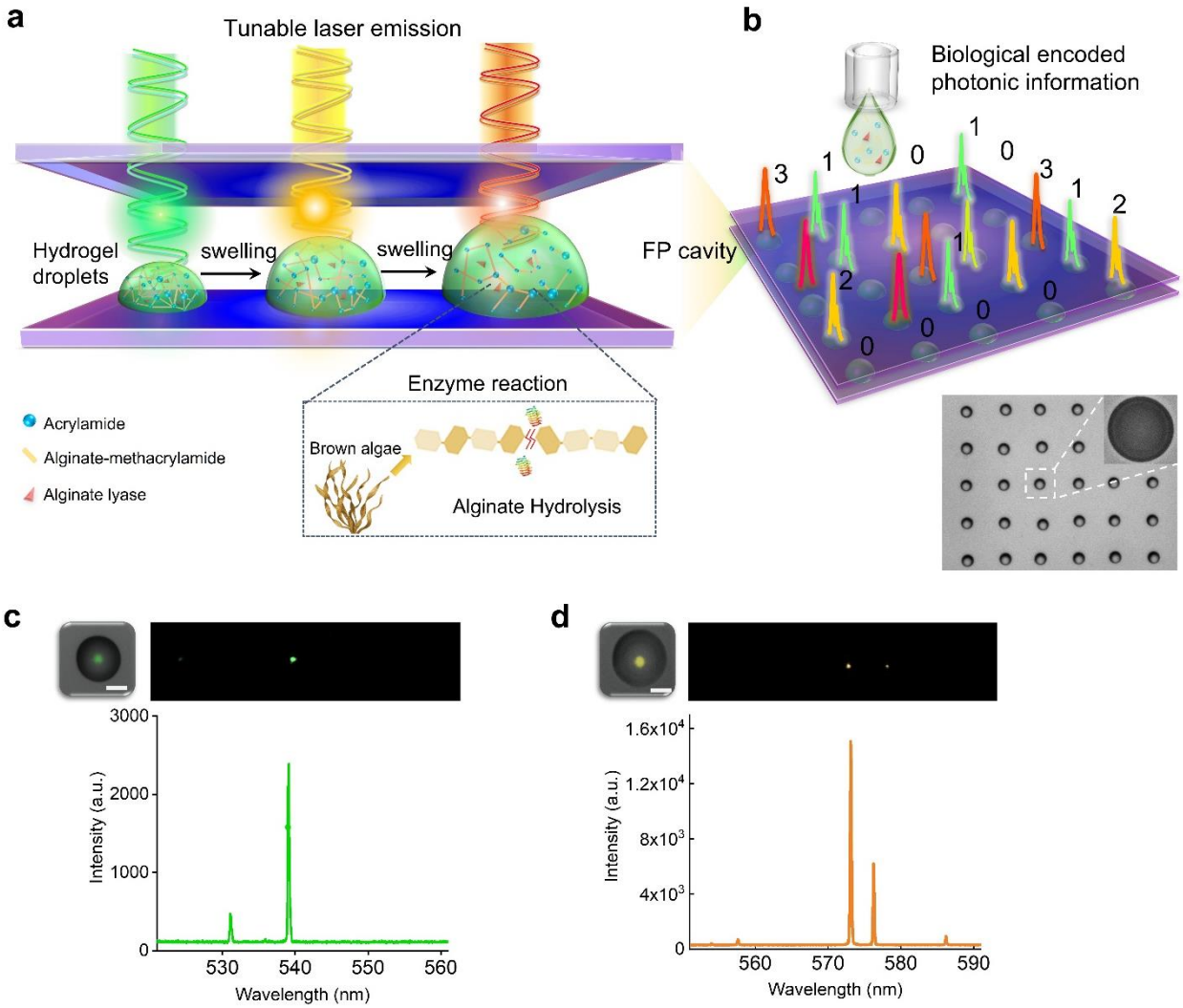

Figure 5.1 (a) Schematic diagram of a biologically controlled hydrogel laser by sandwiching enzyme-responsive hydrogel droplets in a FP cavity formed by two mirrors. **(b)** Schematic showing the realization of laser encoding using hydrogel array. The bottom bright-field image shows inkjet printed PAAm hydrogel array. Droplet diamter:40 μm **(c)** Lasing spectrum of original droplet. **(d)** Lasing spectrum of swelled hydrogel droplet. The corresponding hyperspectral images are provided above its spectra. The top-left image represents the far-field laser emission superimposed on bright-field images. Pump laser: 488 nm. The pump energy density was above their corresponding lasing threshold. Scale bars, 20 μm.

Fig.5.1a illustrates the concept of biologically tunable hydrogel laser, where hydrogel droplet arrays were sandwiched between a Fabry–Pérot (FP) cavity formed by highly reflective mirrors. As shown in the inset of Fig.5.1a, polyacrylamide (PAAm) hydrogel cross-linked by alginate methacrylate (M-AAm) was designed to respond to specific interactions. By tailoring the hydrogel structure with alginate lyase, lasing emission could be adjusted accordingly with the different swelling abilities of hydrogel. Laser emission corresponding to green, yellow, and orange could be controlled at different locations in the array through reaction time or enzyme concentration. Theoretical calculations revealed that the inner 3D-network structures and external curvature of encapsulated hydrogel droplets could be used to control the lasing thresholds and resonance wavelengths. As a proof of concept, we demonstrate the promising potential of such hydrogel laser for laser information encoding (Fig.5.1b). By altering the pump energy density, different emission states of the printed array can be achieved to reflect true and false information, respectively. Finally, hyperspectral laser images were utilized as an advanced feature for a higher level of security. The results may provide inspiration on the rational design of biological tunable laser with performance based on biological materials and conventional photonics.

5.1 Experimental Method

5.1.1 Materials and Chemicals

The dye we used in this work was Fluorescein O-methacrylate (Sigma Aldrich #568864). For hydrogel, Acrylamide (Sigma Aldrich #A9099) was selected as monomer. N,N′-Methylenebis(acrylamide) (Sigma #146072) was crosslinker to form 3D structure, 2-Hydroxy-4′-(2-hydroxyethoxy)-2-methylpropiophenone (Sigma #410896) as photoinitiator to trigger polymerization. Alginate methacrylate (metharylation 30%) (Sigma Aldrich #913507) was chosen as crosslinker to modify the hydrogel. Alginate lyase (Sigma Aldrich #A1603) was used to trigger the degradation of the hydrogel structure.

5.1.2 Laser Cavity Preparation

The Fabry–Pérot cavity was fabricated by using a pair of highly reflective dielectric mirrors (distributed Bragg reflector). Each mirror is composed of a glass substrate coated with dielectric layers with periodic refractive indices, providing high reflections at specific lasing wavelengths. The mirrors were home-made; however, commercialized dielectric mirrors with high reflection can also be used. The droplets were directly printed and sandwiched between the two mirrors, and the cavity length was fixed by using glass microbeads with 45-μm diameters as spacers (Fig.5.2).

5.1.3 Droplet Fabrication

For normal PAAm hydrogel droplets, 0.475 g acrylamide and 0.025 g Bis-AA were dissolved in 500 μL Tris buffer to prepare precursor solution. Furthermore, 45 mg photoinitiator was added into the solution to trigger polymerization after UV curing (Panasonic #ANUJ3500). 4 mg F-MA was added into the solution as gain material. Finally, the prepared solution was added into a modified office printer and printed on the dielectric mirror.

For M-AAm modified droplets, 0.475 g acrylamide and 20 mg alginate methacrylate were dissolved in 500 μL Tris buffer. To achieve different hydrogel structures, alginate lyase was added into the prepared solution to final concentration of 10, 40, 70, and 100 μg/mL. After adding 45 mg photoinitiator, the solution was printed into array by a microplotter (Sonoplot Microplotter). For all hydrogel droplets, the UV curing time was fixed as 10 seconds.

5.1.4 Optical System Setup

A microscopic system (Nikon Ni2) with a 10X 0.3 NA objective was used to pump the droplet array and collect light. Optical pumping was achieved by a pulsed ns-laser (EKSPLA NT230) integrated with an optical parametric oscillator with (repetition rate: 50 Hz; pulse duration: 5 ns; pulse enegry: 5 mJ). According to the respective absorption wavelength of fluorophores, the pump laser was tuned to 480 nm to match the excitation of F-MA. The beam diameter at the objective focal plane was

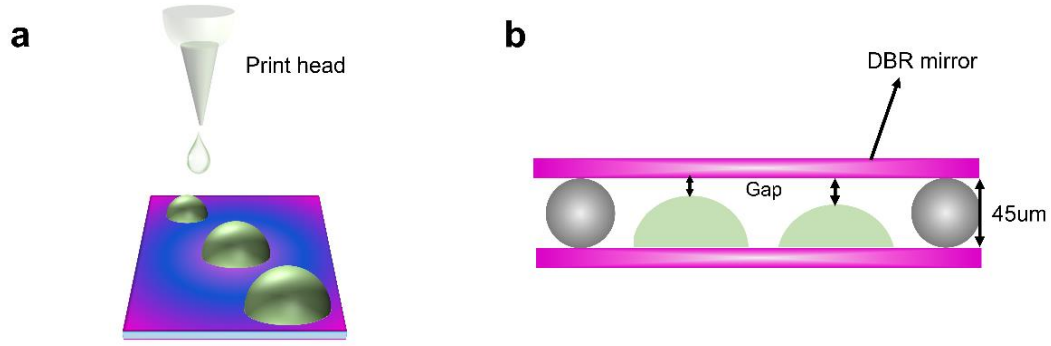

Figure 5.2 (a-b) Schematic showing the structure of FP cavity used in this work.

approximately 40 μm. The collected light was transmitted to a charge-coupled device camera or an imaging spectrometer (Andor Kymera 328i and Newton 970 EMCCD). For measurements of color images (laser and fluorescence), a color CCD (DS-Fi3, Nikon) was mounted on the microscope.

5.1.5 Electric Field Simulation

The electric field of FP resonators and their Q-factors were calculated with the finite element method using COMSOL Multiphysics software. The eigenfrequency study was applied in the electromagnetic waves, frequency-domain interface within the wave optics modules. For all the simulations, a 2D model was employed. The geometries of the resonators were set corresponding to the side view of different droplets, and the refractive index (RI) was 1.4. For the Q-factor calculations, a reflectivity of 99.90% was considered for a highly reflective bottom and top mirror. The imaginary part of refractive index for a 40 μm droplet was set as 5×10^{-4} and decreased proportionally with increased droplet volume. The imaginary index here was set to add the loss that hydrogel caused to the cavity. The value is set as a middle value of the imaginary part of large loss material such as fused silica (10^{-3})[164] and a small loss material which has a value of 10^{-5} for imaginary part of its refractive index[165]. The proportionally decreased value is resulted from the increase of hydrogel droplet volume after swelling, in which the water occupied more space than a lower swelling droplet. We assume that with more water inside the inner structure would be

considered more uniform and have less loss. In this study, the Q-factor value was determined from 150 solutions around the 540 nm wavelength, obtained using COMSOL Multiphysics software. The selection process involved simulating the electric field distribution at the experimentally observed central wavelength and at increments of 0.05 nm on either side, resulting in a total of 150 simulations. From these simulations, we manually selected only those that exhibited the fundamental mode, as observed experimentally, to ensure the accuracy and relevance of our sample data.

5.2 Results and Discussion

5.2.1 Lasing Characteristics of Polyacrylamide Hydrogel Droplet

To achieve lasing, fluorescein-o-methyacrylate (F-MA) was selected as the gain material for all the PAAm hydrogel droplets throughout the entire work. First, we investigate how the hydrogel laser will respond to the change of environmental humidity (water vapor) by exploiting hydrogel cross-linked with Bis-acrylamide (Bis-AA). Fig.5.1c shows the laser emission spectrum of a hydrogel droplet sandwiched between two highly reflective mirrors. With optical confinement provided by FP cavity, the emitted light from F-MA can be amplified through oscillatation, resulting in strong stimulated emission. The lasing spectrum of the hydrogel droplet was observed at 538 nm. After the environment humidity was increased from 60% to 80%, the hydrogel droplet reached a maximum diameter of 56 μm. To our surprise, a redshift of lasing wavelength was observed on the swelled droplet, as shown in Fig.5.1d. The wavelength shift was also confirmed by laser images, as shown in the top inset of Fig.5.1c and Fig. 5.1d, where the laser mode transferred from green to yellow emission. The results here indicate that lasing wavelength could be influenced by the swelling ratio of hydrogel droplets.

To verify lasing actions, we measured the output intensities and free spectral range (FSR) of hydrogel laser in Fig.5.3. The FSR was measured as 2.5nm for two independent droplets (Fig.5.3a-b), which is consistent with the theoretical FSR

(calculate follow the equation: $\Delta\lambda = \frac{\lambda^2}{2nL}$, where *L* is the length of cavity) for FP cavity (48 μm glass beads were used as a spacer). The full wavelength at half maxima (FWHM) is measured as 0.35 nm and 0.61 nm for Fig.5.3a and 5.3b, respectively. However, due to the resolution of our spectrometer, the FWHM measured obtained here is not accurate enough to reflect Q-factor of cavity[166].

Due to the optical lensing effect, hydrogel droplets confine the light tightly in the FP cavity and thus provides a stable resonator for information encoding. The spectrally integrated output intensities were measured under different pump energy densities (Fig.5.3c), where a clear threshold was observed around 36 μJ/mm^2 (Fig.5.3d). To better understand the hydrogel lasing, hyperspectral images of the corresponding droplet were also recorded in Figs.5.2c and 5.2d, showing that the fundamental mode is dominant in such configuration.

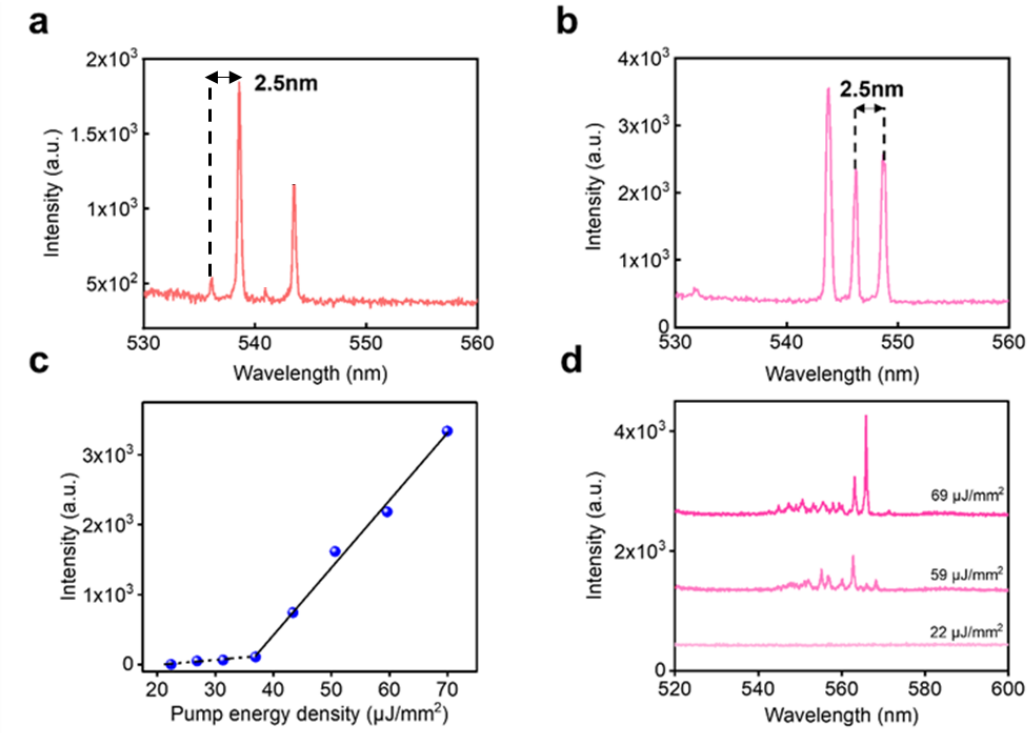

Figure 5.3 (a-b) Spectrum recorded from two different PAAm hydrogel droplet size. Both the measured FSR is consistent with calculated FSR for the FP cavity used in this work. Droplet size: (a) 40 μm; (b) 48 μm. **(c)** Spectrally integrated output intensities as a function of pump energy density from PAAm hydrogel droplets **(d)** Lasing spectra of hydrogel droplet under different pump energy density.

5.2.2 Characterization of Enzyme Reaction and Lasing Wavelength Shift

To achieve a biologically controlled laser, the inner structure of PAAm hydrogel was modified by using alginate-MA as a cross-linker. With the existence of methacrylate connected with alginate chains, alginate binds to polymerized acrylamide chain, forming a 3D hydrogel structure. Alginate lyase is a type of enzyme that can function as a “scissor” to catalyze the degradation of alginate. The chemical bond between alginate monomers would be removed through hydrolysis with the presence of alginate lyase. Herein we employed alginate lyase to tailor the inner structure of M-AAm hydrogel, as illustrated in Fig.5.4a. After adding alginate lyase, the alginate would degrade into small molecules, resulting in the absence of crosslinker and reducing the network density of hydrogel. As a result, the hydrogel would experience a higher swelling ratio under the same environment humidity. In order to systematically study the influence of alginate lyase, two series of experiments were conducted, respectively. Firstly, we investigated the lasing performance under different reaction time with a fixed enzyme concentration (100 μg/mL) as shown in Fig.5.4b, where the sizes of hydrogel droplets change accordingly. From 0 min to 90 minutes, the hydrogel swelling ratio continued to increase and a redshift of lasing wavelength was obtained. The hydrogel swelling ratio saturated after 90 minutes, representing the cease of reaction. Secondly, we investigated the lasing performance by fixing the reaction time with different enzyme concentrations in Fig.5.4c. Similar to the variation shown in Fig.5.4b, the lasing wavelength redshift accordingly. The function of the alginate lyase can be verified by scanning electronic microscope (SEM) images (Fig.5.5). The SEM images show samples with 10 μg/mL and 100 μg/mL alginate lyase after 90 minutes of reaction time. The inner structure of hydrogel demonstrated huge differences upon enzyme reactions. With the increase of enzyme concentrations, the hydrogel structure showed a higher density of pores and larger pore size at the same time. To clearly show that alginate lyase is capable of degrading alginate methacrylate, Gel permeation chromatography (GPC) was employed to measure the molecular

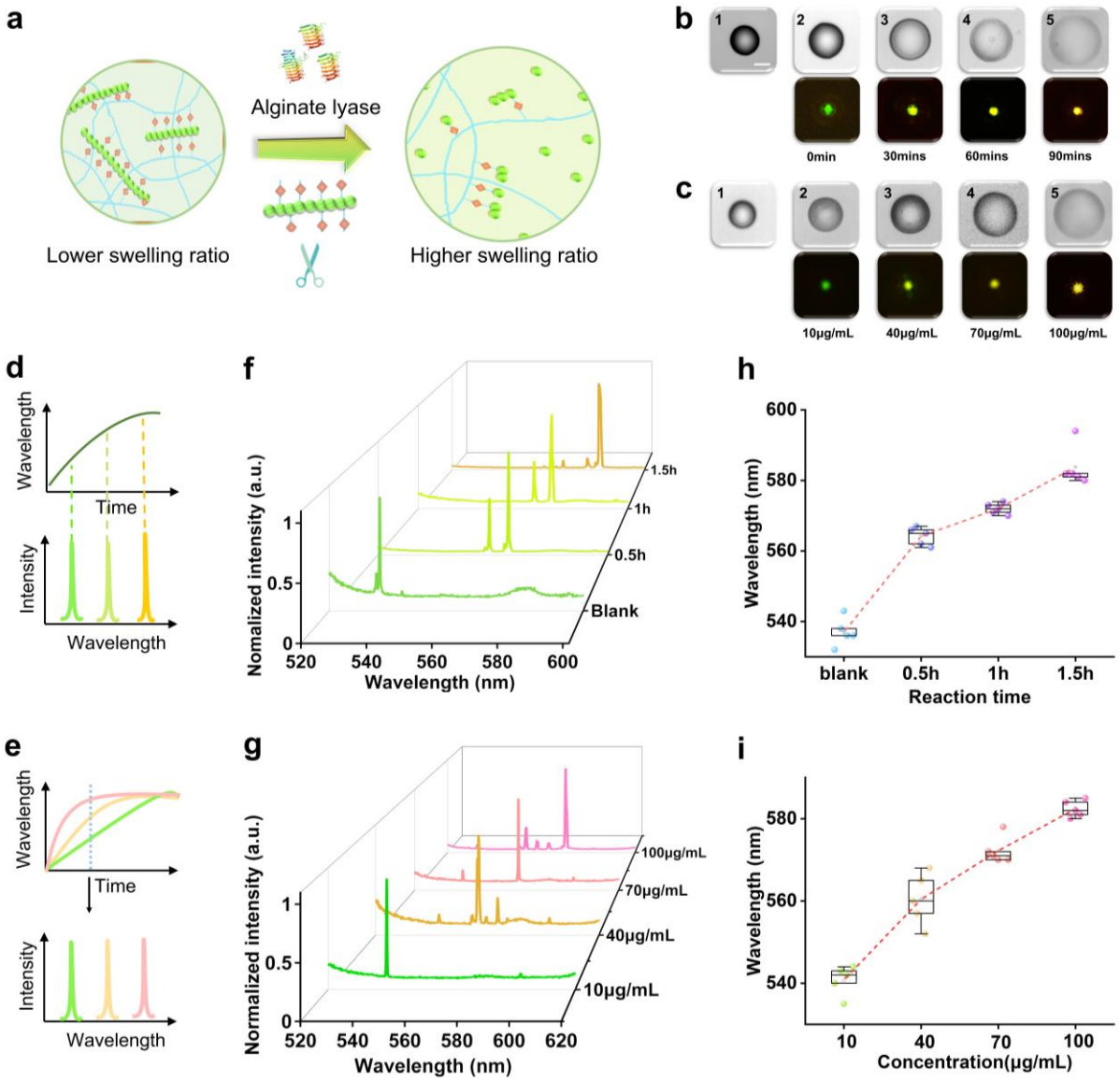

Figure 5.4 (a) Schematic showing the degradation of hydrogel inner network structure before and after adding alginate lyase. **(b-c)** Top**:** Bright field images and corresponding lasing emission images of swelled hydrogel droplets after enzyme reaction for 0 min, 30 minutes, 60 minutes, and 90 minutes. The enzyme concentration was fixed as 100 μg/mL. Bottom: bright field images and corresponding lasing emission images of swelled hydrogel droplets after enzyme reaction for 90minutes. Enzyme concentration: 10 μg/mL, 40 μg/mL, 70 μg/mL, and 100 μg/mL. Scale bar, 15 μm. **(d-e)** Schematic showing the lasing wavelength shift under different reaction time (d) and different enzyme concentration (e). **(f)** Normalized lasing spectra recorded from swelled hydrogel droplets after different reaction time; **(g)** Normalized lasing spectra recorded from swelled hydrogel droplets under different enzyme concentration. **(h)** Statistics of recorded lasing wavelength under different reaction time. **(i)** Statistics of recorded lasing wavelength under different reaction enzyme concentrations.

weight of alginate methacrylate before and after reaction with alginate lyase. From the retention time-response profile (Fig.5.6), we can clearly see that the sample after reaction has longer retention time than the sample before reaction, proving the evidence showing that alginate lyase does catalyze the degradation of alginate with existence of methacrylate. The calculated molecular weight was 3072942 g/mol before and 85467 g/mol after the reaction. Similar reaction was also demonstrated in a previous study. [167]

For better understanding, schematics showing the lasing wavelength shift under different reaction time and different enzyme concentration are plotted in Figs.5.4d and 5.4e. The corresponding lasing spectra for both groups of experiments were recorded and summarized in Figs.5.4f and 5.4g. Initially, one can clearly observe laser emission around 540 nm; however, the lasing wavelength redshifts gradually upon enzyme reaction and eventually ceases at 580 nm. To confirm the reproducibility of such enzyme-tunable laser, the statistics of lasing wavelength from both groups were conducted in Figs.5.4h and 5.4i, respectively.

For each condition, we recorded 5 individual droplets and measured their spectral wavelengths. Our results demonstrate that the lasing wavelength for each group was consistent, which appeared at 540, 562, 571, and 580 nm, respectively. These result demonstrates that our enzyme-responsive hydrogel laser was highly reproducible and

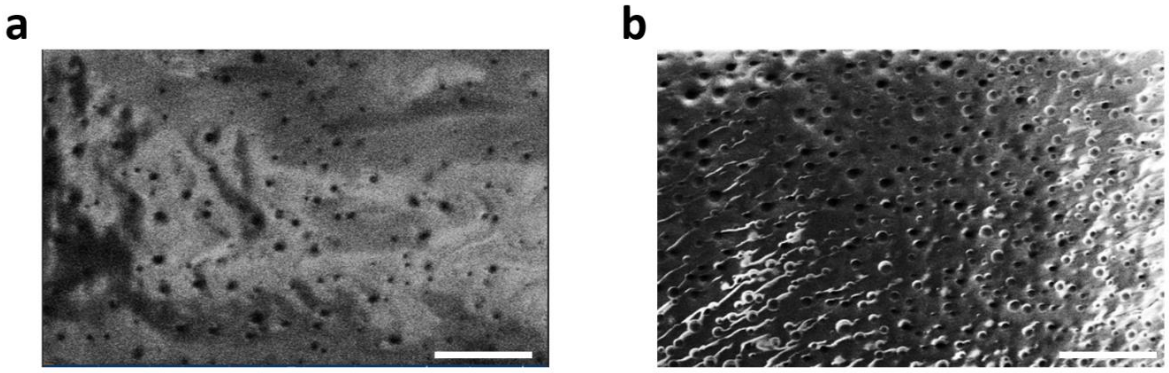

Figure 5.5 (a-b) Scanned electron microscope images of hydrogel structure tailored by 10 μg/mL and 100 μg/mL alginate lyase. Scale bar, 10μm.

controllable. To verify the influence of pump energy on wavelength changes, lasing spectra of droplets reacting with 10, 40, and 100 μg/mL alginate lyase were recorded under different pump energy densities. As we further increased the pump energy density (above threshold), the lasing wavelengths from the droplets remain stable, which indicates that the pump power contributes little to the changes of laser wavelengths.

Besides, the stability of the hydrogel droplet through multiple swell process and its lasing wavelength are also evaluated. As shown in Fig.5.7a, the diameter of hydrogel droplet remains almost the same after 8 cycles of swell. In Fig.5,7b, two samples were evaluated (40 and 100 μg/mL). It is clearly showing that after each droplets can achieve nearly same lasing wavelngth after 8 cycles of experiment, proving its stability.

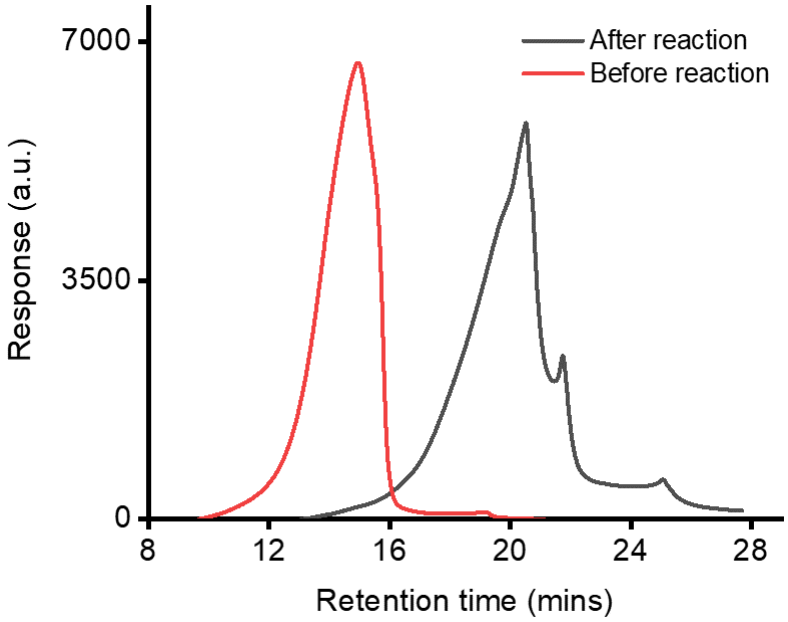

Figure 5.6 Retention time-response profile of alginate methacrylate before (red) and after (black) alginate lyase degradation. Molecular weight was calculated based on standard dextran sample. The calculated molecular weight was 3072942 g/mol before and 85467 g/mol after the reaction.

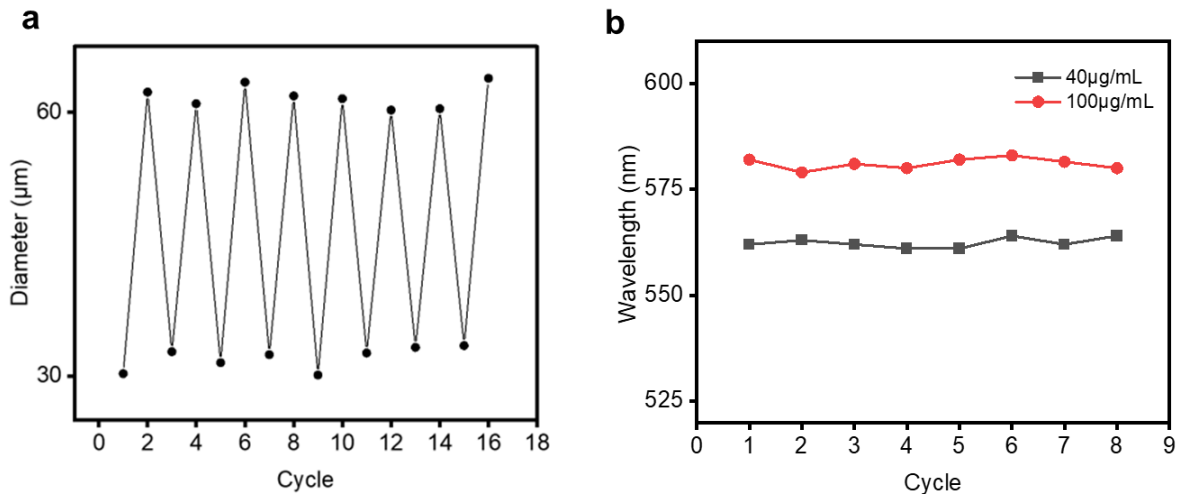

Figure 5.7 (a) Hydrogel size changes in 8 cycles of experiments. **(b)** Hydrogel lasing wavelength changes in 8 cycles of experiments.

5.2.3 Theoretical Calculation of Q-factors and Population Inversion

Before applying hydrogel laser in optical encoding, theoretical calculations were delivered to provide comprehensive insights into the mechanism of wavelength-tunable lasing. Herein, we investigated the quality factor (Q-factor) of an FP cavity encapsulated with hydrogel droplet under various swelling conditions. To mimic experimental conditions, a hydrogel droplet containing 100 μg/mL alginate lyase was selected as a representative model. Fig.5.8a shows the dynamic relation between droplet diameter and its contact angle as the humidity increases. Indeed, the droplet may continue to degrade by the enzyme and the encoded message may eventually vanish after a longer period of time. Potentially, this may be a useful tool for self-erasable message with expriration time [168, 169]. At higher humidity, a larger equivalent cavity length was obtained due to increased droplet size and contact angle, prolonging the photon lifetime and leading to a higher cavity Q-factor. The stronger optical confinement of larger hydrogel droplets can also contribute to the increase of Q-factor. Meanwhile, the 3D networks in hydrogel droplet induces a certain amount of optical scattering (Fig.5.5), which is originated from different refractive indices between hydrogel network and water. Higher water content leads to a larger droplet and in turn, decreases the density of 3D networks in a droplet, resulting in weaker scattering as

well as smaller loss and higher Q factor. To consider this issue, we introduced the imaginary part of the refractive index of a droplet to simulate the loss form spatial refractive index inhomogeneity. Details of imaginary part are provided in Methods. The corresponding models for hydrogel droplets under different swelling conditions support our theory. As presented in Fig.5.8b, the calculated electric field distributions demonstrate different extents of optical confinement when droplet swells. The Q-factor of different hydrogel droplets were extracted and plotted in Fig.5.8c, confirming that the Q-factor indeed increased during the swelling process. Details of calculation can be found in the Method section. Due to the dominance of fundamental mode (Figs.5.1c-5.1d), only the electric field distribution of the fundamental mode was taken into consideration.

According to our simulation results, it is explicit that different swelling state of hydrogel droplets corresponds to different optical Q-factors. It should be noted that the Q-factor of an optical cavity often plays a dominant role in wavelength changes, for instance, in biosensing and laser switching.[97, 170, 171] To fully investigate the relationship between lasing wavelength and different Q-factors, herein, we employed theoretical models to explain this effect. The rate equation model is one of the most well-known systems which can be applied to describe the relation between lasing threshold (lasing wavelength) and quality factor. As shown in the equation below, at the lasing threshold:

$$n_1\sigma_e(\lambda_L) = (n_T - n_1)\sigma_a(\lambda_L) + \frac{2\pi m}{\lambda_L Q_0} \tag{5.1}$$

where n_T is the total concentration of F-MA and n_1 is the concentration of F-MA in the excited state, $\sigma_e(\lambda_L)$ and $\sigma_a(\lambda_L)$ are the emission and absorption cross-sections of F-MA at the lasing wavelength (λ_L), Q_0 is the empty-cavity Q-factor, and m is the refractive index of hydrogel (m ~ 1.4 for hydrogel).

By rewriting eqn. (1), the fraction of F-MA in the excited state can be obtained:

$$\gamma_{th} = \frac{n_1}{n_T} = \frac{1}{\sigma_e(\lambda_L) + \sigma_a(\lambda_L)}\left[\sigma_a(\lambda_L) + \frac{2\pi m}{n_T \lambda_L Q_0}\right] \tag{5.2}$$

The dependence of γ_{th} on different wavelength is plotted in Fig.5.8d based on eqn. (2), in which the absorption and emission cross-sections of F-MA were measured and shown in Fig.5.9. All the Q-factors used here were based on theoretical calculation in Fig.5.8c. Note that the minimum value of γ_{th} represents required population inversion at the lasing threshold, which also corresponds to the wavelength that dominates the oscillation (predicted lasing wavelength). From Fig.5.8d, an obvious red shift from 540 nm to 578 nm was observed for γ_{th}, corresponding to a Q-factor from 3300 to 16000. After exploration of the cause for wavelength shift, the Q-factor was identified as the key factor, which could have a huge influence on lasing threshold as well. Then, we continued our work in search for the possibility of controlling the emission state of biological controlled lasing by altering pump intensity.

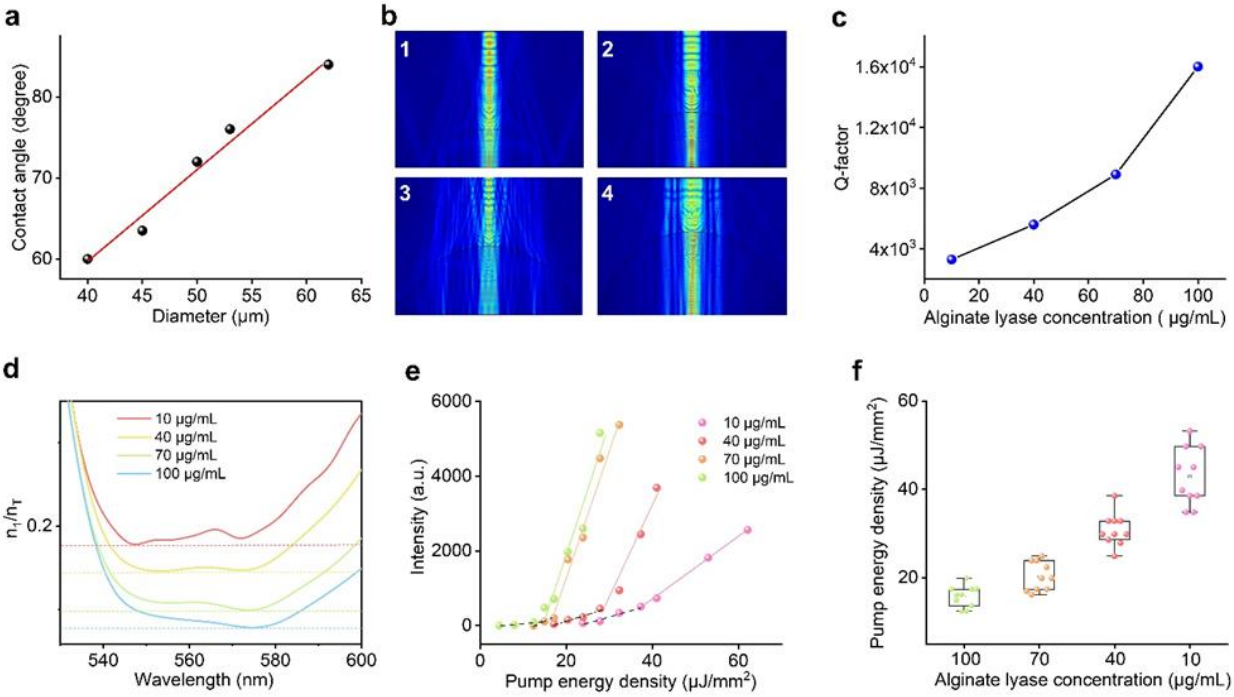

Figure 5.8. (a) Hydrogel droplet contact angle as a function of its corresponding diameter **(b)** Calculated electric field distribution of hydrogel droplets with different morphology inside FP cavity. Contact angle: (1) 65, (2) 72, (3) 78, and (4) 84 degrees. Scale bar, 20 μm **(c)** The profile of calculated Q-factor as a function of alginate lyase concentration**. (d)** Calculated required population inversion for hydrogel droplets tailored by different concentration of alginate lyase. **(e)** Spectrally integrated output intensities as a function of pump energy density from hydrogel droplets tailored by alginate lyase under respective concentrations. **(f)** Statistics of lasing threshold recorded from 10 hydrogel droplets under each enzyme concentration.

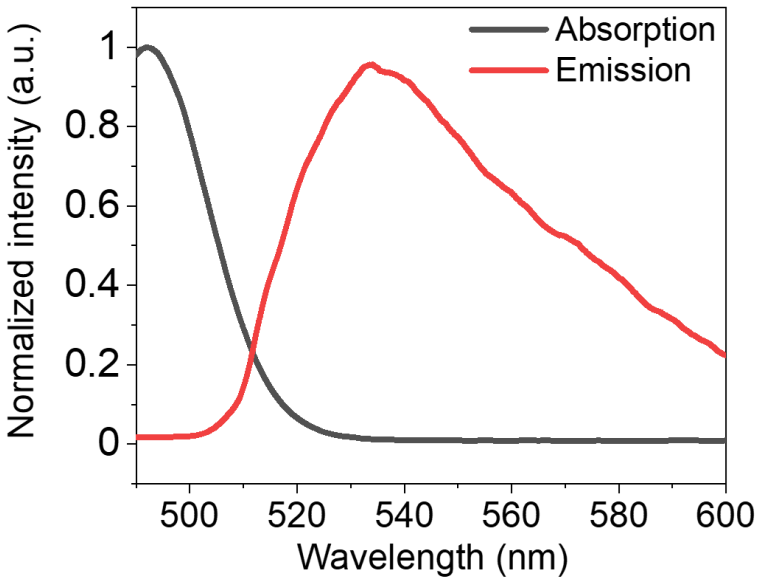

Figure 5.9 Absorption cross sections (black curve) and emission cross sections (red curve) of F-MA in hydrogel precursor from 490 nm to 600 nm.

To investigate the threshold difference, M-AAm hydrogel droplets were treated by alginate lyase with different concentrations (10, 40, 70, 100 μg/mL). The lasing thresholds were measured and plotted in Fig.5.7e. To our surprise, an obvious disparity of lasing threshold was obtained among 10, 40, and 100 μg/mL alginate lyase. However, the lasing thresholds for 70 and 100 μg/mL were very close and were not outstanding enough to serve as a distinctive label. This is likely due to the fact that lasing threshold becomes more stable under a relatively large Q-factor. To confirm the repeatability, the statistics on lasing thresholds were conducted, as shown in Fig.5.8f, respectively. The average lasing thresholds were highly distinguishable among 10, 40, and 100 μg/mL. Such results provided the foundation to control the emission state of individual hydrogel droplets through pump energies.

5.2.4 Laser Information Encoding in Digital Array

The ability to manipulate lasing wavelengths of individual enzymatic hydrogel droplets lays the foundation for optical encoding. By altering the environment humidity,

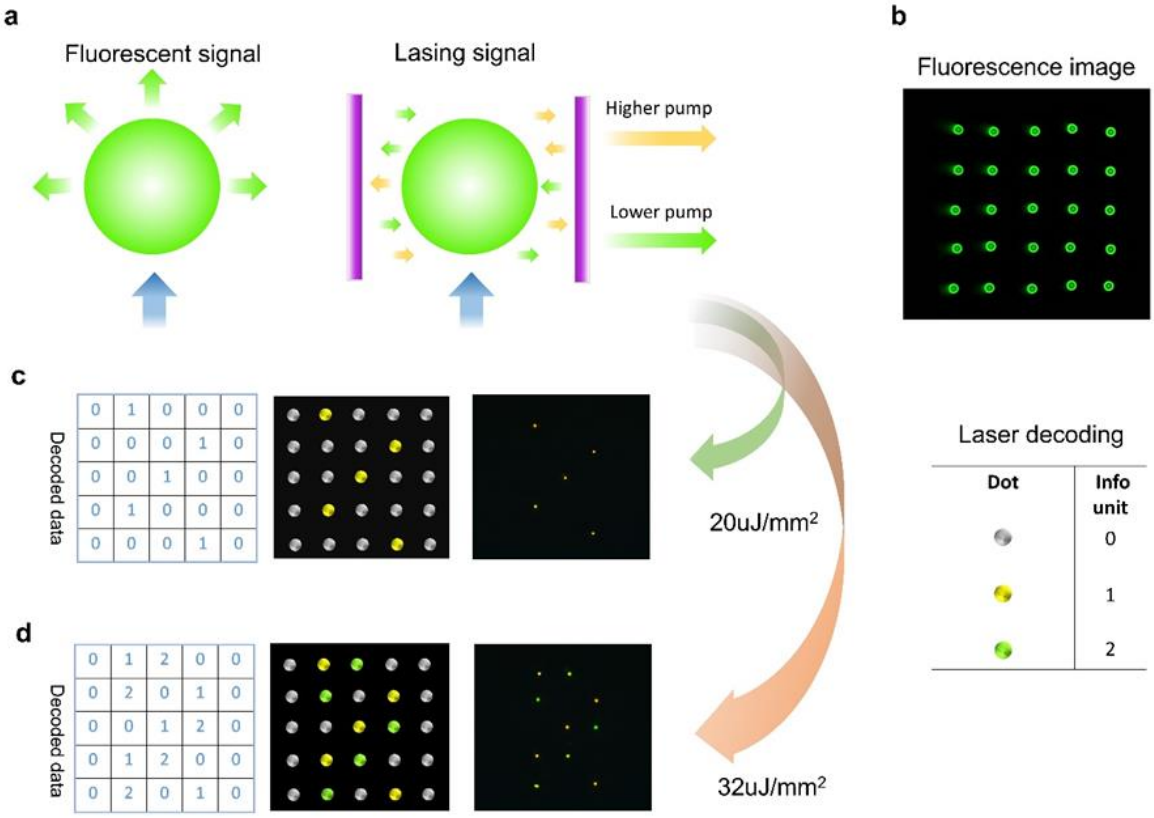

Figure 5.10 **(a)** Schematic showing the differences of lasing signal and fluorescence signal. **(b)** Fluorescence image of the printed microarray pumped by LED light. **(c-d)** Scanned lasing images of microarray under different pump energy density: **(c)** 20 μJ/mm^2 and **(d)** 32 μJ/mm^2. Righthand images**:** experimental laser emission. Center images: encoded laser data. Lefthand images: decoded data from the corresponding lasing images obtained under different pump energy densities.

the swelling ratio of droplets would change correspondingly. Here we take advantage of an inkjet printer to fabricate a microlaser array for encoding. Hydrogel droplets with different concentrations of alginate lyase (100, 40, and 10 μg/mL) were chosen to form the microarray at different spatial locations on-chip. When the environment humidity increases from 60% to 80%, each droplet possesses a distinctive threshold and lasing. Only droplets whose thresholds are lower than pump energy density could be excited while others remain dark. With various permutations of excited and dark droplets, digital information could be coded. Threshold differences between droplets could serve as additional encoding elements for higher level of information encoding. The

true information can only be extracted under the specific pump energy density. Compared with fluorescence signals, lasing signals were able to achieve different emission states corresponding to specific enzyme reactions (Fig.5.10a). As a proof-of-concept, the original 5×5 digital information was programmed into an enzyme-controlled hydrogel array.

Under LED light excitation, the contained information cannot be identified, as presented in Fig.5.10b. All the droplets emitted green emission due to the broadband of fluorescence, without being able to distinguish among different droplets under a humidity of 60%. In contrast, obvious swelling of droplets was observed in an environment with relative humidity of 80%; different laser emission wavelengths could be decrypted under a pulsed laser excitation (ex: 488 nm). Under a pump energy density of 20 μJ/mm^2, the scanned image of laser array is shown in Fig.5.10c. Only the droplets with 100 μg/mL alginate lyase were excited and emitted yellow laser emission. When the pump energy density increased to 32 μJ/mm^2, droplets with 40 μg/mL alginate lyase were excited and emitted green laser emissions (shown in Fig.5.10d). Here we define green emission, yellow emission, and dark droplets as digital number 2, 1, 0 (inset Table), providing a total encoding capacity of 325. The decoded message could be identified under correct pump energy density as shown in Figs.5.10c and 5.10d. Alternatively, each row could also be encoded into 5-digit information with a capacity of 243 labels. Following such an encoding rule, the obtained image can be reversed to the original digital message.

5.2.5 Lasing Encoding Altered by Spatial Arrangement

By altering the spatial arrangement of hydrogel droplets with an inkjet printer, various patterns can be programmed besides a digital array (Fig.5.11a). To demonstrate the scalability, “NTU” array was fabricated containing two different hydrogel droplets (alginate lyase: 100 and 10 μg/mL). Fig.5.11b shows the photo of printed NTU array under normal LED excitation.

The scanned images of the array under LED are shown in Fig.5.11c. One can clearly visualize the NTU pattern with green fluorescence emission before swelling. In

contrast, when the array was excited under a pulsed laser with 20 μJ/mm^2 and 45 μJ/mm^2 (under humidity of 80%), different emission patterns will emerge (Fig.5.11d). For instance, a false information “1 1 1” was observed under 20 μJ/mm^2. However, the true information “NTU” will appear eventually as the pump energy increased to 45 μJ/mm^2. To demonstrate higher-security encoding, an 11×7 microarray was fabricated by printing three different structured hydrogel droplets (alginate lyase: 100, 40, and 10 μg/mL). As shown in Fig.5.11e, the array showed meaningless information under a normal LED light.

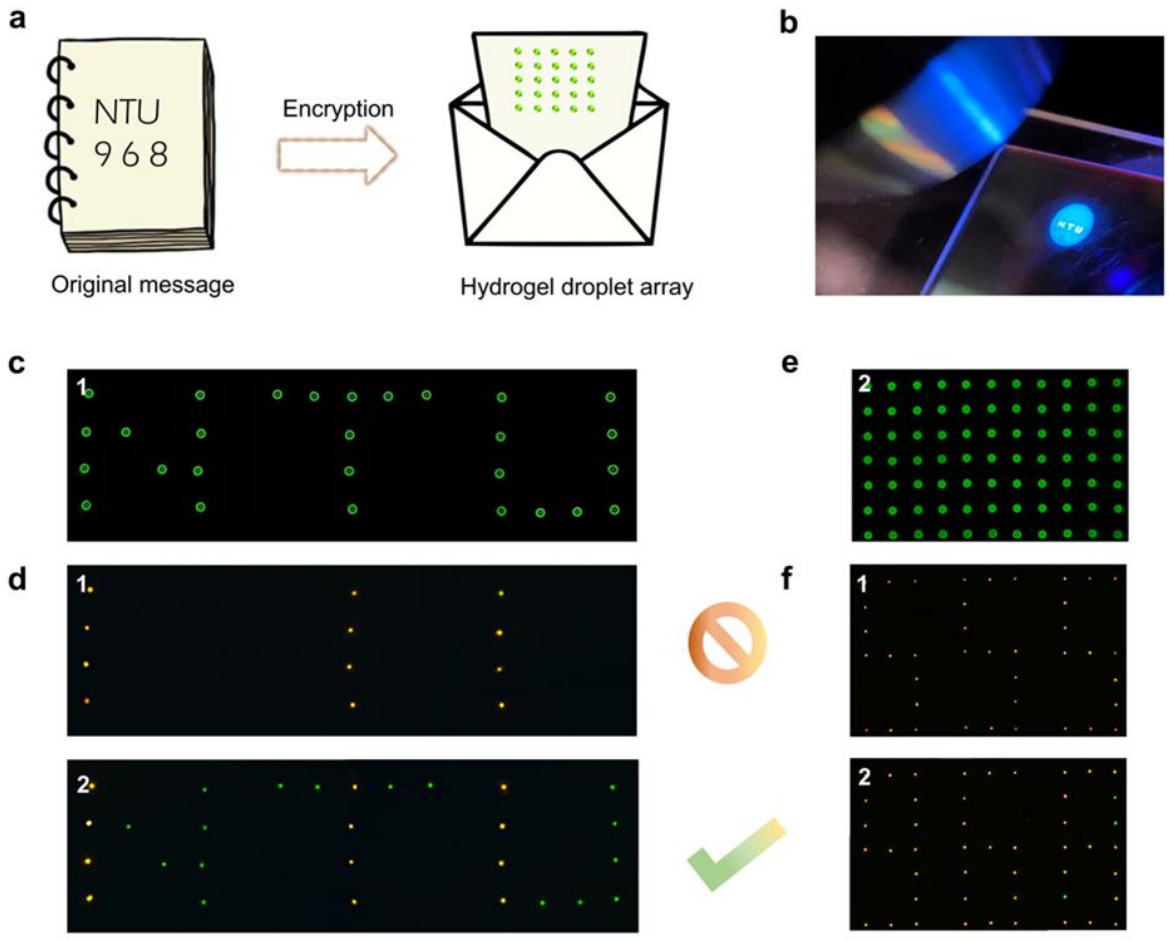

Figure 5.11 **(a)** Schematic showing the concept of information encoding using hydrogel array **(b)** The photo of NTU array illuminated under LED pump. **(c)** Fluorescence image of NTU array under LED pump. **(d)** Scanned lasing images of NTU droplets array under different pump energy density. (1) 20 μJ/mm^2; (2) 45 μJ/mm^2. **(e)** Fluorescence image of 11×7 droplets array under LED pump. **(f)** Scanned lasing images of 11×7 droplets under different pump. (1) 20 μJ/mm^2; (2) 32 μJ/mm^2.

Nevertheless, the true information“9 6 8” can only be extracted under a pump energy density of 32 μJ/mm^2, while the false information “5 5 5” will be acquired under lower pump intensities, such as 20 μJ/mm^2 (Fig.5.11f). To be noted, the droplets containing 10 μg/mL served as background here to help clarify the appearance of digital numbers.

5.2.6 Hyperspectral Lasing Images for Information Security

Lastly, we explored the responsiveness of hydrogel droplets inside an aqueous environment. The principle of acquiring hyperspectral images of laser modes is shown in Fig.5.12a. A 2×2 hydrogel array was printed, and its corresponding lasing image inside air is shown in Fig.5.12b. After immersing the FP cavity with buffer solution, we surprisingly found the laser mode of each droplet reached higher complexity rather than the fundamental mode (Fig.5.12b). Furthermore, Rhodamine-B (RhB) was added to the solution to investigate how laser mode would respond to external chemical stimuli inside an aqueous solution. To our surprise, multicolor laser mode was observed on each droplet after adding RhB (Fig.5.12b), which is the result of Förster resonance energy transfer (FRET). To better illustrate the composition of multicolor modes, the hyperspectral images of three droplets were recorded and shown in Figs.5.12c to 5.12e. The left-hand image shows the integrated laser modes without splitting respective wavelengths. Although the integrated laser modes were quite similar, the detailed differences on different laser modes can be extracted through hyperspectral images, as shown on the right-hand images. Such feature-rich hyperspectral images can be regarded as a highly distinctive pattern for information security. For example, in Fig.5.12c the laser modes can be identified as Ince-Gaussian (IG) 01 and Laguerre-Gaussian (LG) 04. By extracting the order number of laser modes and arranging them corresponding to wavelengths, a digital code 010104010401040404 can be generated. Due to the different responsiveness to external environment, the generated laser code could vary for different external conditions. Meanwhile, the diversity of laser modes, including wavelength and order number could have huge potential in higher-level security methods such as physical

unclonable functions.

Looking into the past decade, a plethora of optical encryption and encoding technologies have been developed, each with its own pros and cons. Optical signals can be roughly divided into two mainstreams, non-luminescent and luminescent signals. Increasing the coding capacity through multiplexed color is one of the most common and straightforward method. For non-luminescent signals, holography is one of the most well known methods to date, which typically relies on the phase modulation of light. Conventional holograms lack the ability to provide vivid and multiplexed color, therefore metasurface hologram have overcome this issue by providing full color messages through the design of dielectric nanostructures[172]. Indeed, metasurfaces formed by nanostructures are well known for their ability to control electromagnetic waves; they can realize either two-bit or multi-bit coding by designing coding elements with different reflection phases (or transmission). Various functionalities could be designed through integration, leading to switchable encoding methods; whereas the fabrication is usually cost-intensive, time-consuming, and challenging for mass production. In contrast, most luminescent signals can be easily fabricated through inkjet printing technology, which makes it cost-effective, time-efficient, and mass-productive; however, it also suffers from broad emission bands. As such, laser emission with narrow linewidth seems to be a promising candidate for its sharp wavelengths and strong intensity. Although the detection method relies on a pump laser, which is indeed a disadvantage, we believe such technical issues may be overcome in the future. Most importantly, laser emissions can provide additional degrees of dimension for encryption or encoding. For instance, the spatial profiles, laser mode orders, wavelengths, and even optical angular momentum could all be considered to form high information capacity and security.

Finally, we would like to mention that the proposed strategy in this study is similar to that of printing luminescent materials. By introducing hydrogel as the host material, various types of biomolecules and reactions can be easily integrated into this system. The preparation and fabrication are straightforward and can be done in a few minutes

to perform a massive dimension of the pattern. To facilitate this technology, the pre-calibration and quantification are very important to reach a fully programmable condition. Once calibrated and optimized, each solution can be used as ink and printed out on a chip directly. The spacers can also be fixed and printed directly as well, without further equipment. We would especially like to point out that the similar concept can be extended to other types of hydrogel polymers and most luminescent dyes or fluorophores (not limited to the emission band in this study). The concept is not only suitable for enzyme reactions but also can be applied in many scenarios, such as DNA derivatives. Manipulating optical properties by biochemical reactions can be realized

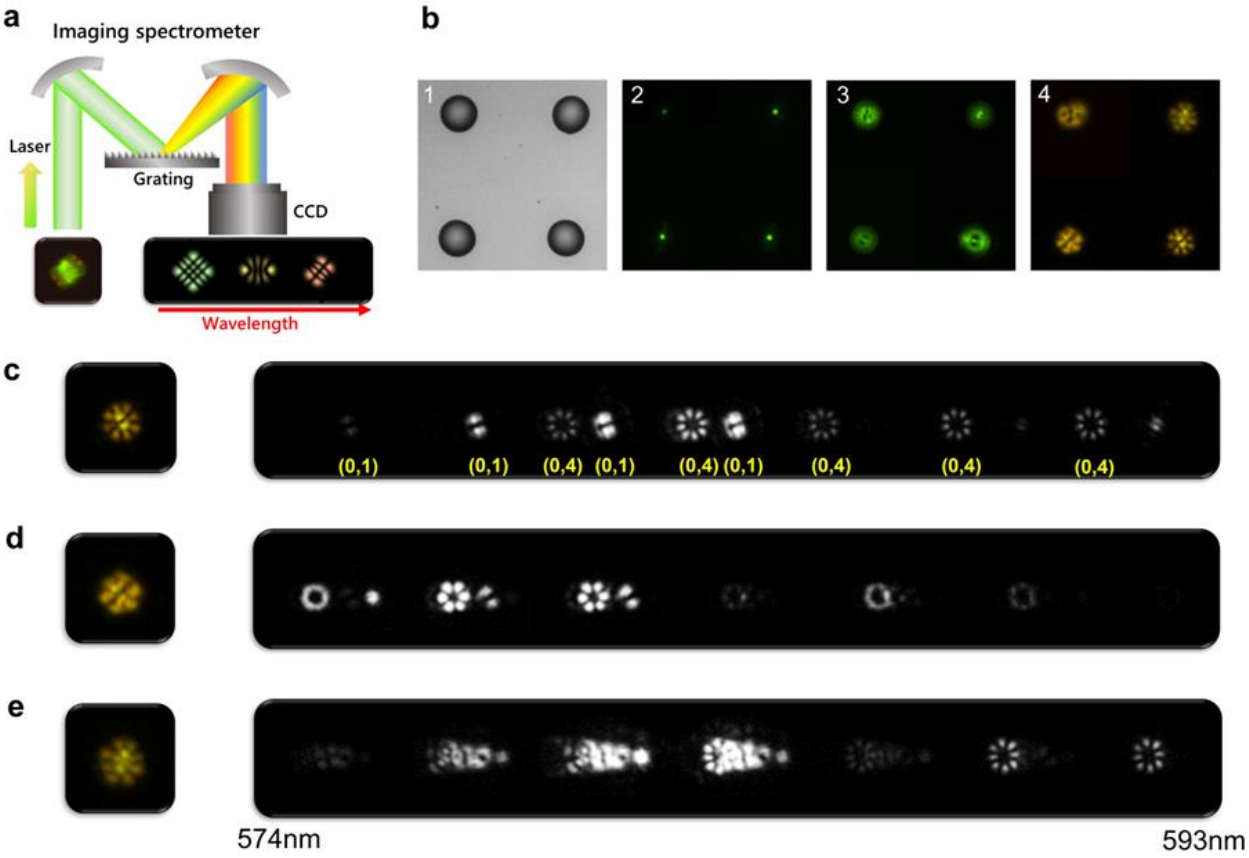

Figure 5.12 (a) Schematic showing the setup of obtaining hyperspectral images[3] **(b)** 1: Bright field image of hydrogel droplet array (d=40 µm). 2-4: Scanned lasing images of hydrogel array in air, Tris buffer, and RhB solution. **(c-e)** Laser modes extracted from three individual hydrogel droplets with introdution of RhB solution. The lefthand image shows the superimposed laser modes. The righthand shows the corresponding hyperspectral images from 574 nm to 593 nm.

through multiple combinations of biochemical reactions, including catalyzation, hydrolysis, and isomerization, which provides flexible and available encoding design for different circumstances. By increasing the complexity or quantity of reactions included, high-order information security methods can be realized as well. Compared with conventional materials or artificial materials, such an approach may provide insight to achieve encoding or anticounterfeiting through sustainable biomaterials and simple reactions. However, the accuracy of information control is an uncertain problem as it is still in its infant stage. The randomness of biological and chemical reactions can be a problem for controllability, which needs to be addressed; however, on the other side, it may provide higher complexity and security for the targeted message.

5.3 Conclusion

Biological tunable laser can be a rational alternative solution for encoding by integrating active biological materials and conventional photonics. In the current study, we developed a biological encoded laser and demonstrated its potential applications in information encoding and encryption. Enzyme-based reactions were employed as the switch to control the hydrogel inner structure, which in turn changes the cavity geometry and lasing emission. Our results revealed that the swelling process of droplets leads to a redshift in lasing wavelength as a result of increased Q-factors. Such wavelength shift could be fully controlled by applying different pump intensities. One can control the desired laser emission wavelength over a wide range of spectra by tuning the swelling ratio in biological driven hydrogel droplets. Finally, various forms of photonic information were fabricated through inkjet-printer, including digital array, text information, and digital numbers for optical encoding. We also showcased the stimuli-responsivity of laser barcode, which could serve as a security label to detect environmental changes.

We envision that by exploiting the complexity and self-recognition of DNA sequences or amino acids, laser light could be fully manipulated and programmed in the near future. Tunable optical devices can also be responsive to different stimuli. However, there are also several challenges. First, to make use of the high capacity

and complexity, the readout of optical signals must be equipped with a high spectral or spatial resolution machine. The coupling efficiency from the molecular scale to the macro scale is also a critical issue that needs to be engineered. Secondly, since the biological molecules or hydrogels are chemically active, they can undergo degradation reactions, including oxiation or hydrolysis, leading to instability and poor reproducibility. Finally, biological materials are generally more expensive than artificial materials nowadays. The search for mass-producible and abundant resources for active optoelectronic applications remains an important step in the future.

Chapter 6: Hydrogel Microlaser Anti-counterfeiting Labels Utilizing 3D Network Randomness

In Chapter 5, we successfully employed enzyme reactions to manipulate the internal structure of the hydrogel and control the laser emission. In the current chapter, our objective is to investigate the feasibility of utilizing the hydrogel itself, independent of external factors, as a potential strategy for implementing anti-counterfeiting measures.

As the world becomes increasingly digitized and interconnected, the challenges related to fraud and security have also escalated exponentially.[173-176] Counterfeiting, a multibillion-dollar global challenge, poses significant threats to a wide range of sectors, from luxury goods to pharmaceuticals, undermining economic growth and endangering public health and safety. Consequently, the need for efficient and reliable anti-counterfeiting technologies has never been more pressing. Optical anti-counterfeiting, a cutting-edge response to this urgent need, has emerged as a pivotal technology offering a sophisticated, yet unobtrusive, solution[175, 177-180]. Optical anti-counterfeiting primarily exploits the properties of light and its interactions with matter to create features or tags that are challenging to replicate. This approach leverages a range of technologies, including holography[181], diffractive optical elements (DOEs)[182], optical variable devices (OVDs)[183], quantum dots[184], and photonic crystals[185]. The significant advantage of these technologies is that they can provide overt, covert, and forensic levels of security features, making them extremely versatile in addressing a broad spectrum of counterfeiting issues. Among these strategies, laser anti-counterfeiting has attracted tremendous attention of researchers. Compared with the conventional broad band photoluminescent methods, the employment of laser emission has been increasingly recognized as a formidable mechanism for optical anti-counterfeiting[2, 7, 133]. This innovative approach introduces novel coding elements by eliciting emission spectra of rich features, which are contingent upon alterations in gain materials and cavity geometrics. Numerous

lasing configurations, scalable from micro to nano levels, has been exhaustively investigated and successfully manifested for such purposes, which include, but are not limited to, whispering-gallery mode lasers and random lasers, thereby broadening the horizons of this emergent field. Meanwhile, the remarkable sensitivity inherent in laser makes it as a potent and efficient medium to conveyance of information encoded within the intrinsic structure of materials. It amplifies subtle changes via optical oscillations, thus providing a conduit for the control of the complexity and volume of information carried by laser emissions through the manipulation of the material structure.

Recently, hydrogels have risen to prominence as an exceptional materials with multiple potential applications in photonics due to their light-guiding properties with chemically reactive network. Endowed by the hydrophilic group in the polymer chains, hydrogel possesses strong water storage capacity and are well-known for their high tunability. Taking advantage of the functional groups on the side chain, hydrogels also demonstrated a higher functionality by responding to various external stimuli, such as pH, temperature, humidity, and specific chemical reactions[68, 71, 156, 160]. While the exceptional biochemical performance of hydrogels is well-recognized, the intricate nature of its three-dimensional polymer network simultaneously confers upon it a potentialy large data storage capacity. By selecting the initiator during polymerization, significant variations can be induced in the hydrogel network structure, affecting parameters such as homogeneity of the network, network density, and interchain molecular distances[186-189]. These modifications open up a substantial range of possibilities for the application of hydrogels in anti-counterfeiting techniques, adding another dimension to their already substantial versatility.

Motivated by the inherent sensitivity of laser technology and the intricate complexity of hydrogel networks, we have designed a laser anti-counterfeiting strategy which harnesses the randomness embedded in the hydrogel network, introduced via free radical polymerization. The Förster Resonance Energy Transfer (FRET) mechanism has been selected for its heightened sensitivity to the spatial positioning

of dye pairs, enabling it to encapsulate the information regarding the random interchain molecular distances within the hydrogel. Figs.6.1a and 6.1b delineate the distinct contrasts between free radical polymerization and step-growth polymerization. As depicted in Fig.6.1a, the hydrogel network structure showcases marked heterogeneity, with discernible disparities in network density across various locations within the hydrogel. Conversely, the network structure assumes a more uniform character during step-growth polymerization.

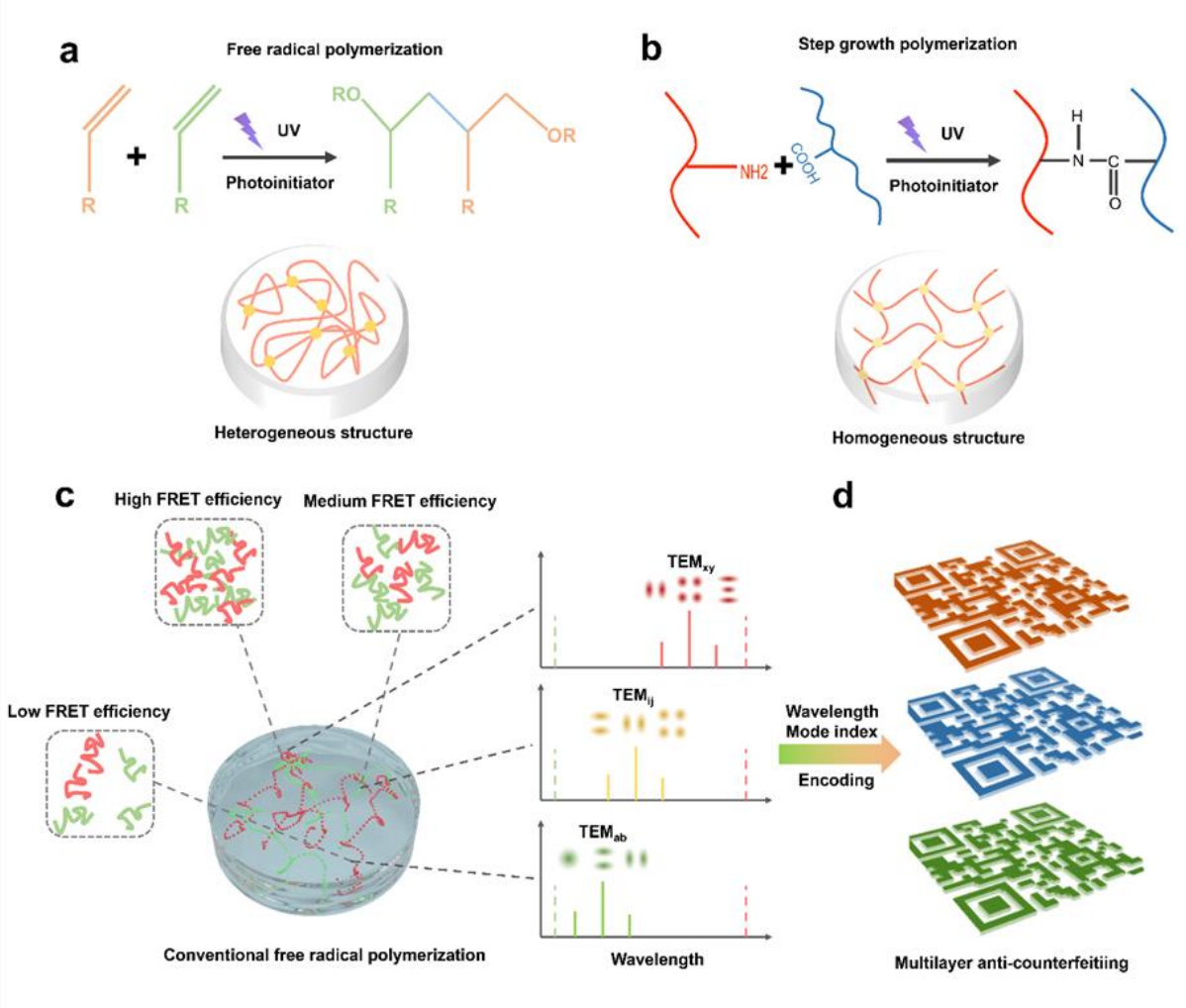

Figure 6.1 (a-b) Schematic showing the process of **(a)** Free radical polymerization and **(b)** Step growth polymerization. **(c)** Schematics diagram illustrating the spatial differentce of hydrogel 3D network density which results in different lasing emission. **(d)** Transferring the laser spectrum and laser modes for multilayer anti-counterfeiting codes

By incorporating an element of randomness through free radical polymerization, the molecular distances between FRET pairs, conjugated onto the hydrogel chains, are randomly distributed across different areas of the hydrogel. This results in differential FRET efficiencies and a diversity of lasing wavelengths in the spectral domain, as represented in Fig.6.1c. Finally, as a proof of concept, we have demonstrated the use of such a hydrogel for generating anti-counterfeiting codes, leveraging information derived from both lasing wavelength and laser modes indices, corresponding to the laser spectrum (Fig.6.1d). These findings may stimulate novel insights into the systematic design of laser anti-counterfeiting methodologies, exploiting performance-based, structurally tunable materials.

6.1 Experimental Methods

6.1.1 Materials

For hydrogel, Poly(N-isopropylacrylamide) (Sigma Aldrich #535311) was selected as the monomer. N,N′-Methylenebis(acrylamide) (Sigma #146072) as crosslinker to form 3D structure, 2-Hydroxy-4′-(2-hydroxyethoxy)-2-methylpropiophenone (Sigma # 410896) as photoinitiator to trigger polymerization. For dye used in this work, Fluorescein O-methacrylate (Sigma Aldrich #568864) served as donor and we chose Acryloxyethyl thiocarbamoyl rhodamine B (Sigma Aldrich # 908665) as the donor.

6.1.2 Microdisk Fabrication

For PNIPAM hydrogel microdisk, 0.3 g Poly(N-isopropylacrylamide) and 0.015 g Bis-AA were dissolved in 500 μL Tris buffer to prepare the precursor solution. Furthermore, 25 mg photoinitiator was added into the solution to trigger polymerization after UV curing (Panasonic #ANUJ3500). Next, 2 mg F-MA were added into the solution as gain material. Finally, the prepared solution was added into a modified office printer and printed on the dielectric mirror. After the completion of printing, a spacer of 9.9 μm was used as spacer to fabricate the FP cavity. After being sandwiched between two mirrors, the printed microdroplets were compressed to form microdisks whose height was equal to the cavity length.

6.1.3 Optical Setup

An optical microscopic system (Nikon Ni2), equipped with a 10X 0.3 NA objective, was utilized for both pumping the droplet array and collecting the emitted light. The pump source comprised of a pulsed ns-laser (EKSPLA NT230) combined with an optical parametric oscillator (repetition rate: 50 Hz; pulse duration: 5 ns; pulse energy: 5 mJ). In correspondence with the specific absorption wavelength of the fluorophores, the pump laser was fine-tuned to an excitation wavelength of 480 nm to match the excitation requirements of F-MA. The laser beam diameter at the focal plane of the objective was approximately 40 μm. The gathered light was directed towards a charge-coupled device (CCD) camera or an imaging spectrometer (Andor Kymera 328i and Newton 970 EMCCD). When measuring color images, which includes laser and fluorescence visuals, a color CCD (DS-Fi3, Nikon) was affixed to the microscope system.

6.2 Results and Discussion

6.2.1 Lasing Performance Calibration for FRET Laser Generated from Hydrogel

To commence, we first set out to calibrate the lasing performance of a hydrogel laser generated from Förster Resonance Energy Transfer (FRET) pairs. In this system, Fluorescein-o-methyacrylate (F-MA) served as the donor and Acryloxyethyl thiocarbamoyl rhodamine B (Rhodamine-M) functioned as the acceptor. It should be underscored that the functional group attached to the fluorophore acted as a bridge linking the dye group and the hydrogel chain, thereby enabling the fluorophore to be responsive to changes in the hydrogel interchain distance. The fundamental principle of FRET, rooted in energy-level interactions, is depicted in Fig.6.2a. FRET encapsulates a process of non-radiative energy transfer between two chromophores, whereby the donor molecule, having absorbed a photon to reach an elevated energy state, transfers this energy to the acceptor molecule without photon emission. This energy transfer is intrinsically tied to the distance and relative orientation between

donor and acceptor molecules, which establishes FRET as a potent tool for exploring molecular interactions and conformational changes. In order to scrutinize the influence of differing FRET efficiencies on lasing performance, we prepared three distinct solutions, each with varying F-MA and Rhodamine-M ratios. Herein, the F-MA concentration was held constant at 2 mM while the Rhodamine-M concentration was adjusted to 0.005, 0.01, and 0.05 mM. In order to generate a laser signal, the solution was interposed within a Fabry–Pérot (FP) cavity formed by two highly reflective mirrors. The outcomes are delineated in Fig.6.2b, where distinct lasing signals across the spectrum are evident. As the donor-acceptor ratio increases, a red shift extending from 521 nm to 618 nm was observed.

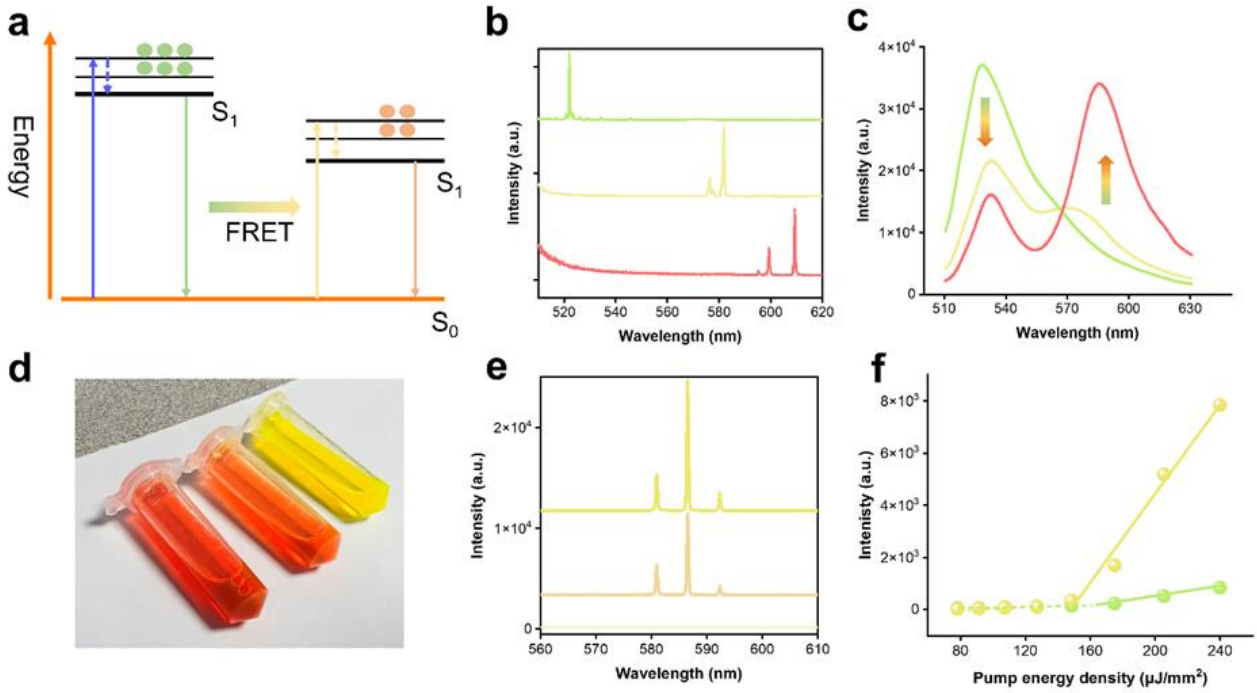

Figure 6.2 **(a)** Schematic showing the non-radiative energy transfer process of FRET. **(b)** Lasing spectra recorded from three different solution with different donor-acceptor ratio (2:0.005; 2:0.01; 2:0.05). **(c)** Fluorescence emission spectra of three different solution mentioned before. **(d)** Photos of solution with different FRET efficiency. **(e)** Lasing spectra of solution with 2:0.01 donor-acceptor ratio under different pump intensity. **(f)** Spectrally integrated output intensities as a function of pump energy density from solution with 2:0.01 ratio and 2:0.005 ratio, respectively.

Fluorescence emission spectra for the three solution variants were recorded (Fig.6.2c), showcasing a pronounced and continuous decline in the F-MA peak and a corresponding increase in the Rhodamine-M peak as the donor-acceptor ratio diminished. This affirmed our hypothesis that FRET lasing signals can be directly manipulated by adjusting FRET efficiency. Photographic evidence of the three solutions (Fig.6.2d) vividly demonstrates a distinct change in absorption due to variations in the dye pair ratios. Having successfully produced a lasing signal from FRET pairs within the FP cavity, we proceeded to examine the impact of FRET ratios on the laser threshold to gain deeper insights into its characteristics. The lasing spectra under various pump intensities for a 2 mM:0.01 mM solution are shown in Fig.6.2e. The spectrally integrated output intensities from two different FRET efficiencies (2:0.005 and 2:0.01) were assessed under different pump intensities, and distinct thresholds of 142 μJ/mm^2 and 163 μJ/mm^2 were discerned respectively. This serves to substantiate our assertion that an elevated FRET efficiency can result in a lower threshold lasing signal.

6.2.2 Randomness of Hydrogel FRET Lasing Signal and Theoretical Calculation of FRET

Upon calibrating the performance of the FRET laser in solution, we proceeded to incorporate the FRET pairs within the hydrogel. As previously discussed, the functional group attached to the fluorophores aids in affixing the fluorophores to the hydrogel chains. This is a notable contrast to dye groups in solution, which undergo random Brownian motion and lack a fixed distance; in this context, the distance between FRET pairs can be wholly dependent on the interchain distance within the hydrogel. As illustrated in Fig.6.3a, we anticipated that the random structure introduced by free radical polymerization could lead to variations in the spatial density of the hydrogel network, thereby producing random interchain distances. Once FRET dye molecules are mounted on these chains, such variations can be manifested in the form of diverse lasing wavelengths. A redshift should be observable if the pump location is transitioned from an area of lower hydrogel network density to a region of higher density, owing to

the decreased interchain distance and increased FRET efficiency. Prior to validating our hypothesis using lasing signals, we initially recorded the fluorescence emission spectra from various locations on a fabricated hydrogel disk, the results of which are displayed in Fig.6.3b. The varied intensities of the F-MA peaks and Rhodamine-M peaks unequivocally indicate that the FRET efficiencies at these five locations differ substantially from each other, further confirming that the randomness introduced by free radical polymerization impacts FRET efficiency. To better visualize the randomness of interchain distance, we decided to theoretically calculate the distance based on Förster equation:

$$E = \frac{1}{1+\frac{R}{R_0{}^6}} = 1 - \frac{F_{DA}}{F_D} \tag{6.4}$$

where R_0 is the Förster distance and FRET pairs, R is the distance between fluorophores, F_{DA} is the fluorescence intensity of donor with the presence of acceptor and F_D is the fluorescence intensity of donor without acceptor. The Förster distance R_0 can be calculated using the following equation[190]:

$$R_0 = \left[8.8\times 10^{23}\cdot \kappa^2 \cdot n^4 \cdot QY_D \cdot J(\lambda)\right]^{1/6} \tag{6.5}$$

where κ^2 is dipole orientation factor which is 2/3 here for randomly oriented donors and acceptors, n is refractive index, QY_D is the quantum yield of F-MA which is 0.97 here, and $J(\lambda)$ is the spectral overlap integral of donors and acceptor.

Following the calculations, a Förster distance of 4.3 nm for the FRET pair of F-MA and Rhodamine-M was obtained. With this distance (R_0) in mind, the relationship between molecular distance and FRET efficiency for F-MA and Rhodamine-M can be depicted by the curve presented in Fig.6.3c. Utilizing this curve, theoretical values of interchain distance at each recorded location could be computed after extracting the FRET efficiency from the fluorescence spectra. The results, shown in Fig.6.3d, indicate distances at each location of 4.9, 5.1, 5.4, 5.6, and 6.0 nm, corresponding to FRET efficiencies from highest to lowest. These calculations not only facilitate quantification of the 3D network interchain distances but also aid in visualizing the randomness

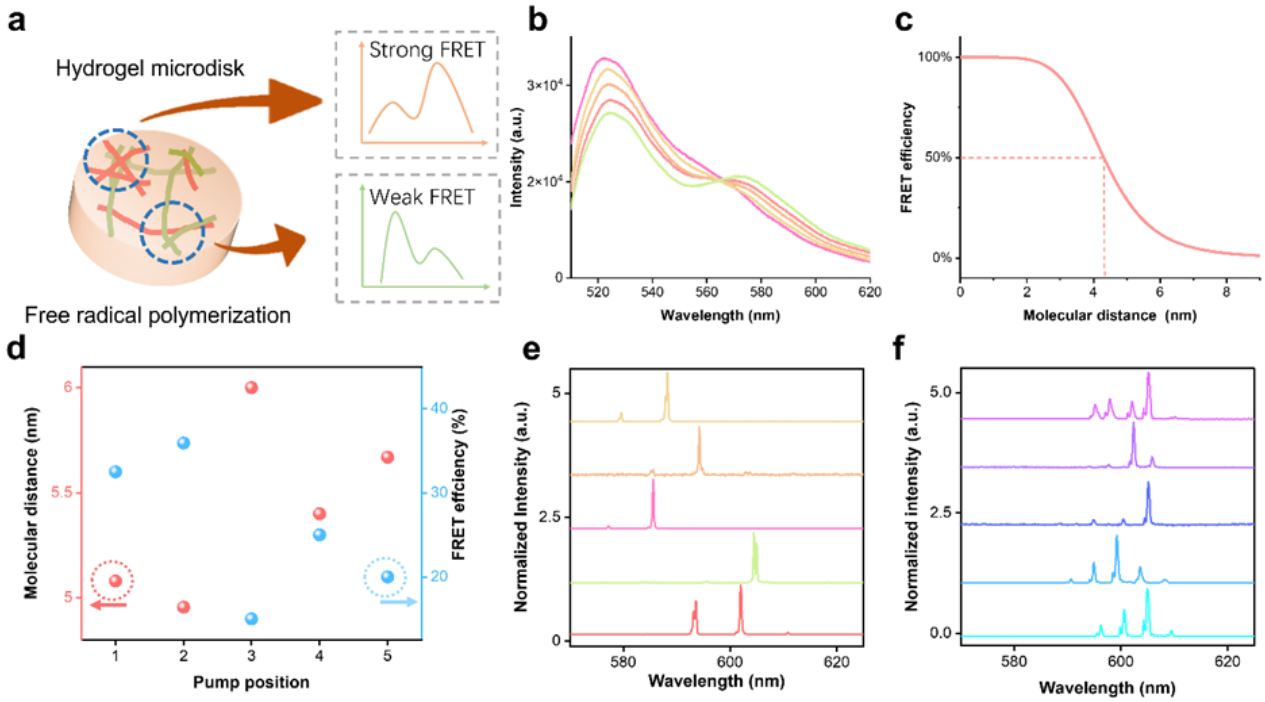

Figure 6.3 (a) Schematic showing the different FRET efficiency resulted from different network density introduced by free radical polymerization. **(b)** Fluorescence spectra recorded from different location of the hydrogel microdisk. **(c)** Relation curve of FRET efficiency corresponding to molecular distance with R_0 set to 4.3 nm. **(d)** Calculated molecular distances based on FRET efficiency extracted from fluorescence spectra. **(e)** Lasing spectra recorded from different location from the hydrogel microdisk. **(f)** Lasing spectra recorded from different from the hydrogel microdisk encapsulated a much higher FRET ratio dye pairs (2:0.01).

introduced by the free radical polymerization process. Finally, the lasing spectra for each point were recorded, as shown in Fig.6.3e, where it can be seen that the lasing signals occur at distinct wavelengths. In comparison, another experiment employing a higher F-MA Rhodamine-M ratio was conducted, in which no significant lasing wavelength was observed in the spectra (Fig.6.3f). This observation corroborates that the wavelength differences resulted from varying network density and interchain distances, validating that such randomness can be reflected by lasing signals and providing the foundation for utilizing such a microdisk to generate a vast volume of random data for information security.

6.2.3 Generating Anti-counterfeiting Code Using Hydrogel FRET Lasing Signal

Lastly, we exploited the randomness of the hydrogel network density and the FRET laser's sensitivity to molecular distances to generate anti-counterfeiting codes. An array of hydrogel microdisks was fabricated for this purpose (Fig.6.4a). For each microdisk, the lasing spectra were recorded from four distinct locations. To ensure complete independence of the excited locations, the area of the microdisk was fabricated significantly larger than the laser pump light (150 μm vs. 30 μm), with the selected locations separated by at least 70 μm from center to center. Besides the lasing wavelength, the laser modes derived from hyperspectral images also presented a significant and intriguing dimension. The complexity of these laser modes, in terms of their modality and form, demonstrates vast potential in the domain of information security. Consequently, we recorded both the longitudinal modes from the lasing spectra and the transverse modes from the hyperspectral images to generate multi-dimensional codes. The coding rule is illustrated in Fig.6.4b. Given that the transverse mode contributes two mode indices, two axes can be established based on this factor. Corresponding longitudinal modes are considered an additional factor determining the color of each square. If the longitudinal modes fall between 580-590 nm, the square is filled green, with blue and red representing longitudinal modes between 590-600 nm and 600-610 nm, respectively. An overlap rule, considering the possibility of identical mode indices, was also established and is depicted in Fig.6.5b. As a proof of concept, we recorded the lasing spectra from four distinct locations on a hydrogel microdisk, with the results shown in Figs.6.4c and 6.4e. As shown in Fig.6.5c, several longitudinal modes were observed, and their corresponding transverse modes were also identified. Following the code rule, the spectrum was translated into a code based on different longitudinal mode wavelengths, as shown in Fig.6.5d. After the overlapping process, a code representing the spectrum from this point was generated. The same process was applied to the spectrum from another location, resulting in an additional code (Fig.6.4f). By integrating the codes generated from four distinct locations into a single

one, a more complex anti-counterfeiting code can be achieved (Fig.6.4g). Considering that each square can have a maximum of 7 conditions and that the color occupancy from square to square is independent, a data capacity of 7^{64} can be achieved based on a single microdisk. With the integration of an array of microdisks, an even larger data capacity can be easily obtained.

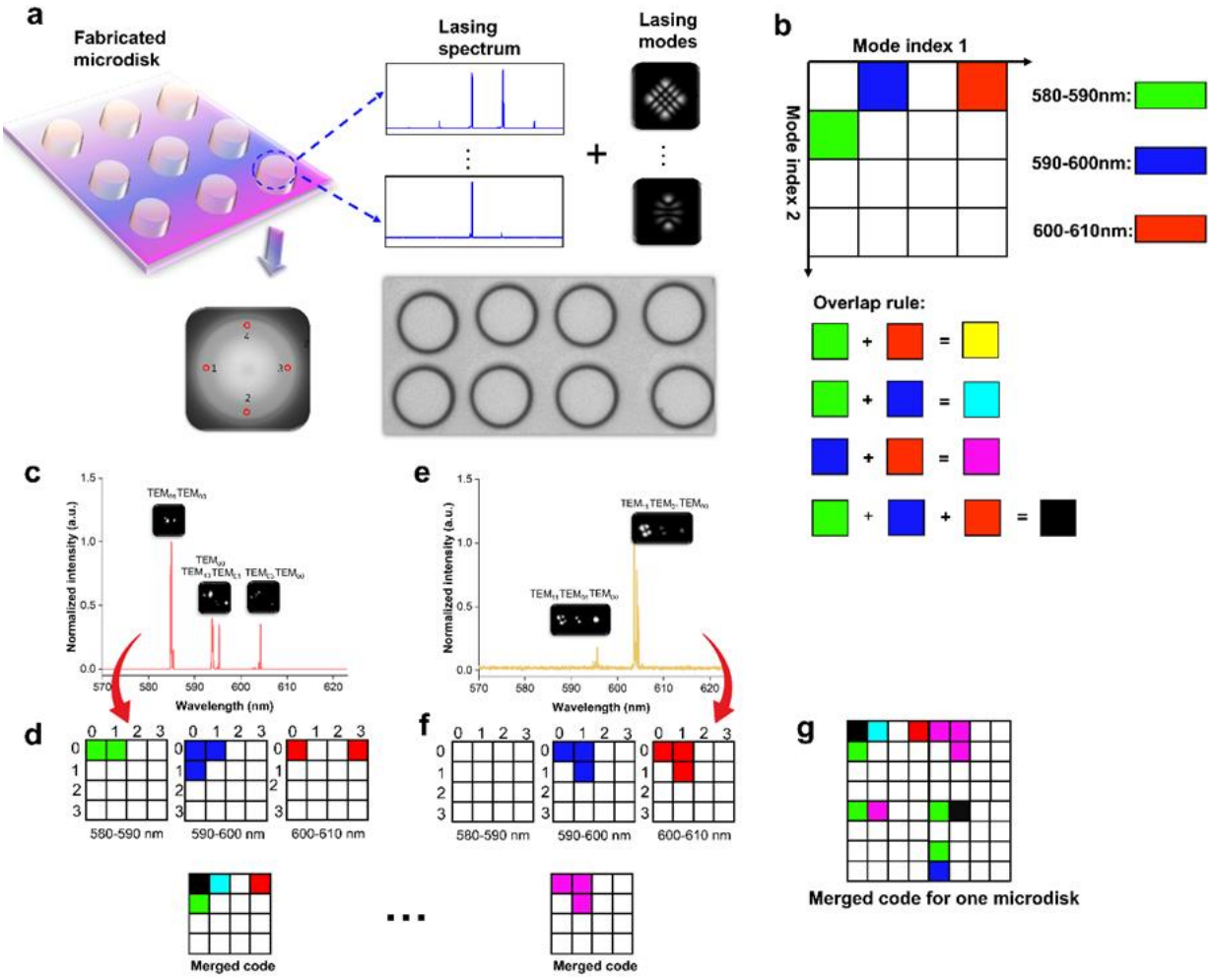

Figure 6.4 (a) Schematics showing how to use the fabricated microdisk to complete anti-counterfeiting code generation. **(b)** Coding rule and overlapping rule. **(c)** Lasing spectrum recorded from one location of microdisk and its corresponding transverse mode. **(d)** Separated code based on wavelength and merged code. **(e)** Lasing spectrum recorded from a distinct location of microdisk and its corresponding transverse mode. **(d)** Separated code based on wavelength and merged code. (g) The final code integrated by four positions.

6.3 Conclusions

In conclusion, our research pioneers an innovative avenue in anti-counterfeiting methodologies by leveraging the intricate structures of hydrogel networks and the sensitivity of FRET lasers to molecular distances. We demonstrate the immense potential of hydrogels as a flexible and capable platform for optical encoding, primarily due to their vast structural complexity and high tunability. The critical aspect of our study lies in the successful utilization of hydrogel's structural randomness, a product of free radical polymerization, to generate intricate and secure anti-counterfeiting codes. In essence, the hydrogel's structural complexity and the FRET laser's capacity for sensing subtle changes in molecular distances, when combined, can yield an encoding method with increased data capacity, thereby providing enhanced protection against counterfeiting attempts. Nevertheless, the efficacy of this process is contingent upon careful consideration of several variables, including the choice of the excited locations on the microdisks, and the balance between the size of the laser pump light and the microdisk area. The coding rule, incorporating an array of both longitudinal and transverse modes, represents a level of complexity that poses challenges but also provides security. Our proof-of-concept experiment exhibits promising results, suggesting that our strategy, though intricate, can be effectively implemented and optimized for wider applicability. As we move forward, we envisage further investigations into materials that exhibit similar structural complexities and light-responsive properties as hydrogels. Future studies also need to assess the stability and robustness of the generated codes under varying environmental conditions and over extended periods. In sum, our research represents a significant leap in the field of anti-counterfeiting, amalgamating the strengths of material science and information security, offering a robust and efficient method for data encoding and decoding.

Chapter 7: Conclusion and Future Work

In this dissertation, we have explored the extensive potential of hydrogel-based microlasers, presenting a novel perspective on their versatile applications in the realms of both chemical and physical analysis. From the chemical perspective, we have successfully induced lasing signals from a hydrogel structure predicated on a WGM cavity. We conducted a thorough analysis of the performance characteristics of this hydrogel biological microlaser, specifically evaluating the lasing threshold and lasing intensity. Furthermore, our research demonstrated that this hydrogel biological microlaser holds the capability to detect variations in molecular distances between FRET pairs and differentiate molecular sizes based on the lasing threshold. Advancing from chemical molecules to living organisms, we proved that our biological microlaser array, fabricated through innovative inkjet printing, could encapsulate living organisms and allow us to monitor and quantify dynamic changes within these biological entities with greater sensitivity than conventional fluorescence analysis. Turning our attention to the physical side, we capitalized on the intrinsic properties of hydrogels to create tunable microlaser for anti-counterfeiting. The enzyme-based reactions we employed led to the controllable manipulation of the hydrogel's internal structure, and consequently, its lasing emission. This intricate control paved the way for information encoding and encryption, revealing the potential of hydrogel lasers in anti-counterfeiting applications. Lastly, to further explore the potential of hydrogel microlaser, we investigated the use of FRET lasers to detect subtle changes in molecular distances, exploiting the inherent structural randomness of hydrogel. The fusion of these elements resulted in a method of optical encoding with heightened data capacity, thus providing an additional layer of security against counterfeiting. In essence, this thesis underscores the versatility and vast potential of hydrogel microlasers, exploring their applications from biological and chemical analysis to physical encoding and anti-counterfeiting. Our research serves as a significant step forward in the intersection of biophotonics, and information security, opening avenues for further investigations and applications in these fields.

As a final outlook, we proposed some potential research directions that can be done in the future:

(1) In Chapter 3, we demonstrated the capability of a hydrogel microlaser to detect molecular distances and differentiate molecular sizes. However, the current design of the WGM hydrogel laser necessitates the inclusion of a DBR mirror to provide a sufficiently high cavity Q-factor for laser generation. While the printed laser array has great potential for high throughput biosensing, it's in vivo applications may be limited due to this requirement. Recent developments have seen hydrogel microdroplets being functionalized and injected into various in vivo environments such as vascular systems and tissues for chemical detection or drug delivery. If the hydrogel microlaser could be modified to function without the need for a bottom DBR, and if it could generate a WGM laser signal as a three-dimensional hydrogel microsphere, its applicability could be significantly broadened. One possible solution is to utilize monomer and crosslinker materials with a higher refractive index to create a hydrogel structure that retains its hydration while having a high refractive index. Our calculations suggest that for a microsphere in an aqueous environment to support lasing, the minimum required refractive index is 1.47.

(2) In Chapters 3 and 6, we demonstrated the ability of Fluorescence Resonance Energy Transfer (FRET) to reflect the interchain distances within hydrogel and the distances between molecules based on laser signals. As discussed in Chapter 2, hydrogels are considered ideal candidates for analyzing cellular mechanics, such as cell force mapping. We envisage that the integration of hydrogel microarray and FRET could provide a new-generation tool for quantifying cell force. A potential setup could be as follows:

Initially, a hydrogel embedded with FRET pairs would be fabricated. It's essential for the fluorophores to chemically bind with the hydrogel chain (as shown in Fig.7.1b) so that the distance between the FRET pairs changes when the hydrogel deforms. Subsequently, the hydrogel will be incubated with cells. Given the hydrogel's elasticity, we expect that cellular contraction would deform the hydrogel

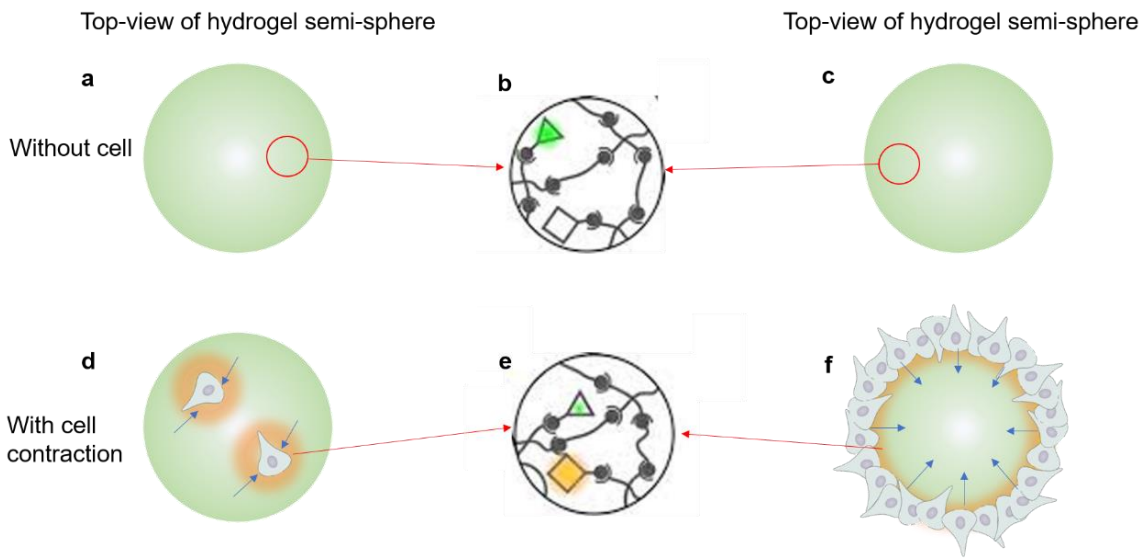

Figure 7.1 (a, c) Blank hydrogel semi-sphere. **(b)** Fluorophores endowed on the chain of hydrogel (large FRET distance). **(d)** Schematic diagram of cell contraction reflected by FRET fluorescence. **(e)** Fluorophores endowed on the chain of hydrogel (small FRET distance). **(e)** Large cell ring applies contraction force on hydrogel semi-sphere.

surface following successful attachment.

As depicted in Fig.7.1d, the fluorescence emitted from areas surrounding the cells changes from green to orange. Fig.7.1e illustrates the internal structural changes in the hydrogel near the cell. As the cell contracts, the hydrogel surface is squeezed, bringing the hydrogel chains closer together. As a result, the increased proximity of the FRET pairs boosts the FRET efficiency, leading to a shift in fluorescence.

Another setup is demonstrated in Fig.7.1f. Here, the cells form a ring that encircles the hydrogel sphere. In this configuration, the hydrogel is squeezed by a cell cluster instead of a single cell. With a larger number of cells, the exerted force is greater. By observing the periphery of the hydrogel sphere, we can minimize the influence of the green fluorescence background.

Author's Publications

Journal Papers

1. **Gong, X.,** Qiao, Z., Liao, Y., Zhu, S., Shi, L., Kim, M., & Chen, Y. C. (2022). Enzyme Programmable Microgel Lasers for Information Encoding and Anti‐Counterfeiting. ***Advanced Materials*****,** *34*(10), 2107809.
2. **Gong, X.,** Feng, S., Qiao, Z., & Chen, Y. C. (2021). Imaging-based optofluidic biological microlaser array encapsulated with dynamic living organisms. ***Analytical Chemistry*****,** *93*(14), 5823-5830.
3. **Gong, X.**, Qiao, Z., Guan, P., Feng, S., Yuan, Z., Huang, C., ... & Chen, Y. C. (2020). Hydrogel Microlasers for Versatile Biomolecular Analysis Based on a Lasing Microarray. ***Advanced Photonics Research*****,** *1*(1), 2000041
4. **Gong, X.,** Qiao, Z., Liao, Y., Chen, Y. C. (2023). Hydrogel Microlaser Anti-counterfeiting Labels Utilizing 3D Network Randomness. **Under review**
5. Zhang, Y.**, Gong, X.**, Yuan, Z., Wang, W., & Chen, Y. C. (2020). DNA self-switchable microlaser. ***ACS nano*****,** *14*(11), 16122-16130
6. Qiao, Z., **Gong, X.**, Guan, P., Yuan, Z., Feng, S., Zhang, Y., ... & Chen, Y. C. (2021). Lasing action in microdroplets modulated by interfacial molecular forces. ***Advanced Photonics*****,** *3*(1), 016003.
7. Jie, R. A., **Gong, X.**, Qiao, Z., & Chen, Y. C. (2022). Monitoring osmotic pressure with a hydrogel integrated optofluidic microlaser. ***Journal of Materials Chemistry C*****,** *10*(21), 8400-8406.

Conference papers

1. **Gong, X**., Feng, S., Qiao, Z., Yuan, Z., & Chen, Y. C. (2021, May). Inkjet Printed Optofluidic Biological microlasers for Laser Imaging Analysis of Living Organism. In *CLEO: Applications and Technology* (pp. AM3C-2). Optica Publishing Group.
2. **Gong, X.**, Qiao, Z., & Chen, Y. C. (2022, May). Programmable Microlaser Array Enabled by Living Biomaterials. In *2022 Conference on Lasers and Electro-Optics (CLEO)* (pp. 1-2). IEEE.
3. **Gong, X**., & Chen, Y. C. (2021, March). Hydrogel microlasers for versatile biomolecular analysis based on lasing microarray. In *Frontiers in Biological Detection: From Nanosensors to Systems XIII* (Vol. 11662, pp. 14-21). SPIE.

Appendices

Chapter 3

Table 1

Parameters	Description	value
n_d	Spatially averaged density of donor molecules	
q_d	Photon densities of lasing mode at donor emission band	
n_a	Spatially averaged density of acceptor molecules	
q_a	Photon densities of lasing mode at acceptor emission band	
I_p	Pump intensity	
σ_{pd}	Absorption cross section of donor molecules at pump wavelength	1.25×10^{-16} cm^2
σ_{pa}	Absorption cross section of acceptor molecules at pump wavelength	0.05×10^{-16} cm^2
σ_{edd}	Emission cross section of donor molecules at λ_d	1.19×10^{-16} cm^2
σ_{add}	Absorption cross section of donor molecules at λ_d	0.5×10^{-19} cm^2
σ_{aad}	Absorption cross section of acceptor molecules at λ_a	2.5×10^{-16} cm^2
σ_{eaa}	Emission cross section of acceptor molecules at λ_a	1.1×10^{-16} cm^2
σ_{aaa}	Absorption cross section of acceptor molecules at λ_a	2.0×10^{-18} cm^2
τ_d	Fluorescent lifetime of donor molecules	4.1 ns

τ_a	Fluorescent lifetime of acceptor molecules	1.68 ns
Δt	Pump pulse width	5 ns
η_F	Energy transfer efficiency	0.949 or 0.919 or 0.898
k_F	Energy transfer rate	$1/(1/\eta_F-1)(1/\tau_d)$
c	Light velocity	3×10^8 m/s
h	Planck's constant	6.62606957×10^{-34} J • s
η	Refractive Index	1.42
N_a	Total concentration of acceptor molecules	$1.2044\times10^{18}/cm^3$
N_d	Total concentration of donor molecules	$1.2044\times10^{18}/cm^3$
F	Fraction of mode volume occupied by the dye molecules	1
V	Volume of the electromagnetic mode	1.64×10^{-9} cm^2
λ_d	Emission wavelength of donor molecules	530 nm
λ_a	Emission wavelength of acceptor molecules	600 nm
λ_p	Pump wavelength	475 nm
Q	Q-factor	8×10^4
τ_{cd}	Photon life time of cavity at λ_d	$Q\lambda_d/(2\pi c)$
τ_{ca}	Photon life time of cavity at λ_a	$Q\lambda_d/(2\pi c)$

Table 2

Varibles or Parameters	Description	value
n	Spatially averaged density of RhB molecules	
q	Photon densities of lasing mode	
I_p	Pump intensity	
N_0	Total concentration of dye molecules	

σ_{ap}	Absorption cross section at pump wavelength	2.5×10^{-16} cm^2
σ_{el}	Emission cross section at lasing wavelength	1.1×10^{-16} cm^2
τ_f	Fluorescent lifetime	1.68 ns
Δt	Pump pulse width	5ns
c	Light velocity	3×10^8 m/s
h	Planck's constant	6.62606×10^{-34} J • s
η	Refractive Index	1.42 or 1.421
F	Fraction of mode volume occupied by the dye molecules	1
V	Volume of the electromagnetic mode	1.64×10^{-9} cm^2
λ_p	Pump wavelength	530 nm
λ_l	Lasing wavelength	600 nm
Q	Q-factor	8×10^4 or 8.0126×10^4
τ_q	Photon life time of cavity	$Q\lambda_l/(2\pi c)$

Bibliography

[1] Y.-C. Chen, Q. Chen, and X. Fan, "Lasing in blood," *Optica,* vol. 3, no. 8, pp. 809-815, 2016/08/20 2016. [Online]. Available: http://www.osapublishing.org/optica/abstract.cfm?URI=optica-3-8-809.

[2] Z. Qiao, Z. Wan, G. Xie, J. Wang, L. Qian, and D. Fan, "Multi-vortex laser enabling spatial and temporal encoding," *PhotoniX,* vol. 1, pp. 1-14, 2020.

[3] Z. Qiao *et al.*, "Cellular Features Revealed by Transverse Laser Modes in Frequency Domain," *Advanced Science,* vol. 9, no. 1, p. 2103550, 2022.

[4] Y.-C. Chen, X. Tan, Q. Sun, Q. Chen, W. Wang, and X. Fan, "Laser-emission imaging of nuclear biomarkers for high-contrast cancer screening and immunodiagnosis," *Nat. Biomed. Eng.,* vol. 1, no. 9, pp. 724-735, 2017.

[5] M. Schubert *et al.*, "Monitoring contractility in cardiac tissue with cellular resolution using biointegrated microlasers," *Nat. Photon.,* pp. 1-7, 2020.

[6] H. Chang *et al.*, "Ultrastable low-cost colloidal quantum dot microlasers of operative temperature up to 450 K," *Light: Science & Applications,* vol. 10, no. 1, p. 60, 2021.

[7] K. Wang *et al.*, "Geometry-programmable perovskite microlaser patterns for two-dimensional optical encryption," *Nano Letters,* vol. 21, no. 16, pp. 6792-6799, 2021.

[8] C. Wei, S.-Y. Liu, C.-L. Zou, Y. Liu, J. Yao, and Y. S. Zhao, "Controlled self-assembly of organic composite microdisks for efficient output coupling of whispering-gallery-mode lasers," *Journal of the American Chemical Society,* vol. 137, no. 1, pp. 62-65, 2015.

[9] S. Zhao, G. Li, X. Peng, J. Ma, Z. Yin, and Q. Zhao, "Ultralow-threshold green fluorescent protein laser based on high Q microbubble resonators," *Optics Express,* vol. 30, no. 13, pp. 23439-23447, 2022.

[10] Y.-C. Chen, Q. Chen, X. Wu, X. Tan, J. Wang, and X. Fan, "A robust tissue laser platform for analysis of formalin-fixed paraffin-embedded biopsies," *Lab Chip,* vol. 18, no. 7, pp. 1057-1065, 2018.

[11] Y.-C. Chen, Q. Chen, and X. Fan, "Optofluidic chlorophyll lasers," *Lab Chip,* vol. 16, no. 12, pp. 2228-2235, 2016.

[12] Z. Yuan *et al.*, "Bioresponsive microlasers with tunable lasing wavelength," *Nanoscale,* vol. 13, no. 3, pp. 1608-1615, 2021.

[13] T. Baba, "Photonic and Iontronic Sensing in GaInAsP Semiconductor Photonic Crystal Nanolasers," in *Photonics*, 2019, vol. 6, no. 2: Multidisciplinary Digital Publishing Institute, p. 65.

[14] N. Pourdavoud *et al.*, "Distributed feedback lasers based on MAPbBr3," *Advanced Materials Technologies,* vol. 3, no. 4, p. 1700253, 2018.

[15] N. A. I. M. Kamil *et al.*, "Principles and characteristics of random lasers and their applications in medical, bioimaging and biosensing," in *AIP Conference Proceedings*, 2020, vol. 2203, no. 1: AIP Publishing LLC, p. 020017.

[16] X. Fan and S.-H. Yun, "The potential of optofluidic biolasers," *Nat. Methods,* vol. 11, pp. 141-147, 2014.

[17] M. C. Gather and S. H. Yun, "Single-cell biological lasers," *Nat. Photon.,* vol. 5, pp. 406-410, 2011.
[18] M. Humar and S. H. Yun, "Intracellular microlasers," *Nat. Photon.,* vol. 9, pp. 572-576, 2015.
[19] X. Wu *et al.*, "Nanowire lasers as intracellular probes," *Nanoscale,* vol. 10, no. 20, pp. 9729-9735, 2018.
[20] Q. Chen, X. Zhang, Y. Sun, M. Ritt, S. Sivaramakrishnan, and X. Fan, "Highly sensitive fluorescent protein FRET detection using optofluidic lasers," *Lab Chip,* vol. 13, pp. 2679-2681, 2013.
[21] X. Tan *et al.*, "Fast and reproducible ELISA laser platform for ultrasensitive protein quantification," *ACS sensors,* vol. 5, no. 1, pp. 110-117, 2019.
[22] X. Yang *et al.*, "Turbidimetric inhibition immunoassay revisited to enhance its sensitivity via an optofluidic laser," *Biosens. Bioelectron.,* vol. 131, pp. 60-66, 2019.
[23] Y. W. Huang, J. Tao, and X. G. Huang, "Research progress on FP interference—based fiber-optic sensors," *Sensors,* vol. 16, no. 9, p. 1424, 2016.
[24] M. H. Bitarafan and R. G. DeCorby, "On-chip high-finesse Fabry-Perot microcavities for optical sensing and quantum information," *Sensors,* vol. 17, no. 8, p. 1748, 2017.
[25] N. Toropov, G. Cabello, M. P. Serrano, R. R. Gutha, M. Rafti, and F. Vollmer, "Review of biosensing with whispering-gallery mode lasers," *Light: Science & Applications,* vol. 10, no. 1, p. 42, 2021.
[26] M. Humar, "Liquid-crystal microdroplets as optical microresonators and lasers," Citeseer, 2012.
[27] Y. Zheng *et al.*, "Sensing and lasing applications of whispering gallery mode microresonators," *Opto-Electronic Advances,* vol. 1, no. 9, p. 180015, 2018.
[28] N. Komatsu *et al.*, "Development of an optimized backbone of FRET biosensors for kinases and GTPases," *Molecular biology of the cell,* vol. 22, no. 23, pp. 4647-4656, 2011.
[29] W. B. Asher *et al.*, "Single-molecule FRET imaging of GPCR dimers in living cells," *Nature methods,* vol. 18, no. 4, pp. 397-405, 2021.
[30] J. C. Sanders and E. D. Holmstrom, "Integrating single-molecule FRET and biomolecular simulations to study diverse interactions between nucleic acids and proteins," *Essays in biochemistry,* vol. 65, no. 1, pp. 37-49, 2021.
[31] M. Morimatsu, A. H. Mekhdjian, A. C. Chang, S. J. Tan, and A. R. Dunn, "Visualizing the interior architecture of focal adhesions with high-resolution traction maps," *Biophysical Journal,* vol. 108, no. 2, pp. 305a-306a, 2015.
[32] !!! INVALID CITATION !!! 32-34.
[33] Q. Shi, H. Liu, D. Tang, Y. Li, X. Li, and F. Xu, "Bioactuators based on stimulus-responsive hydrogels and their emerging biomedical applications," *NPG Asia Materials,* vol. 11, no. 1, p. 64, 2019.
[34] H. Shibata, Y. J. Heo, T. Okitsu, Y. Matsunaga, T. Kawanishi, and S. Takeuchi, "Injectable hydrogel microbeads for fluorescence-based in vivo continuous glucose monitoring," *Proceedings of the National Academy of Sciences,* vol.

107, no. 42, pp. 17894-17898, 2010.
[35] H.-I. Park and S.-Y. Park, "Smart fluorescent hydrogel glucose biosensing microdroplets with dual-mode fluorescence quenching and size reduction," *ACS Appl. Mater. Interfaces,* vol. 10, no. 36, pp. 30172-30179, 2018.
[36] M. K. Jaiswal, J. R. Xavier, J. K. Carrow, P. Desai, D. Alge, and A. K. Gaharwar, "Mechanically stiff nanocomposite hydrogels at ultralow nanoparticle content," *ACS nano,* vol. 10, no. 1, pp. 246-256, 2016.
[37] W. Lee, R. K. Singh, A. J. Putnam, S. Takayama, R. L. Leask, and C. Moraes, "Distributed hydrogel mechanosensors to measure internal forces in engineered tissues."
[38] X. Duan, S. Kamin, and N. Liu, "Dynamic plasmonic colour display," *Nature communications,* vol. 8, no. 1, p. 14606, 2017.
[39] B. Yoon, J. Lee, I. S. Park, S. Jeon, J. Lee, and J.-M. Kim, "Recent functional material based approaches to prevent and detect counterfeiting," *Journal of Materials Chemistry C,* vol. 1, no. 13, pp. 2388-2403, 2013.
[40] P. Kumar, S. Singh, and B. K. Gupta, "Future prospects of luminescent nanomaterial based security inks: from synthesis to anti-counterfeiting applications," *Nanoscale,* vol. 8, no. 30, pp. 14297-14340, 2016.
[41] W. Ren, G. Lin, C. Clarke, J. Zhou, and D. Jin, "Optical nanomaterials and enabling technologies for high-security-level anticounterfeiting," *Advanced Materials,* vol. 32, no. 18, p. 1901430, 2020.
[42] W. Diffie and M. E. Hellman, "New directions in cryptography," in *Democratizing Cryptography: The Work of Whitfield Diffie and Martin Hellman*, 2022, pp. 365-390.
[43] R. Pappu, B. Recht, J. Taylor, and N. Gershenfeld, "Physical one-way functions," *Science,* vol. 297, no. 5589, pp. 2026-2030, 2002.
[44] L. Jing *et al.*, "Multigenerational crumpling of 2D materials for anticounterfeiting patterns with deep learning authentication," *Matter,* vol. 3, no. 6, pp. 2160-2180, 2020.
[45] Y. W. Hu *et al.*, "Flexible and biocompatible physical unclonable function anti-counterfeiting label," *Advanced Functional Materials,* vol. 31, no. 34, p. 2102108, 2021.
[46] H. Im *et al.*, "Chaotic organic crystal phosphorescent patterns for physical unclonable functions," *Advanced Materials,* vol. 33, no. 44, p. 2102542, 2021.
[47] J. W. Leem *et al.*, "Edible unclonable functions," *Nature Communications,* vol. 11, no. 1, p. 328, 2020.
[48] Y. Fan *et al.*, "Randomly Induced Phase Transformation in Silk Protein-Based Microlaser Arrays for Anticounterfeiting," *Advanced Materials,* vol. 33, no. 42, p. 2102586, 2021.
[49] Y. Yao *et al.*, "Heteroepitaxial Growth of Multiblock Ln-MOF Microrods for Photonic Barcodes," *Angewandte Chemie,* vol. 131, no. 39, pp. 13941-13945, 2019.
[50] Y. C. Chen and X. Fan, "Biological Lasers for Biomedical Applications," *Adv. Opt. Mater.,* vol. 7, no. 11, p. 1900377, 2019.

[51] J. E. Hales;, G. Matmon;, P. A. Dalby;, J. M. Ward;, and G. Aeppli, "Virus lasers for biological detection," *Nat. Commun.,* vol. 10, no. 3594, pp. s41467-019-11604-z, 2019.
[52] S. Caixeiro, M. Gaio, B. Marelli, F. G. Omenetto, and R. Sapienza, "Silk-Based Biocompatible Random Lasing," *Adv. Opt. Mater.,* vol. 4, no. 7, pp. 998-1003, 2016.
[53] W. Lee, Q. Chen, X. Fan, and D. K. Yoon, "Digital DNA detection based on a compact optofluidic laser with ultra-low sample consumption," *Lab Chip,* vol. 16, no. 24, pp. 4770-4776, 2016.
[54] V. D. Ta, S. Caixeiro, F. M. Fernandes, and R. Sapienza, "Microsphere Solid-State Biolasers," *Adv. Opt. Mater.,* vol. 5, no. 8, 2017.
[55] T. Van Nguyen *et al.*, "Protein-based microsphere biolasers fabricated by dehydration," *Soft Matter,* vol. 15, no. 47, pp. 9721-9726, 2019.
[56] V. D. Ta, Y. Wang, and H. Sun, "Microlasers Enabled by Soft-Matter Technology," *Adv. Opt. Mater.,* vol. 7, no. 17, p. 1900057, 2019.
[57] Y. Wei, X. Lin, C. Wei, W. Zhang, Y. Yan, and Y. S. Zhao, "Starch-Based Biological Microlasers," *ACS Nano,* vol. 11, pp. 597–602, 2017.
[58] M. Humar, A. Dobravec, X. Zhao, and S. H. Yun, "Biomaterial microlasers implantable in the cornea, skin, and blood," *Optica,* vol. 4, no. 9, pp. 1080-1085, 2017.
[59] L. Zhao *et al.*, "Whispering gallery mode laser based on cholesteric liquid crystal microdroplets as temperature sensor," *Opt. Commun.,* vol. 402, pp. 181-185, 2017.
[60] A. Jonáš *et al.*, "In vitro and in vivo biolasing of fluorescent proteins suspended in liquid microdroplet cavities," *Lab on a Chip,* vol. 14, no. 16, pp. 3093-3100, 2014.
[61] X. Li *et al.*, "Ultrasound Modulated Droplet Lasers," *ACS Photon.,* vol. 6 no. 2, pp. 531-537, 2019.
[62] Z. Lv *et al.*, "Intracellular near-Infrared Microlaser Probes Based on Organic Microsphere–SiO2 Core–Shell Structures for Cell Tagging and Tracking," *ACS Appl. Mater. Interfaces,* vol. 10, no. 39, pp. 32981-32987, 2018.
[63] G. Pirnat, M. Humar, and I. Muševič, "Remote and autonomous temperature measurement based on 3D liquid crystal microlasers," *Optics Exp.,* vol. 26, no. 18, pp. 22615-22625, 2018.
[64] A. Matsumoto *et al.*, "Synthetic “smart gel” provides glucose-responsive insulin delivery in diabetic mice," *Sci. Adv,* vol. 3, no. 11, p. eaaq0723, 2017.
[65] K. Y. Lee and D. J. Mooney, "Hydrogels for tissue engineering," *Chem. Rev,* vol. 101, no. 7, pp. 1869-1880, 2001.
[66] J. Li and D. J. Mooney, "Designing hydrogels for controlled drug delivery," *Nat. Rev. Mater,* vol. 1, no. 12, pp. 1-17, 2016.
[67] L. Li *et al.*, "A nanostructured conductive hydrogels-based biosensor platform for human metabolite detection," *Nano Lett.,* vol. 15, no. 2, pp. 1146-1151, 2015.
[68] W. Lee *et al.*, "Dispersible hydrogel force sensors reveal patterns of solid mechanical stress in multicellular spheroid cultures," *Nat. Commun,* vol. 10, no.

1, pp. 1-14, 2019.
[69] M. Dolega, M. Delarue, F. Ingremeau, J. Prost, A. Delon, and G. Cappello, "Cell-like pressure sensors reveal increase of mechanical stress towards the core of multicellular spheroids under compression," *Nat. Commun,* vol. 8, no. 1, pp. 1-9, 2017.
[70] L. Jongpaiboonkit *et al.*, "An adaptable hydrogel array format for 3-dimensional cell culture and analysis," *Biomaterials,* vol. 29, no. 23, pp. 3346-3356, 2008.
[71] P. Gagni *et al.*, "A self-assembling peptide hydrogel for ultrarapid 3D bioassays," *Nanoscale Adv.,* vol. 1, no. 2, pp. 490-497, 2019.
[72] J. Zhao *et al.*, "Full-color laser displays based on organic printed microlaser arrays," *Nat. Commun.,* vol. 10, no. 1, pp. 1-7, 2019.
[73] V. D. Ta *et al.*, "Multicolor lasing prints," *Appl. Phys. Lett.,* vol. 107, no. 22, p. 221103, 2015.
[74] M. Choi, M. Humar, S. Kim, and S. H. Yun, "Step-index optical fiber made of biocompatible hydrogels," *Adv. Mater,* vol. 27, no. 27, pp. 4081-4086, 2015.
[75] S. Tanosaki, H. Taniguchi, K. Tsujita, and H. Inaba, "Microdroplet dye laser enhancing effects in dye-highly scattering intralipid mixture," *Applied physics letters,* vol. 69, no. 6, pp. 719-721, 1996.
[76] D. Gao, S. Wilken, A. B. Nguyen, G. R. Abraham, T. Liedl, and O. A. Saleh, "Controlling the size and adhesion of DNA droplets using surface-enriched DNA molecules," *Soft Matter,* vol. 20, no. 6, pp. 1275-1281, 2024.
[77] D. Erickson *et al.*, "Optofluidics," in *SPIE*, B. Javidi and D. Psaltis, Eds., 2005, vol. 5908. [Online]. Available: file:///Z:/Labs/Fan%20Lab/Fan/Paper%20Collection/Optofluidics.pdf. [Online]. Available: file:///Z:/Labs/Fan%20Lab/Fan/Paper%20Collection/Optofluidics.pdf
[78] X. Fan and I. M. White, "Optofluidic Microsystems for Chemical and Biological Analysis," *Nature Photon.,* vol. 5, pp. 591-597, 2011.
[79] P. Measor *et al.*, "On-chip surface-enhanced Raman scattering detection using integrated liquid-core waveguides," *Appl. Phys. Lett.,* vol. 90, p. 211107, 2007. [Online]. Available: file:///Z:/Labs/Fan%20Lab/Fan/Paper%20Collection/On-chip%20surface-enhanced%20Raman%20scattering%20detection%20using%20integrated%20liquid-core%20waveguides.pdf.
[80] C. Gong, Y. Gong, Q. Chen, Y.-J. Rao, G.-D. Peng, and X. Fan, "Reproducible fiber optofluidic laser for disposable and array applications," *Lab Chip,* vol. 17, no. 20, pp. 3431-3436, 2017.
[81] A. Chen *et al.*, "Dual-color fluorescence cross-correlation spectroscopy on a planar optofluidic chip," *Lab Chip,* vol. 11, 2011.
[82] Q. Chen, A. Kiraz, and X. Fan, "Optofluidic FRET lasers using aqueous quantum dots as donors," *Lab Chip,* vol. 16, pp. 353-359, 2016.
[83] Q. Chen, M. Ritt, S. Sivaramakrishnan, Y. Sun, and X. Fan, "Optofluidic lasers with a single molecular layer of gain," *Lab Chip,* vol. 14, pp. 4590-4595, 2014.
[84] H. Zhu, I. M. White, J. D. Suter, M. Zourob, and X. Fan, "Sensitive optofluidic micro-resonator for label-fee viral detection," *Analyst,* vol. 132, pp. 356-360,

2008.
[85] D. Erickson, D. Sinton, and D. Psaltis, "Optofluidics for energy applications," *Nature Photon.,* vol. 5, pp. 583-590, 2011.
[86] C. Lei *et al.*, "High-throughput imaging flow cytometry by optofluidic time-stretch microscopy," *Nature protocols,* vol. 13, no. 7, pp. 1603-1631, 2018.
[87] L.-P. Sun *et al.*, "Ultrasensitive optofluidic interferometer for online monitoring of photocatalytic reactions," *Journal of Lightwave Technology,* vol. 37, no. 21, pp. 5435-5441, 2019.
[88] X. Zhao, J. Xue, Z. Mu, Y. Huang, M. Lu, and Z. Gu, "Gold nanoparticle incorporated inverse opal photonic crystal capillaries for optofluidic surface enhanced Raman spectroscopy," *Biosensors and Bioelectronics,* vol. 72, pp. 268-274, 2015.
[89] J. Zhu *et al.*, "Optofluidics: the interaction between light and flowing liquids in integrated devices," *Opto-Electronic Advances,* vol. 2, no. 11, p. 190007, 2019.
[90] C. Monat, P. Domachuk, and B. J. Eggleton, "Integrated optofluidics: A new river of light," *Nature Photon.,* vol. 1, pp. 106-114, 2007. [Online]. Available: file:///Z:/Labs/Fan%20Lab/Fan/Paper%20Collection/Integrated%20optofluidics%20A%20new%20river%20of%20light.pdf.
[91] D. Erickson, D. Sinton, and D. Psaltis, "Optofluidics for energy applications," *Nature Photonics,* vol. 5, no. 10, p. 583, 2011.
[92] K. N. Chopra, "An overview of Optofluidics Technology as Novel approach for Renewable Energy," *Invertis Journal of Renewable Energy,* vol. 4, no. 3, pp. 140-148, 2014.
[93] Y.-F. Chen, L. Jiang, M. Mancuso, A. Jain, V. Oncescu, and D. Erickson, "Optofluidic opportunities in global health, food, water and energy," *Nanoscale,* vol. 4, no. 16, pp. 4839-4857, 2012.
[94] Y. C. Chen and X. Fan, "Biological lasers for biomedical applications," *Adv. Opt. Mater.,* vol. 7, no. 17, p. 1900377, 2019.
[95] Y.-C. Chen, Q. Chen, X. Wu, X. Tan, J. Wang, and X. Fan, "A robust tissue laser platform for analysis of formalin-fixed paraffin-embedded biopsies," *Lab on a Chip,* vol. 18, no. 7, pp. 1057-1065, 2018.
[96] X. Wu, M. K. Khaing Oo, K. Reddy, Q. Chen, Y. Sun, and X. Fan, "Optofluidic laser for dual-mode sensitive biomolecular detection with a large dynamic range," *Nature Commun.,* vol. 5, p. 3779, 2014.
[97] Y. Zhang, X. Gong, Z. Yuan, W. Wang, and Y.-C. Chen, "DNA Self-Switchable Microlaser," *ACS nano,* 2020.
[98] Y. Sun and X. Fan, "Distinguishing DNA by Analog-to-Digital-like Conversion by Using Optofluidic Lasers," *Angew. Chem. Int. Ed.,* vol. 51, pp. 1236-1239, 2012.
[99] Y. Sun, S. I. Shopova, C.-S. Wu, S. Arnold, and X. Fan, "Bioinspired optofluidic FRET lasers via DNA scaffolds," *Proc. Natl. Acad. Sci. USA,* vol. 107, pp. 16039-16042, 2010.
[100] H. Zhang, P. Palit, Y. Liu, S. Vaziri, and Y. Sun, "Reconfigurable Integrated Optofluidic Droplet Laser Arrays," *ACS Appl. Mater. Interfaces,* vol. 12, no. 24, pp. 26936-26942, 2020/06/17 2020, doi: 10.1021/acsami.0c05967.

[101] C. Gong *et al.*, "Distributed fibre optofluidic laser for chip-scale arrayed biochemical sensing," *Lab on a Chip,* vol. 18, no. 18, pp. 2741-2748, 2018.
[102] N. Zhang *et al.*, "High-Q and highly reproducible microdisks and microlasers," *Nanoscale,* vol. 10, no. 4, pp. 2045-2051, 2018.
[103] X. Yang *et al.*, "Mass production of thin-walled hollow optical fibers enables disposable optofluidic laser immunosensors," *Lab on a Chip,* vol. 20, no. 5, pp. 923-930, 2020.
[104] Z. Gu *et al.*, "Direct-Writing Multifunctional Perovskite Single Crystal Arrays by Inkjet Printing," *Small,* vol. 13, no. 8, p. 1603217, 2017.
[105] H. Zhang *et al.*, "2D Ruddlesden–Popper perovskites microring laser array," *Advanced Materials,* vol. 30, no. 15, p. 1706186, 2018.
[106] Z. Wang, Y. Ren, Y. Wang, Z. Gu, X. Li, and H. Sun, "Lateral cavity enabled Fabry-Perot microlasers from all-inorganic perovskites," *Applied Physics Letters,* vol. 115, no. 11, p. 111103, 2019.
[107] Y. Wang, X. Li, V. Nalla, H. Zeng, and H. Sun, "Solution-processed low threshold vertical cavity surface emitting lasers from all-inorganic perovskite nanocrystals," *Advanced Functional Materials,* vol. 27, no. 13, p. 1605088, 2017.
[108] P. Venugopalan, N. S. Mousavi, A. Dabirian, and S. Kumar, "Ultrasensitive biosensing based on plasmonic nanostructures," in *SPIE Micro+ Nano Materials, Devices, and Applications 2019*, 2019, vol. 11201: International Society for Optics and Photonics, p. 112011A.
[109] N. S. Mousavi and S. Kumar, "Effective in-field thermal conductivity of ferrofluids," *Journal of applied physics,* vol. 123, no. 4, p. 043902, 2018.
[110] P. Panindre, N. S. Mousavi, and S. Kumar, "Positive pressure ventilation for fighting wind-driven high-rise fires: simulation-based analysis and optimization," *Fire Safety Journal,* vol. 87, pp. 57-64, 2017.
[111] N. S. Mousavi and S. Kumar, "Effective heat capacity of ferrofluids–analytical approach," *International journal of thermal sciences,* vol. 84, pp. 267-274, 2014.
[112] N. S. Mousavi, S. D. Khapli, and S. Kumar, "Direct observations of field-induced assemblies in magnetite ferrofluids," *Journal of applied physics,* vol. 117, no. 10, p. 103907, 2015.
[113] X. Gong *et al.*, "Hydrogel Microlasers for Versatile Biomolecular Analysis Based on a Lasing Microarray," *Advanced Photonics Research,* vol. 1, no. 1, p. 2000041, 2020.
[114] J. G. Sutcliffe, "Nucleotide sequence of the ampicillin resistance gene of Escherichia coli plasmid pBR322," *Proceedings of the National Academy of Sciences,* vol. 75, no. 8, pp. 3737-3741, 1978.
[115] Y. Sun *et al.*, "Tetrahedral Framework Nucleic Acids Loading Ampicillin Improve the Drug Susceptibility against Methicillin-Resistant Staphylococcus aureus," *ACS Applied Materials & Interfaces,* vol. 12, no. 33, pp. 36957-36966, 2020.
[116] Z.-g. Yu, A. L. Sutlief, and R. Y. Lai, "Towards the development of a sensitive and selective electrochemical aptamer-based ampicillin sensor," *Sensors and Actuators B: Chemical,* vol. 258, pp. 722-729, 2018.

[117] Q. Ji *et al.*, "Layer-by-layer films of graphene and ionic liquids for highly selective gas sensing," *Angewandte Chemie International Edition,* vol. 49, no. 50, pp. 9737-9739, 2010.
[118] L. Jia *et al.*, "A facile photo-induced synthesis of COOH functionalized meso-macroporous carbon films and their excellent sensing capability for aromatic amines," *Chemical Communications,* vol. 48, no. 72, pp. 9029-9031, 2012.
[119] L. Jia *et al.*, "Highly ordered nanoporous carbon films with tunable pore diameters and their excellent sensing properties," *Chemistry–A European Journal,* vol. 21, no. 2, pp. 697-703, 2015.
[120] P. Srinivasu *et al.*, "Novel three dimensional cubic Fm3m mesoporous aluminosilicates with tailored cage type pore structure and high aluminum content," *Advanced Functional Materials,* vol. 18, no. 4, pp. 640-651, 2008.
[121] G. P. Mane *et al.*, "Preparation of highly ordered nitrogen-containing mesoporous carbon from a gelatin biomolecule and its excellent sensing of acetic acid," *Advanced Functional Materials,* vol. 22, no. 17, pp. 3596-3604, 2012.
[122] R. M. Jarvis and R. Goodacre, "Discrimination of bacteria using surface-enhanced Raman spectroscopy," *Analytical Chemistry,* vol. 76, no. 1, pp. 40-47, 2004.
[123] S. Pahlow, S. Meisel, D. Cialla-May, K. Weber, P. Rösch, and J. Popp, "Isolation and identification of bacteria by means of Raman spectroscopy," *Advanced drug delivery reviews,* vol. 89, pp. 105-120, 2015.
[124] M. Kaur and V. Kumar, "A comprehensive review on image encryption techniques," *Archives of Computational Methods in Engineering,* vol. 27, no. 1, pp. 15-43, 2020.
[125] M. Khan and T. Shah, "A literature review on image encryption techniques," *3D Research,* vol. 5, no. 4, pp. 1-25, 2014.
[126] Z. Gao *et al.*, "Laterally Engineering Ln-MOFs Epitaxial Heterostructures for Spatially Resolved Planar 2D Photonic Barcoding," *Angewandte Chemie,* 2021.
[127] H. Al Sabea *et al.*, "Efficient photomodulation of visible Eu (III) and invisible Yb (III) luminescences using DTE photochromic ligands for optical encryption," *Advanced Functional Materials,* vol. 30, no. 30, p. 2002943, 2020.
[128] Y. Chen, J. Gao, and X. Yang, "Chiral grayscale imaging with plasmonic metasurfaces of stepped nanoapertures," *Advanced Optical Materials,* vol. 7, no. 6, p. 1801467, 2019.
[129] T. Nomura and B. Javidi, "Optical encryption using a joint transform correlator architecture," *Optical Engineering,* vol. 39, no. 8, pp. 2031-2035, 2000.
[130] G. Qu *et al.*, "Reprogrammable meta-hologram for optical encryption," *Nature communications,* vol. 11, no. 1, pp. 1-5, 2020.
[131] G. Unnikrishnan, M. Pohit, and K. Singh, "A polarization encoded optical encryption system using ferroelectric spatial light modulator," *Optics communications,* vol. 185, no. 1-3, pp. 25-31, 2000.
[132] G. Unnikrishnan, J. Joseph, and K. Singh, "Optical encryption by double-random phase encoding in the fractional Fourier domain," *Optics letters,* vol. 25,

no. 12, pp. 887-889, 2000.
[133] Z. Gao, K. Wang, Y. Yan, J. Yao, and Y. S. Zhao, "Smart responsive organic microlasers with multiple emission states for high-security optical encryption," *National Science Review,* vol. 8, no. 2, p. nwaa162, 2021.
[134] X. Guo *et al.*, "Full-Color Holographic Display and Encryption with Full-Polarization Degree of Freedom," *Adv. Mater.,* p. 2103192, 2021.
[135] K. T. Lim, H. Liu, Y. Liu, and J. K. Yang, "Holographic colour prints for enhanced optical security by combined phase and amplitude control," *Nat. Commun.,* vol. 10, no. 1, pp. 1-8, 2019.
[136] K. Wang *et al.*, "Geometry-Programmable Perovskite Microlaser Patterns for Two-Dimensional Optical Encryption," *Nano Letters,* 2021.
[137] Y. Wu, Y. Ren, J. Guo, Z. Liu, L. Liu, and F. Yan, "Imidazolium-type ionic liquid-based carbon quantum dot doped gels for information encryption," *Nanoscale,* vol. 12, no. 40, pp. 20965-20972, 2020.
[138] Y. Liu *et al.*, "Inkjet-printed unclonable quantum dot fluorescent anti-counterfeiting labels with artificial intelligence authentication," *Nature communications,* vol. 10, no. 1, pp. 1-9, 2019.
[139] Z. Gao *et al.*, "Spatially Responsive Multicolor Lanthanide-MOF Heterostructures for Covert Photonic Barcodes," *Angewandte Chemie International Edition,* vol. 59, no. 43, pp. 19060-19064, 2020.
[140] Y. Yang *et al.*, "Modular nanocomposite films with tunable physical organization of cellulose nanocrystals for photonic encryption," *Advanced Optical Materials,* vol. 8, no. 12, p. 2000547, 2020.
[141] Y. Zhao, H. C. Shum, H. Chen, L. L. Adams, Z. Gu, and D. A. Weitz, "Microfluidic generation of multifunctional quantum dot barcode particles," *Journal of the American Chemical Society,* vol. 133, no. 23, pp. 8790-8793, 2011.
[142] L. Bai *et al.*, "Bio-inspired vapor-responsive colloidal photonic crystal patterns by inkjet printing," *ACS nano,* vol. 8, no. 11, pp. 11094-11100, 2014.
[143] J. Feng *et al.*, "Random organic nanolaser arrays for cryptographic primitives," *Advanced Materials,* vol. 31, no. 36, p. 1807880, 2019.
[144] Y. Bian, H. Xue, and Z. Wang, "Programmable Random Lasing Pluses Based on Waveguide-Assisted Random Scattering Feedback," *Laser & Photonics Reviews,* vol. 15, no. 4, p. 2000506, 2021.
[145] X. Shi, W. Song, D. Guo, J. Tong, and T. Zhai, "Selectively Visualizing the Hidden Modes in Random Lasers for Secure Communication," *Laser & Photonics Reviews,* p. 2100295, 2021.
[146] Y. Fan *et al.*, "Randomly Induced Phase Transformation in Silk Protein-Based Microlaser Arrays for Anticounterfeiting," *Advanced Materials,* p. 2102586, 2021.
[147] K. Kim *et al.*, "Massively parallel ultrafast random bit generation with a chip-scale laser," *Science,* vol. 371, no. 6532, pp. 948-952, 2021.
[148] Z. Gao *et al.*, "Covert Photonic Barcodes Based on Light Controlled Acidichromism in Organic Dye Doped Whispering-Gallery-Mode Microdisks," *Advanced Materials,* vol. 29, no. 30, p. 1701558, 2017.

[149] Y. Hou, Z. Gao, Y. S. Zhao, and Y. Yan, "Organic micro/nanoscale materials for photonic barcodes," *Organic Chemistry Frontiers,* vol. 7, no. 18, pp. 2776-2788, 2020.
[150] F.-F. Xu, Z.-L. Gong, Y.-W. Zhong, J. Yao, and Y. S. Zhao, "Wavelength-tunable single-mode microlasers based on photoresponsive pitch modulation of liquid crystals for information encryption," *Research,* vol. 2020, 2020.
[151] C. Gong *et al.*, "Topological Encoded Vector Beams for Monitoring Amyloid-Lipid Interactions in Microcavity," *Advanced Science,* p. 2100096, 2021.
[152] Y. Na and D.-K. Ko, "Deep-learning-based high-resolution recognition of fractional-spatial-mode-encoded data for free-space optical communications," *Scientific Reports,* vol. 11, no. 1, pp. 1-11, 2021.
[153] M. Szatkowski, J. Masajada, I. Augustyniak, and K. Nowacka, "Generation of composite vortex beams by independent Spatial Light Modulator pixel addressing," *Optics Communications,* vol. 463, p. 125341, 2020.
[154] S. N. Khonina, A. V. Ustinov, S. A. Fomchenkov, and A. P. Porfirev, "Formation of hybrid higher-order cylindrical vector beams using binary multi-sector phase plates," *Scientific Reports,* vol. 8, no. 1, pp. 1-11, 2018.
[155] F. Bian, L. Sun, L. Cai, Y. Wang, and Y. Zhao, "Bioinspired MXene-integrated colloidal crystal arrays for multichannel bioinformation coding," *Proceedings of the National Academy of Sciences,* vol. 117, no. 37, pp. 22736-22742, 2020.
[156] H. Wu, H. Wang, F. Cheng, F. Xu, and G. Cheng, "Synthesis and characterization of an enzyme-degradable zwitterionic dextran hydrogel," *RSC advances,* vol. 6, no. 37, pp. 30862-30866, 2016.
[157] Y. Zhao, Z. Xie, H. Gu, C. Zhu, and Z. Gu, "Bio-inspired variable structural color materials," *Chemical Society Reviews,* vol. 41, no. 8, pp. 3297-3317, 2012.
[158] J.-H. Kim and T. R. Lee, "Thermo-and pH-responsive hydrogel-coated gold nanoparticles," *Chemistry of materials,* vol. 16, no. 19, pp. 3647-3651, 2004.
[159] Q.-L. Huang *et al.*, "Stretchable PEG-DA hydrogel-based whispering-gallery-mode microlaser with humidity responsiveness," *Journal of Lightwave Technology,* vol. 36, no. 3, pp. 819-824, 2018.
[160] Y. B. Schuetz, R. Gurny, and O. Jordan, "A novel thermoresponsive hydrogel based on chitosan," *European Journal of Pharmaceutics and Biopharmaceutics,* vol. 68, no. 1, pp. 19-25, 2008.
[161] S. Jung, J. L. Kaar, and M. P. Stoykovich, "Design and functionalization of responsive hydrogels for photonic crystal biosensors," *Molecular Systems Design & Engineering,* vol. 1, no. 3, pp. 225-241, 2016.
[162] S. Li *et al.*, "Photo-responsive photonic hydrogel: in situ manipulation and monitoring of cell scaffold stiffness," *Materials Horizons,* vol. 7, no. 11, pp. 2944-2950, 2020.
[163] P. Shen *et al.*, "Three-dimensional/two-dimensional photonic crystal hydrogels for biosensing," *Journal of Materials Chemistry C,* vol. 9, no. 18, pp. 5840-5857, 2021.
[164] F. J. Fraile-Peláez and A. Macho, "Electromagnetic Formalism of the Propagation and Amplification of Light," *arXiv preprint arXiv:1907.06504,* 2019.

[165] P. Chýlek, D. Ngo, and R. Pinnick, "Resonance structure of composite and slightly absorbing spheres," *JOSA A,* vol. 9, no. 5, pp. 775-780, 1992.
[166] X. Gong *et al.*, "Enzyme-Programmable Microgel Lasers for Information Encoding and Anti-Counterfeiting," *Advanced Materials,* vol. 34, no. 10, p. 2107809, 2022.
[167] A. I. Chou, S. O. Akintoye, and S. B. Nicoll, "Photo-crosslinked alginate hydrogels support enhanced matrix accumulation by nucleus pulposus cells in vivo," *Osteoarthr.,* vol. 17, no. 10, pp. 1377-1384, 2009.
[168] M. Cheng *et al.*, "Writable and self-erasable hydrogel based on dissipative assembly process from multiple carboxyl tetraphenylethylene derivative," *ACS Mater. Lett.,* vol. 2, no. 4, pp. 425-429, 2020.
[169] C. H. Cheng, D. S. Yang, J. Kim, and P. B. Deotare, "Nanoscale Strain Engineering: Self-Erasable and Rewritable Optoexcitonic Platform for Antitamper Hardware (Advanced Optical Materials 21/2020)," *Adv. Opt. Mater.,* vol. 8, no. 21, p. 2070082, 2020.
[170] Z. Guo *et al.*, "Hyperboloid-Drum Microdisk Laser Biosensors for Ultrasensitive Detection of Human IgG," *Small,* vol. 16, no. 26, p. 2000239, 2020.
[171] Z. Wang *et al.*, "Bio-electrostatic sensitive droplet lasers for molecular detection," *Nanoscale Adv.,* vol. 2, no. 7, pp. 2713-2719, 2020.
[172] Y. Hu *et al.*, "3D-Integrated metasurfaces for full-colour holography," *Light: Science & Applications,* vol. 8, no. 1, p. 86, 2019.
[173] A. Abdollahi, H. Roghani-Mamaqani, B. Razavi, and M. Salami-Kalajahi, "Photoluminescent and chromic nanomaterials for anticounterfeiting technologies: recent advances and future challenges," *ACS nano,* vol. 14, no. 11, pp. 14417-14492, 2020.
[174] X. Yu, H. Zhang, and J. Yu, "Luminescence anti-counterfeiting: from elementary to advanced," *Aggregate,* vol. 2, no. 1, pp. 20-34, 2021.
[175] R. Arppe and T. J. Sørensen, "Physical unclonable functions generated through chemical methods for anti-counterfeiting," *Nature Reviews Chemistry,* vol. 1, no. 4, p. 0031, 2017.
[176] H. Suo, Q. Zhu, X. Zhang, B. Chen, J. Chen, and F. Wang, "High-security anti-counterfeiting through upconversion luminescence," *Materials Today Physics,* vol. 21, p. 100520, 2021.
[177] Y. Xie, Y. Song, G. Sun, P. Hu, A. Bednarkiewicz, and L. Sun, "Lanthanide-doped heterostructured nanocomposites toward advanced optical anti-counterfeiting and information storage," *Light: Science & Applications,* vol. 11, no. 1, p. 150, 2022.
[178] F. Zhang *et al.*, "Multimodal, convertible, and chiral optical films for anti-counterfeiting labels," *Advanced Functional Materials,* vol. 32, no. 33, p. 2204487, 2022.
[179] H. Song *et al.*, "RGB Tricolor and Multimodal Dynamic Optical Information Encryption and Decoding for Anti-Counterfeiting Applications," *ACS Applied Materials & Interfaces,* vol. 14, no. 40, pp. 45562-45572, 2022.
[180] L. Bai *et al.*, "Hierarchical disordered colloidal thin films with duplex optical

elements for advanced anti-counterfeiting coding," *Advanced Optical Materials,* vol. 8, no. 24, p. 2001378, 2020.
[181] K. Huang *et al.*, "Ultraviolet Metasurfaces of≈ 80% Efficiency with Antiferromagnetic Resonances for Optical Vectorial Anti-Counterfeiting," *Laser & Photonics Reviews,* vol. 13, no. 5, p. 1800289, 2019.
[182] G. Ruffato, R. Rossi, M. Massari, E. Mafakheri, P. Capaldo, and F. Romanato, "Design, fabrication and characterization of computer generated holograms for anti-counterfeiting applications using OAM beams as light decoders," *Scientific reports,* vol. 7, no. 1, p. 18011, 2017.
[183] R. Lee, "Micro-technology for anti-counterfeiting," *Microelectronic Engineering,* vol. 53, no. 1-4, pp. 513-516, 2000.
[184] K. Jiang, L. Zhang, J. Lu, C. Xu, C. Cai, and H. Lin, "Triple-mode emission of carbon dots: applications for advanced anti-counterfeiting," *Angewandte Chemie International Edition,* vol. 55, no. 25, pp. 7231-7235, 2016.
[185] H. Hu, Q.-W. Chen, J. Tang, X.-Y. Hu, and X.-H. Zhou, "Photonic anti-counterfeiting using structural colors derived from magnetic-responsive photonic crystals with double photonic bandgap heterostructures," *Journal of Materials Chemistry,* vol. 22, no. 22, pp. 11048-11053, 2012.
[186] J. C. Arango *et al.*, "Nanostructured Surface Functionalization of Polyacrylamide Hydrogels Below the Length Scale of Hydrogel Heterogeneity," *ACS Applied Materials & Interfaces,* vol. 14, no. 38, pp. 43937-43945, 2022.
[187] B. Xue *et al.*, "Engineering hydrogels with homogeneous mechanical properties for controlling stem cell lineage specification," *Proceedings of the National Academy of Sciences,* vol. 118, no. 37, p. e2110961118, 2021.
[188] M. W. Tibbitt, A. M. Kloxin, L. A. Sawicki, and K. S. Anseth, "Mechanical properties and degradation of chain and step-polymerized photodegradable hydrogels," *Macromolecules,* vol. 46, no. 7, pp. 2785-2792, 2013.
[189] Y. Sun, X. Le, S. Zhou, and T. Chen, "Recent progress in smart polymeric gel-based information storage for anti-counterfeiting," *Advanced Materials,* vol. 34, no. 41, p. 2201262, 2022.
[190] B. Prevo and E. J. Peterman, "Förster resonance energy transfer and kinesin motor proteins," *Chemical Society Reviews,* vol. 43, no. 4, pp. 1144-1155, 2014.